Evaluating the Impact Diminished *SKP1* and *CUL1* Expression Have on Chromosome Instability and High-Grade Serous Ovarian Cancer Pathogenesis

by

Chloe C. Lepage

A Thesis submitted to the Faculty of Graduate Studies of
The University of Manitoba
in partial fulfillment of the requirements of the degree of

MASTER OF SCIENCE

Department of Biochemistry and Medical Genetics
University of Manitoba
Winnipeg

TABLE OF CONTENTS

ABSTRACT

High-grade serous ovarian cancer (HGSOC) is the most common and lethal ovarian cancer subtype. Chromosome instability (CIN; an increased rate of chromosome gains and losses) is believed to play a fundamental role in the development and evolution of HGSOC. The current study aims to evaluate the underlying mechanisms responsible for inducing CIN in HGSOC. Importantly, overexpression of Cyclin E1 protein induces CIN and genomic amplification contributes to HGSOC pathogenesis in ~20% of patients. Misregulation of Cyclin E1 at the protein level (*i.e.* aberrant protein turnover) is also expected to be causally linked to CIN and HGSOC development, but has never been evaluated in this context. Cyclin E1 levels are normally regulated in a cell cycle-dependent manner by the SCF (SKP1-CUL1-FBOX) complex, an E3 ubiquitin ligase that includes the proteins SKP1 and CUL1. Conceptually, loss of SCF complex function stemming from diminished *SKP1* or *CUL1* expression is predicted to underlie increases in Cyclin E1 protein levels and induce CIN. This study evaluates the impact of diminished *SKP1* or *CUL1* expression in a fallopian tube secretory epithelial cell model (a cell of origin for HGSOC) using two complementary approaches (siRNA and CRISPR/Cas9). Single-cell quantitative imaging microscopy approaches were employed to evaluate changes in CIN-associated phenotypes in response to diminished *SKP1* or *CUL1* expression. Our data identify *SKP1* and *CUL1* as novel CIN genes in HGSOC precursor cells that may contribute to the early development and pathogenesis of HGSOC.

ACKNOWLEDGEMENTS

This thesis represents the culmination of more than two years' worth of research, which was supported by the diverse contributions of many individuals who must be recognized.

To Kirk and Mark, this is the part of my thesis where saying what I mean in "as few words as possible" is still going to require a large number of words, because there is a lot of meaning to convey. Kirk, throughout my time in your lab and encompassing each of my various roles from undergraduate trainee to MSc student, you have always been an outstanding mentor. Thank you for giving me the freedom to explore, with the right amount of guidance and support to keep me on track. Thank you for *noticing* and *appreciating* the details. Mark, you have been a wonderful co-advisor over these past two years. Discussions with you always feel empowering and inspiring, and have given me confidence and clarity with respect to my future beyond graduate school. Thank you both for your trust and patience. Most of all, thank you for helping me grow and learn.

Thank you to my advisory committee and members of the larger university community for sharing your time and expertise. Barb and Sabine, you have truly been the perfect complements to my advisory committee! Jeff, thank you for chairing all of my committee meetings and taking an interest in my research. You have each offered unique perspectives and insights that have helped shape my MSc program into a very positive and enriching experience.

Thank you to all individuals and organizations who provided funding that made this research possible. This research is a direct product of financial support from Canadian Institutes of Health Research, University of Manitoba, CancerCare Manitoba, and the Research Institute in Oncology and Hematology. I would also like to thank the donors who generously provided funding for the Emil and Lynette Hain Scholarship in Oncology Research, Phyllis J. McAlpine Graduate Fellowship, and the Manitoba Medical Services Foundation Major Student Research Award.

To all current and former lab members who have supported me along this journey, you are all wonderful and I feel the need to thank you each individually (in no particular order). Lucile, thank you for being a great friend. You're the person I go to when I'm feeling lost and I need a sense of reason, clarity, and purpose; after talking with you, everything makes sense again. Laura, thank you for your wisdom, advice, and insight. You have contributed so much to the lab and paved the way for many projects including my own. You are an inspiration and a role model. Manisha, I'm so fortunate to have had you by my side (literally) at every stage of this MSc journey – we've been through a lot together! Thank you for your warmth, care, and generosity. Claire (my

erstwhile writing partner), thank you for your energy, openness, and compassion. You're the person I go to for commiseration and also for celebration. Zelda, you make the lab such a welcoming place for all of us and you are so greatly appreciated. Nicole, thank you for helping me get on my feet as a new grad student; you helped me feel comfortable and supported. Michaela, thank you for your empathy and enthusiasm; Kailee, thank you for your thoughtfulness and positivity – the lab is more fun with both of you in it. Morgan and Ally, thank you for bringing fresh new energy into the lab! Thank you to all the former lab members whose paths crossed with mine and who helped establish and maintain the positive lab culture we have now. These past two years were so much better for having known each of you.

Finally, to Mom, Dad, Mahalia, Maceo, and all other family and friends outside of my graduate school bubble, I appreciate you beyond what I am able to express here. Thank you for your patience and understanding. I have been so fully immersed in this program and I feel as though these past two years I have demanded more support than I have been able to give back. Thank you all for continuing to reach out, for taking care of me or encouraging me to take care of myself. If you sent me music for my writing playlist, this whole thesis is infused with those feelings and ideas. If you cooked me meals, you fueled my ability to complete this program and write this document. If you spent time with me outside of the lab, you gave my mind the rest and peace I sometimes forgot it needed. I know none of you will read this document but thank you all for listening to me and sharing in my excitement!

LIST OF TABLES

LIST OF FIGURES

LIST OF ABBREVIATIONS

~	Approximately
µg	Microgram(s) (weight)
µL	Microliter(s) (volume)
µm	Micron(s) (size)
µM	Micromolar (concentration)
°C	Degrees Celsius
aa	Amino acid(s)
BCA	Bicinchoninic acid
BFP	Blue fluorescent protein
BSA	Bovine serum albumin
bp	Base pair(s)
CCD	Charge-coupled device
CIN	Chromosome instability
cm	Centimeter(s) (size)
CO_2	Carbon dioxide
CPTS	Copper phthalocyanine 3, 4', 4'', 4'''-tetrasulfonic acid tetrasodium salt
CRC	Colorectal cancer
CRISPR	Clustered regularly interspaced short palindromic repeats
CRL	Cullin-RING ubiquitin ligase
CUL1	Cullin 1
DAPI	4',6-Diamidino-2-Phenylindole
DMEM	Dulbecco's modified Eagle medium
DSB	Double-strand break
EDTA	Ethylenediaminetetraacetic acid
EOC	Epithelial ovarian cancer
FACS	Fluorescence-activated cell sorting
FBS	Fetal bovine serum
FT	Fallopian tube secretory epithelial
GFP	Green fluorescent protein
GOF	Gain-of-function
h	Hour(s)
HBSS	Hank's balanced salt solution
HGSOC	High-grade serous ovarian cancer
HRP	Horseradish peroxidase
HRR	Homologous recombination repair
Indels	Insertions or deletions
IHC	Immunohistochemistry
kb	Kilobase(s)
kDa	Kilodalton(s)
K-S	Kolmogorov-Smirnov
LB	Luria-Bertani
LOF	Loss-of-function
min	Minute(s)
mL	Milliliter(s) (volume)

MNF	Micronucleus formation
M-W	Mann-Whitney
n	Number of technical replicates
N	Number of experimental replicates
NA	Nuclear area
N-CIN	Numerical chromosome instability
NHEJ	Nonhomologous end joining
nm	Nanometer(s) (size)
nM	Nanomolar (concentration)
NMD	Nonsense-mediated mRNA decay
nt	Nucleotide(s)
PBS	Phosphate buffered saline
PCR	Polymerase chain reaction
PI	Propidium iodide
PTC	Premature termination codon
P-value	Probability value
PVDF	Polyvinylidene difluoride
RBX1	RING box protein 1
RIPA	Radioimmunoprecipitation assay
ROS	Reactive oxygen species
RT	Room temperature
RTCA	Real-time cell analysis
rpm	Revolutions per minute
SCF	SKP1-CUL1-FBOX protein
S-CIN	Structural chromosome instability
SFM	Serum-free medium
sgRNA	Synthetic guide RNA
SKP1	S-phase kinase-associated protein 1
SKY	Spectral karyotyping
sec	Second(s)
siRNA	Short interfering RNA
SOC	Super optimal broth with catabolite repression
STIC	Serous tubal intraepithelial carcinoma
TAE	Tris-acetate-EDTA
TBST	Tris-buffered saline + Tween 20
USG	Ultroser G
V	Volts
vs.	Versus
WGA	Wheat germ agglutinin
w/v	Weight by volume

USED WITH PERMISSION and CONTRIBUTION OF AUTHOR

PREFACE:

This thesis contains material, images, and/or ideas from one article published in the peer-reviewed journal *Cancers*, of which Chloe Lepage was co-first author. This journal applies the Creative Commons Attribution (CC BY) license to articles and other works, such that articles can be reused in whole or in part for any purpose.

CONTRIBUTION OF AUTHOR

CHAPTER 1:

Lepage, C.C., Morden, C.R., Palmer, M.C.L., Nachtigal, M.W., and McManus, K.J. Detecting Chromosome Instability in Cancer: Approaches to Resolve Cell-to-Cell Heterogeneity. *Cancers*. **11**, (2019).

Contribution: Chloe Lepage contributed to original draft preparation (50%), editing (50%), and figure preparation (100%).

CHAPTER 1. INTRODUCTION

1.1. OVARIAN CANCER OVERVIEW

In Canada, 220,400 new cancer diagnoses occur each year, and 1 in 2 Canadians are predicted to be diagnosed with cancer in their lifetime[1]. Approximately half of all cancer diagnoses lead to fatality, with 82,100 cancer-related deaths occurring each year in Canada[1]. Ovarian cancer specifically accounts for 2.8% of all cancer diagnoses in women (~3,000 Canadians annually) and the average lifetime risk of ovarian cancer is 1.3% (~1 in 75 women)[1]. Relative to overall cancer mortality, ovarian cancer has a disproportionately high mortality rate and accounts for 4.9% of all cancer deaths (~1,900 Canadians annually)[1]. Importantly, ovarian cancer encompasses a heterogeneous set of diseases and survival outcomes vary between different histological subtypes (*i.e.* histotypes)[2,3]. High-grade serous ovarian cancer (HGSOC) is the most common and aggressive ovarian cancer histotype[4], and is frequently diagnosed at advanced stages, when chemotherapy is typically required to treat residual disease following cytoreductive surgery[5]. Despite strong initial response rates, the majority of HGSOC patients ultimately develop drug resistance leading to disease recurrence[6]. Thus, improving early disease detection and developing more effective therapeutic strategies are two key research areas that are expected to improve outcomes for HGSOC patients. The current study explores the early etiology of HGSOC and the molecular events suspected to contribute to HGSOC pathogenesis.

1.1.1. Epithelial Ovarian Cancer (EOC) Histotypes

The majority of ovarian cancers are epithelial in origin, while sex cord-stromal and germ cell tumors represent a minor fraction (< 10%) of ovarian cancer cases[2,3]. Epithelial ovarian cancers (EOCs) are typically categorized as one of five major histotypes: high-grade serous, low-grade serous, endometrioid, clear cell, or mucinous[7]. HGSOC represents the most common

histotype, accounting for ~70% of all EOC diagnoses, while endometrioid, clear cell, low-grade serous, and mucinous tumors account for ~10%, 10%, 5%, and 3% of diagnoses, respectively[3,7]. Importantly, the major EOC histotypes have different etiological origins and are associated with distinct sets of risk factors and therapeutic outcomes[7]. While cells within the ovarian surface epithelium were previously believed to be the primary source of all EOCs (reviewed by Levanon *et al.*[8]), more recent studies have shown that each histotype most likely arises from a distinct non-ovarian tissue, and the ovarian surface epithelium actually represents a secondary site in the oncogenic pathway[7]. There is strong molecular, genetic, and clinical evidence demonstrating that serous ovarian cancers originate from secretory epithelial cells within the distal fallopian tube mucosa[9–14] (described further in Section 1.1.3.), while the endometrioid and clear cell histotypes likely arise from displaced endometrial tissue (*i.e.* endometriosis)[15–17]. Mucinous ovarian cancers may originate from cells within the tubal-peritoneal junction (*i.e.* the site on the fallopian tube fimbriae where the inner mucosal epithelium meets the outer peritoneal mesothelium)[18], or in some cases may represent a metastatic deposit from a gastrointestinal primary tumor[18].

EOCs are often classified as either "Type I" or "Type II" tumors to describe two different pathways of tumor development and progression[19]. Type I tumors are low grade, slow-growing, and typically present at early stages[19,20] (see Section 1.1.2.). These tumors are characterized by a small number of defined genetic alterations such as *BRAF*[21], *KRAS*[21], or *PTEN*[22] mutations, along with wild-type *TP53*[23]. Low-grade serous carcinoma, low-grade endometrioid carcinoma, clear-cell carcinoma, and mucinous carcinoma are all categorized as Type I tumors[20]. Type II tumors are high grade, and typically present at advanced stages suggesting rapid disease progression[19,20]. Type II tumors are further defined by a high degree of genomic complexity relative to Type I tumors, including a large number of low frequency gene mutations, copy number alterations and

structural changes[24–26] as well as ubiquitous mutation of *TP53*[23,24]. Type II tumors include HGSOCs and additional rare EOC subtypes (*e.g.* high-grade endometrioid carcinomas and undifferentiated carcinomas)[20], and are associated with poor prognoses[20].

1.1.2. EOC Staging, Treatment and Prognosis

EOC staging is typically assessed as per the American Joint Committee on Cancer (AJCC)[27] or the International Federation of Gynecology and Obstetrics (FIGO)[28] staging guidelines based on tumor size and spread (T), degree of lymph node involvement (N), and extent of metastatic progression (M). In stage I EOC, cancer remains confined to the ovary or fallopian tubes, while stage II involves spread to other nearby pelvic organs including the uterus, bladder, colon, or rectum[27,28]. Stage III EOC includes further spread to retroperitoneal (pelvic or para-aortic) lymph nodes, while stage IV may involve invasion into spleen or liver, advanced lymph node involvement beyond retroperitoneal lymph nodes, and metastases to distant organs outside of the peritoneal cavity such as lungs or bone[27,28]. Approximately 30% of HGSOC patients present with excessive accumulation of peritoneal fluid (*i.e.* ascites) containing cancer cells that have shed from the primary tumor[29], which may facilitate metastasis within and across the peritoneal cavity (*i.e.* transcoelomic metastasis)[30]. Interestingly, metastatic deposits of HGSOC frequently occur at sites predicted by the natural current of ascitic fluid within the peritoneal cavity, such as the greater omentum (*i.e.* a fold of peritoneal membrane descending from the stomach and across the intestines), the subdiaphragmatic region, and the pouch of Douglas (the region of peritoneum between the rectum and uterus)[30,31].

At stages I and II, surgery can often result in complete tumor resection and 5-year relative survival rates can be as high as 92%[32]. In contrast, at advanced stages, surgery is not expected to be curative, but is performed for debulking purposes (*i.e.* to minimize residual disease) to enhance

the efficacy of subsequent chemotherapy[5]. Frontline chemotherapy for all EOC histotypes includes a taxane (*e.g.* paclitaxel) coupled with a platinum agent (*e.g.* carboplatin) with or without the addition of an angiogenesis inhibitor (*e.g.* bevacizumab)[33]. While many HGSOC patients are initially chemoresponsive, ~75% of patients will relapse within 18 months[6]. In cases where patients are deemed platinum resistant (*i.e.* relapse within 6 months of initial treatment[5]), the use of secondary agents such as gemcitabine[34], pegylated liposomal doxorubicin (Caelyx)[35], or topotecan[36] may prolong survival, but is not typically curative[5].

Importantly, cancer stage at diagnosis varies between the different EOC histotypes. Serous ovarian cancers, which are largely HGSOCs, are most often diagnosed at stage III (51% of cases) or IV (29% of cases)[2]. The late stage at diagnosis contributes to a poor overall prognosis for serous ovarian cancers, with 5-year survival rates of ~42% and ~26% for stages III and IV respectively, or ~43% for all stages combined[2]. HGSOC patients often remain asymptomatic until the disease has reached an advanced stage or present with nonspecific symptoms which contributes to the delayed diagnosis[37–39]. In contrast, endometrioid, clear cell, and mucinous ovarian cancers are frequently diagnosed at early stages (58-64% diagnosed at stage I) and are associated with more favorable overall 5-year survival rates (82%, 71%, and 66%, respectively)[2]. Thus, the late stage of diagnosis and the prevalence of drug resistance in HGSOC are two major factors that account for its high mortality rates. To better combat these negative associations requires an understanding of the molecular mechanisms contributing to HGSOC pathogenesis.

1.1.3. Molecular Pathogenesis of High-Grade Serous Ovarian Cancer (HGSOC)

As described above, HGSOC is a Type II tumor characterized by a complex genetic landscape. Nonsense or missense *TP53* mutations are present in > 96% of HGSOC samples, making them the most common genetic alterations observed in HGSOC[24,40,41]. Importantly, *TP53*

mutation is the earliest known event in the pathogenesis of HGSOC and can be detected in precursor lesions within the fallopian tube epithelium[13,42]. A "*TP53* signature" refers to a stretch of fallopian tube secretory epithelial cells that exhibit strong TP53 staining via immunohistochemistry (IHC) with evidence of DNA damage, but otherwise appear benign[12,43]. Some *TP53* signatures may progress to serous tubal intraepithelial carcinomas (STICs), which are further characterized by dysplasia and an increased proliferative capacity[12,43]. The subsequent migration of these cells to the ovarian surface epithelium is what ultimately gives rise to ovarian carcinoma in these cases[12,43] (Fig. 1-1). Progression from a STIC lesion to an ovarian carcinoma may take as long as 7 years, which appears to be followed by a relatively rapid onset of metastasis beyond the ovary[10]. Importantly, STIC lesions and corresponding HGSOCs harbor the same *TP53* mutations, which provides evidence of the fallopian tube origin of HGSOC[13,42]. However, STIC lesions are not identified in all HGSOC patients, and more recent models suggest that ovarian carcinomas may occur directly from an "early serous proliferation" rather than a tubal carcinoma (referred to as a "precursor escape" model)[44]. Following acquisition of a *TP53* mutation, it is thought that additional genetic alterations are required for tumorigenesis and metastatic progression.

Another common class of genetic alterations in HGSOC includes defects in DNA homologous recombination repair (HRR) genes, which are present in ~50% of HGSOCs[24,45,46]. The majority of these HRR defects are due to inactivating mutations in *BRCA1* (~12%)[24] or *BRCA2* (~11%)[24], as well as *BRCA1* promoter hypermethylation (~11%)[24]. Alterations in additional HRR pathway members, including *ATM*, *ATR*, *RAD51C*, *PTEN* and *EMSY* collectively occur in ~25% of HGSOCs[24]. Importantly, germline HRR defects confer an increased lifetime risk of developing ovarian cancer[47]. For example, germline *BRCA1* or *BRCA2* mutations (which occur in ~13-17%

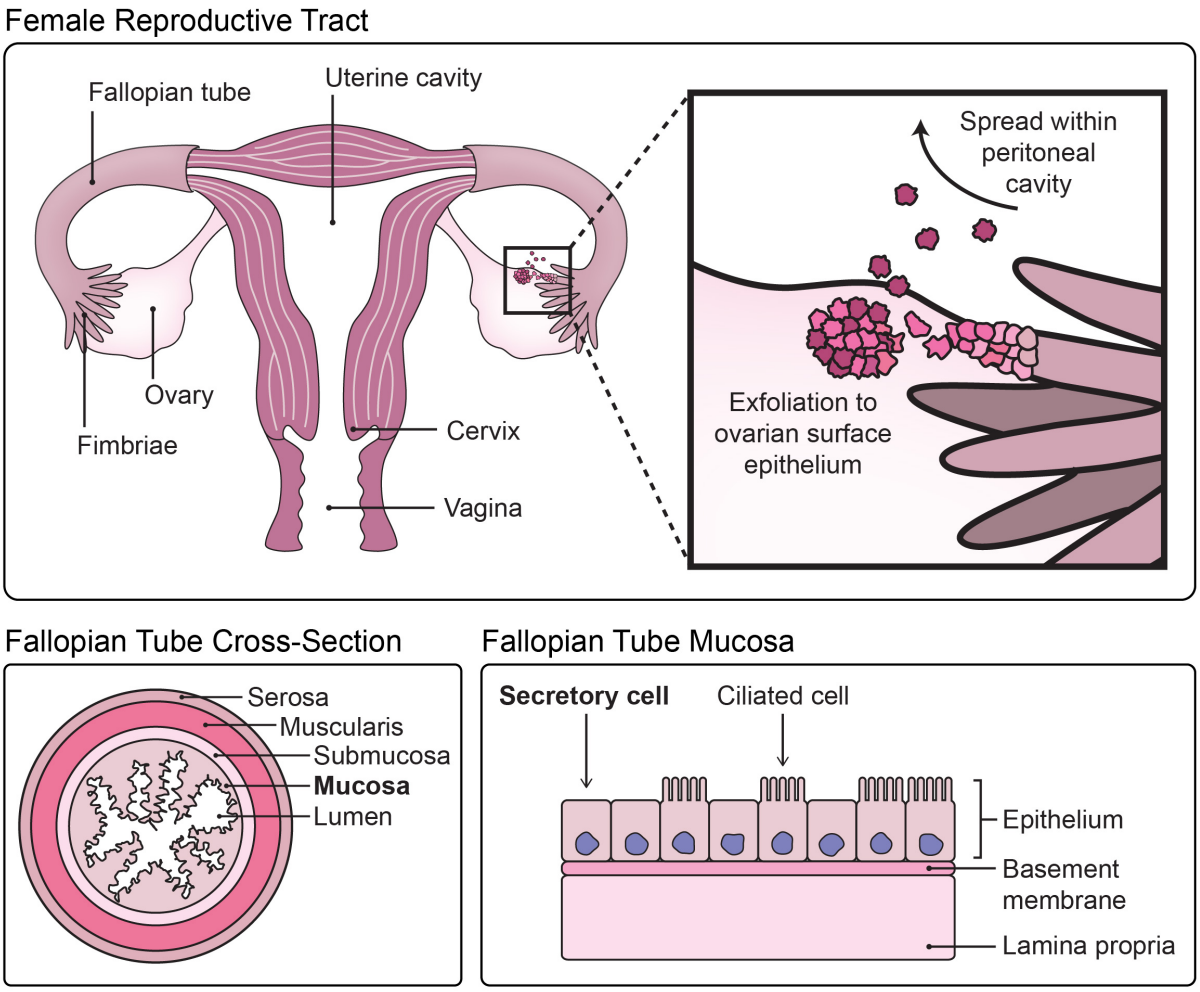

Figure 1-1. Fallopian Tube Secretory Epithelial Cells are Precursors for HGSOC.
A schematic depicting the organs, tissues, and cells involved in the pathogenesis of HGSOC. HGSOCs originate from dysplastic precursor lesions at the fimbriated end of the fallopian tube, which spread to the nearby ovarian surface epithelium, forming an ovarian tumor (top panel). A cross-sectional view of the fallopian tube shows four major tissue layers (bottom left panel). The epithelium of the innermost mucosal layer is composed of two major cell types: secretory cells and ciliated cells (bottom right panel). The secretory cells of the inner fallopian tube epithelium are the cells of origin for HGSOC.

of HGSOC patients[24,47]) confer lifetime risks of ovarian cancer as high as 54% for *BRCA1* and 23% for *BRCA2*[48] compared to 1.3% in the general population[1]. Consequently, many individuals harboring germline *BRCA1/2* mutations undergo prophylactic bilateral salpingo-oophorectomy (surgical removal of both fallopian tubes and ovaries)[49]. The biological specimens from these women have provided insight into the early etiology of HGSOC, including the important discovery that precursor lesions for HGSOC are found within the distal fallopian tube epithelium rather than the ovarian surface epithelium[11].

In addition to the genetic alterations described above, genomic characterization of HGSOC has revealed widespread somatic gene copy number alterations[24,50] and structural rearrangements[51]. These include *CCNE1*, *MYC*, and *MECOM* copy number amplifications, *NF1* and *RB1* deletions, structural rearrangements affecting *NF1* and *RB1*, and many additional low-frequency alterations[24,51]. *CCNE1* gene amplification occurs in ~20% of HGSOCs, and is an early event in HGSOC pathogenesis[50]. Interestingly, *CCNE1* amplifications are mutually exclusive with *BRCA1/2* mutations[24,52], and synthetic genetic targeting of *BRCA1* is lethal in cells harboring *CCNE1* amplifications[53] (*i.e. BRCA1* and *CCNE1* are synthetic dosage lethal interactors[54]). In addition, HGSOCs harboring *CCNE1* amplifications are associated with primary platinum resistance[55] and poor prognosis[56]. These data suggest that *BRCA1/2* mutation and *CCNE1* amplification may represent two distinct pathways towards cancer development[52]. In general, characterizing the genetic landscape of HGSOC is critical to improve our fundamental understanding of disease etiology, but there remain many unanswered questions such as: 1) What are the mechanisms underlying the observed genomic complexity in HGSOC?; 2) Which genetic alterations are important drivers of HGSOC development?; and 3) What accounts for the rapid disease progression and emergence of drug resistance in HGSOC?

1.2. CHROMOSOME INSTABILITY (CIN) IN CANCER

Genome instability is an enabling feature of cancer[57] that refers to a state of increased mutations, copy number changes and epigenetic alterations within a cell[58]. Genome instability exhibits critical roles in cancer initiation, progression, evolution and drug resistance and is characteristic of virtually all cancer types[59]. Traditionally, genome instability has been categorized into three distinct forms: 1) microsatellite instability; 2) CpG island methylator phenotype; and 3) chromosome instability (CIN)[58]. While microsatellite instability arises from defects in DNA mismatch repair genes (*MLH1*, *MSH2*, *MSH6*, and *PMS2*) that underlie DNA mismatches and expansions and/or contractions of repetitive DNA sequences termed microsatellites[60], CpG island methylator phenotype is characterized by extensive DNA methylation at CpG dinucleotides within promoter regions leading to transcriptional silencing[61]. CIN is a third form of genome instability and is defined as an increase in the rate at which whole chromosomes or large parts thereof are gained or lost[58].

Collectively, all three forms of genome instability contribute to cancer pathogenesis by altering the expression and/or encoded functions of key genes, and thus are significant contributors to the pervasive aberrant genetic and epigenetic landscapes found within cancer cells[58,62]. CIN has a particularly profound impact on genome stability by inducing simultaneous and ongoing copy number changes in large cohorts of genes, some of which may be important in cancer development (*e.g.* oncogenes, tumor suppressor genes, DNA repair genes and apoptotic genes)[63–65]. Thus, CIN is a dynamic process that increases the probability of acquiring the myriad of genetic changes required to initiate and drive the development and progression of cancer[66–68].

1.2.1. CIN Drives Intratumoral Heterogeneity and Cancer Evolution

The chromosomal alterations associated with CIN can be broadly classified as either numerical (N-CIN), involving gains and/or losses of whole chromosomes, or structural (S-CIN), involving amplifications, deletions, inversions, and translocations of chromosomal regions that can range in size from single genes to whole chromosome arms, however these two classes are not mutually exclusive[58,69,70] (Fig. 1-2). Conceptually, the ongoing chromosome gains, losses, or structural alterations associated with CIN promote the production of genetically distinct (*i.e.* heterogeneous) populations of daughter cells[58]. Thus, within the context of cancer, CIN increases intratumoral heterogeneity, which under certain conditions may confer a selective or growth advantage (*e.g.* increased cell proliferation, metastatic potential, or intrinsic drug resistance) to a subpopulation of cells[71] (Fig. 1-3). For example, under certain selective pressures (*e.g.* chemotherapy), cells harboring a specific growth advantage *(e.g.* drug resistance) will continue to proliferate and may ultimately produce a highly aggressive and/or drug-resistant tumor[72]. Accordingly, CIN is proposed to play a critical role in cancer evolution by increasing population diversity, or by conferring new capabilities. Thus, it is not surprising that CIN is frequently associated with disease recurrence and poor patient outcomes[71,73]. However, rates of chromosomal changes (*i.e.* the level of CIN) can vary between different cancer types or within a given tumor[58,74], and in certain cancer contexts, extensive levels of CIN are associated with more favorable outcomes (*e.g.* in some ovarian, breast, gastric, and lung cancers)[75,76]. It has been suggested that a maximum CIN threshold may exist that is favourable for tumor survival and growth, but extreme CIN beyond this threshold may not be compatible with tumor cell viability and thus, cancer cells with inherently high levels of CIN die and are lost from the population[77,78].

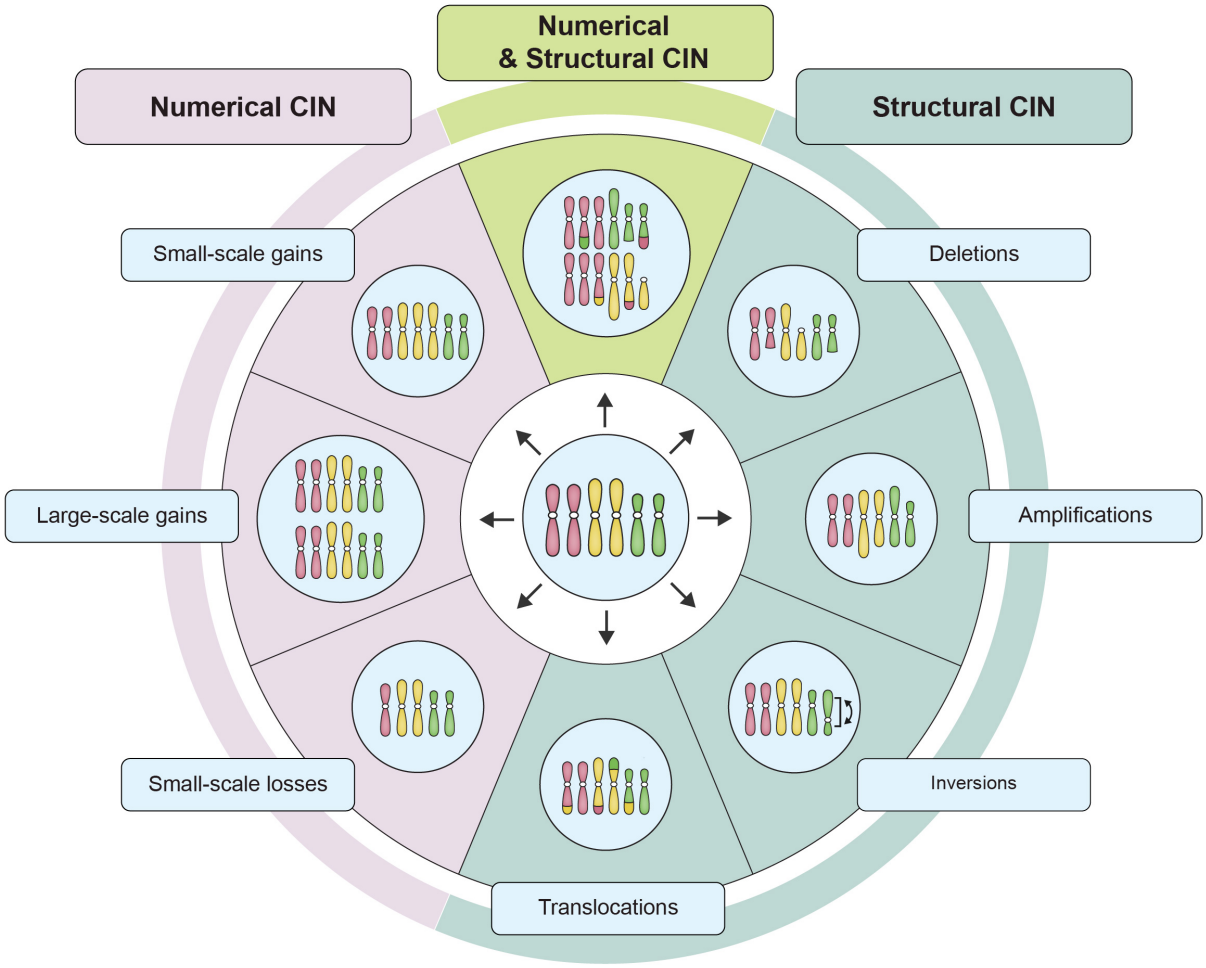

Figure 1-2. Examples of N-CIN and S-CIN.
A schematic depicting examples of the types of karyotypic changes associated with either N-CIN or S-CIN. Note that a single aberrant karyotype is not sufficient to define CIN, as CIN is characterized by ongoing karyotypic change and increased cell-to-cell karyotypic heterogeneity. For illustrative purposes, the starting diploid cell (center) only contains three pairs of chromosomes (*i.e.* a partial karyotype). N-CIN involves whole chromosome gains or losses, including small-scale changes that result in aneuploidy, as well as large-scale polyploidization events. S-CIN includes partial chromosome deletions, amplifications, inversions, or translocations. These different classes of N-CIN or S-CIN are often combined to produce complex karyotypes that evolve over time.

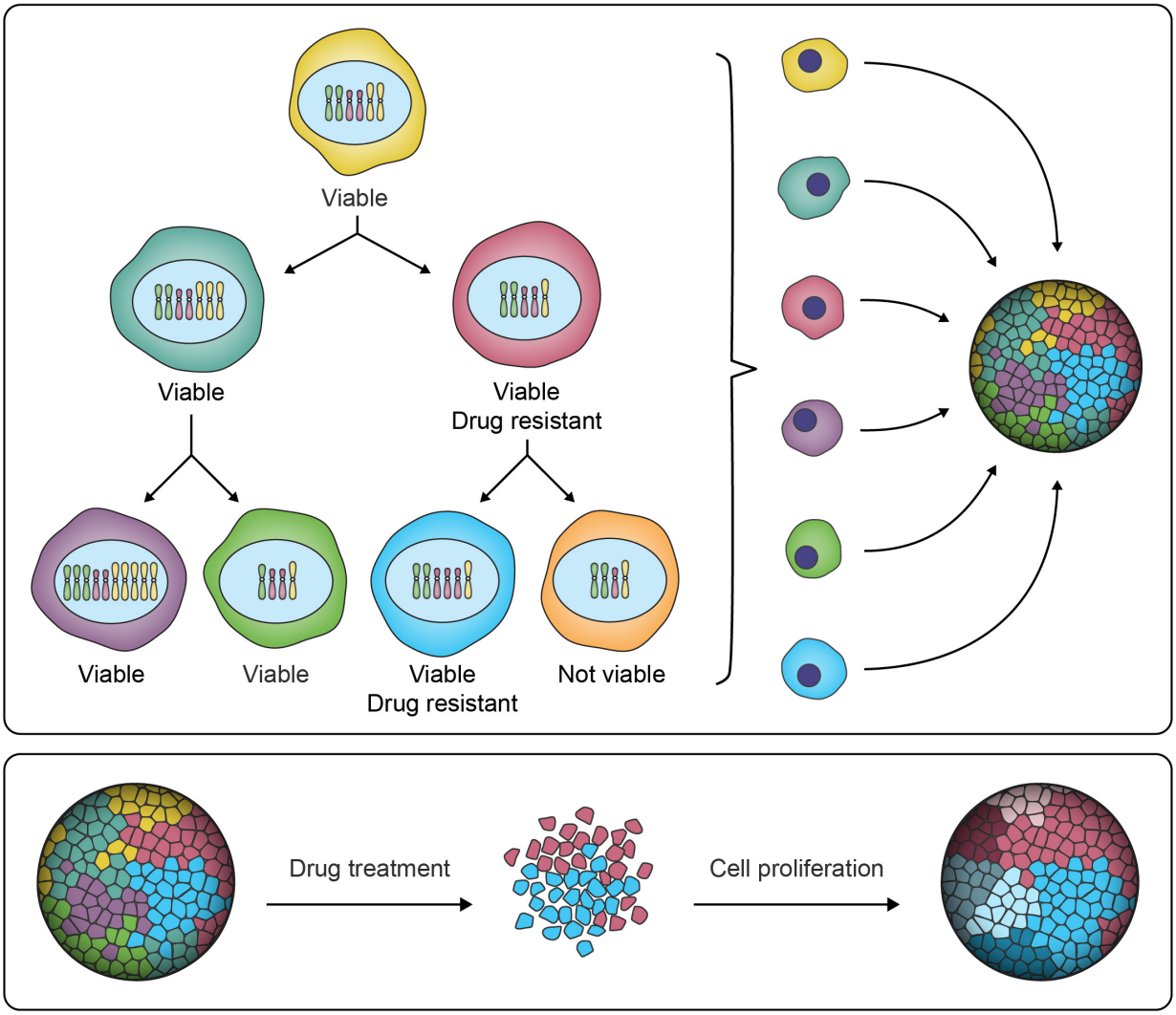

Figure 1-3. CIN Drives Intratumoral Heterogeneity and Cancer Evolution.
A schematic depicting a hypothetical example of CIN within an initial cell that for illustrative purposes contains only three pairs of chromosomes (*i.e.* a partial karyotype). As this cell undergoes two rounds of cellular division, chromosomes are gained or lost, producing a heterogeneous population of genetically distinct daughter cells, which underlies intratumoral heterogeneity. Some chromosome complements may not be compatible with cell viability, as indicated by the orange cell that is lost from the population. Other chromosome complements may confer selective advantages under defined environmental conditions. In this example, the pink and blue cells have acquired drug resistance capabilities, which allows them to survive and proliferate under a drug treatment that kills the other cells. Thus, the chromosome gains and losses driven by CIN result in a complex and heterogeneous tumor with high evolutionary potential. Note that while this example is focused on small-scale gains/losses of whole chromosomes (N-CIN), chromosome complements may also evolve via increases in ploidy (N-CIN) or structural chromosome changes (S-CIN), and often include a combination of both N- and S-CIN.

In general, the heterogeneity driven by CIN contributes to a complex cell population with high evolutionary potential.

1.2.2. Relevance and Potential Origins of CIN in HGSOC

While HGSOC is often referred to as a "genetically unstable" tumor type with a complex genomic landscape[25,43,79–82], to date there is only one study that has directly assessed the prevalence of CIN in HGSOC[83]. In this study, primary HGSOC samples were isolated from patient ascites, which were collected at various timepoints over the course of disease[83]. Importantly, all samples evaluated within this study exhibited CIN, and an increased level of CIN coincided with the emergence of drug resistance and disease recurrence[83]. Thus, these findings provide preliminary insight into the role CIN may play in the evolution of HGSOC at late stages of disease. Beyond this study, genetic and molecular data suggest that CIN may also play a role in early HGSOC development. Some of the strongest evidence supporting this possibility involves the aberrant expression and function of *CCNE1* (Cyclin E1), which is frequently amplified at the level of the genome and/or overexpressed at the level of the protein in early precursor lesions and in corresponding HGSOCs[50,84]. Cyclin E1 is a cell cycle regulatory protein that is important for G1 to S phase transition[85], and has additional roles in DNA replication and centrosome biology[86]. It exerts these functions by binding and activating cyclin-dependent kinase 2 (CDK2), thereby enabling the phosphorylation of downstream target proteins[87]. For example, phosphorylation of RB by Cyclin E1/CDK2 enables the initiation of S phase via E2F gene transcription[87], and phosphorylation of CP110 triggers centrosome duplication[88]. This time-sensitive control over the cell cycle is regulated by Cyclin E1 abundance, where Cyclin E1 levels peak during G1 and S phase and subsequently decline due to proteolytic degradation of Cyclin E1[89].

Importantly, Cyclin E1 overexpression induces CIN in various cancer contexts[90,91]. Many HGSOCs and HGSOC precursors harbor supernumerary centrosomes (*i.e.* > 2 centrosomes/cell), which is associated with *CCNE1* amplification[84]. In general, aberrant centrosome duplication results in the formation of abnormal multipolar mitotic spindles, leading to aberrant mitotic events including chromosome segregation errors (Fig. 1-4)[92]. Thus, inducing supernumerary centrosomes is one mechanism by which Cyclin E1 overexpression may induce CIN in HGSOC. In addition, Cyclin E1 overexpression induces replication stress (*i.e.* replication-associated DNA damage) either due to premature S-phase entry in the presence of insufficient nucleotide (nt) pools resulting in replication fork collapse[93], or due to increases in replication initiation and interference between replication and transcription machinery[94]. Cyclin E1 overexpression also induces aberrant phosphorylation of the centromeric protein CENP-A leading to increases in mitotic defects and CIN phenotypes[95]. As highlighted above, genomic amplification of *CCNE1* occurs in ~20% of HGSOCs[96], which often correlates with overexpression at the level of the protein[97]. Interestingly, Cyclin E1 protein overexpression is observed in ~45-50% of HGSOCs[97,98], suggesting that additional mechanisms leading to the overexpression of Cyclin E1 may be fundamentally implicated in HGSOC pathogenesis. For example, aberrant protein turnover is one possible mechanism by which Cyclin E1 may be overexpressed.

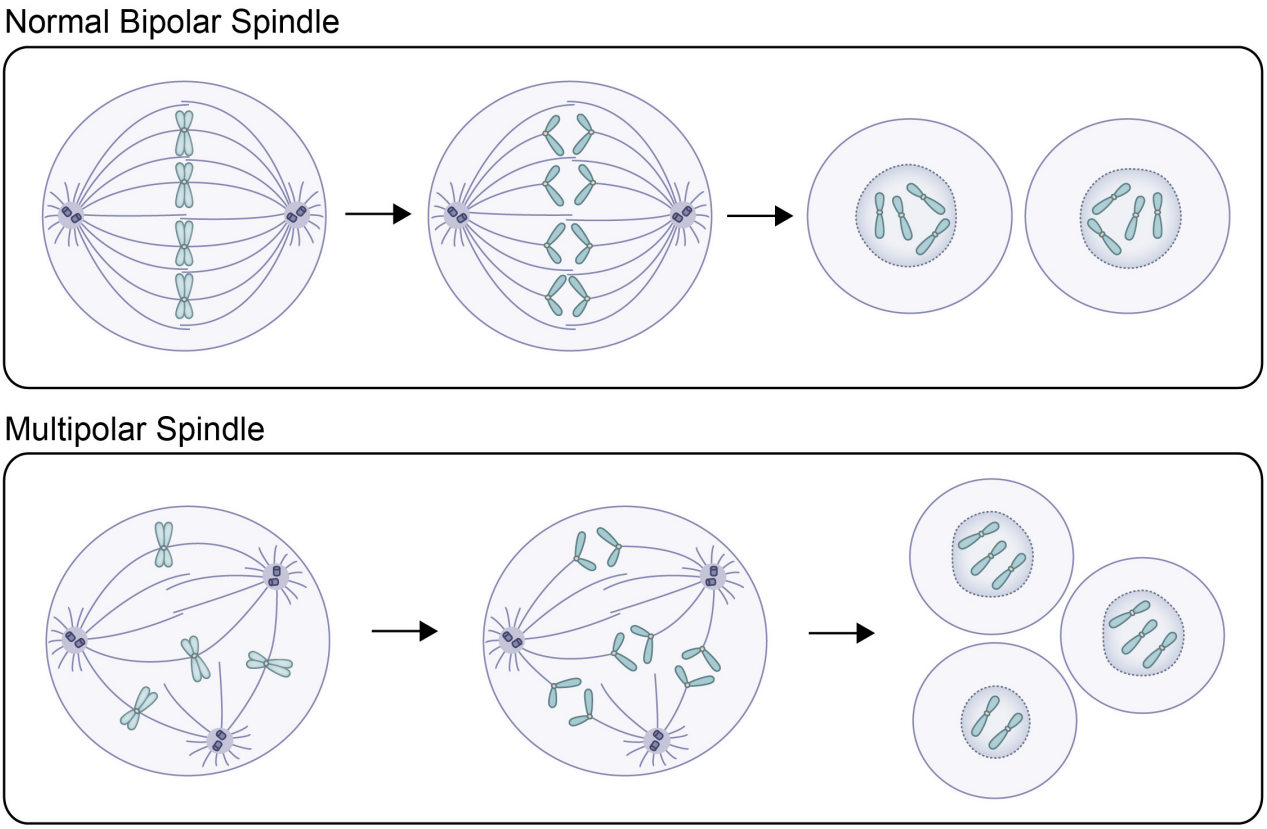

Figure 1-4. Aberrant Mitotic Spindle Dynamics are a Mechanism of CIN.
Schematic depicting mitotic chromosome segregation in a cell with a normal bipolar mitotic spindle (top panel) and with an abnormal multipolar spindle (bottom panel). For illustrative purposes, the initial cell contains only four chromosomes post-DNA replication. Under normal conditions (top panel), chromosomes align at the metaphase plate and segregate equally to the two spindle poles, generating two daughter cells with equal numbers of chromosomes (*i.e.* both diploid). In contrast, a multipolar spindle may result in aberrant mitoses characterized by abnormal chromosome attachment to microtubules, congression defects, and segregation errors, leading to abnormal (aneuploid) chromosome complements within the resulting daughter cells which may or may not be compatible with viability (bottom panel).

1.3. THE SKP1-CUL1-FBOX (SCF) COMPLEX

The ubiquitin-proteasome pathway represents the major mechanism mediating targeted intracellular protein turnover[99]. This pathway involves the conjugation of ubiquitin to protein substrates within the cell (*e.g.* Cyclin E1, detailed below), which targets them for proteolytic degradation[99]. The transfer of ubiquitin to a target substrate involves three steps, each catalyzed by a unique enzyme: 1) an E1 enzyme facilitates ATP-dependent ubiquitin activation; 2) activated ubiquitin is transferred to an E2 ubiquitin conjugating enzyme; and 3) the E2 enzyme is recruited to an E3 ubiquitin ligase, which catalyzes the polyubiquitination of the target substrate. The resulting polyubiquitin chain is linked through lysine 48 (K48)-glycine 76 (G76) isopeptide bonds, which is recognized by the 26S proteasome[100].

There are predicted to be ~1000 distinct E3 ubiquitin ligases in humans, which are divided into four major groups: 1) the Homologous to the E6-AP Carboxyl Terminus (HECT); 2) U-box; 3) Plant-homeo-domain (PHD)-finger; and 4) Really Interesting New Gene (RING)-finger type[101]. Several subfamilies exist within the family of RING-finger type E3 ubiquitin ligases, including the cullin-based subfamily[101] (see Section 1.3.2). Importantly, the SKP1-CUL1-F-box protein (SCF) E3 ubiquitin ligase (SCF) complex is a cullin-based RING-finger type E3 ubiquitin ligase that is involved in the degradation of Cyclin E1 and other substrates[102] (Fig. 1-5). The SCF complex is composed of four protein subunits, three of which are invariable core components (RING box protein 1 [RBX1], S-phase kinase associated protein 1 [SKP1], and cullin 1 [CUL1]) and one of which is a variable F-box protein that confers substrate specificity[102]. The current study focuses on two of the core SCF complex components, namely SKP1 and CUL1, and their potential roles in regulating chromosome stability via Cyclin E1.

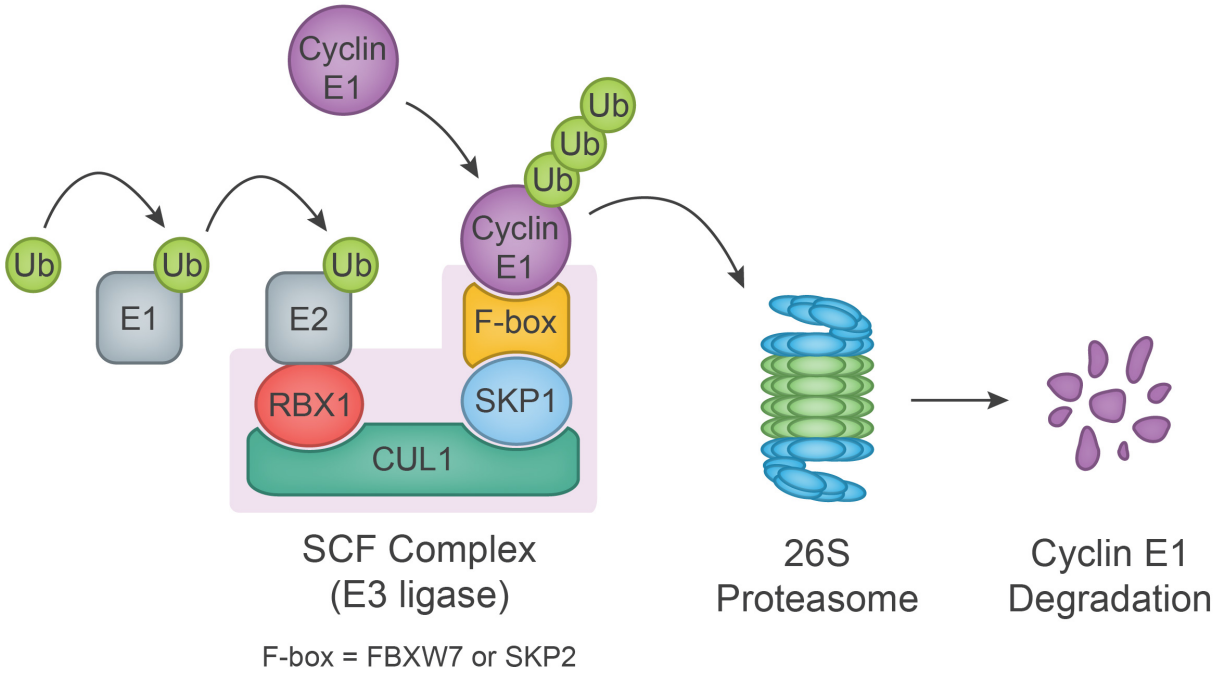

Figure 1-5. Regulation of Cyclin E1 levels by the SCF Complex.
A schematic illustrating the SCF complex-mediated polyubiquitination and subsequent proteasomal degradation of Cyclin E1. The SCF complex consists of four protein subunits: RBX1, CUL1, SKP1 and an F-box protein. There are 68 different F-box proteins that recognize distinct sets of substrates. The F-box proteins involved in regulation of Cyclin E1 levels are FBXW7 and SKP2.

1.3.1. S-phase Kinase Associated Protein 1

Within the SCF complex, SKP1 serves as an adapter protein that links one of 68 distinct F-box proteins to CUL1[103]. Human *SKP1* maps to chromosome 5q31.1 and contains 5 exons spanning ~28 kb of genomic DNA[104]. *SKP1* encodes two distinct protein isoforms of 163 and 160 amino acids (aa) respectively, both with a mass of ~18 kilodaltons (kDa). The larger 163 aa isoform is believed to be the most functionally relevant, as it includes a tryptophan residue (aa 159) that was shown in an orthologous *Saccharomyces cerevisiae* model to be essential for *in vivo* function[105].

The role of the SCF complex in regulating Cyclin E1 levels suggests that altered expression or function of SKP1 and other SCF complex components may lead to the misregulation of Cyclin E1 turnover and result in CIN. Indeed, in an siRNA-based screen of 168 potential human CIN genes identified through cross-species approaches, *SKP1* was identified as a top candidate (McManus laboratory, unpublished observations). Further validation experiments showed that *SKP1* silencing corresponded with increases in Cyclin E1 levels and CIN phenotypes, confirming *SKP1* is a *bona fide* human CIN gene within a colorectal cancer (CRC) context (McManus laboratory, unpublished observations). Importantly, heterozygous loss of *SKP1* occurs in ~46% of HGSOCs[24] and in a variety of additional cancer types (Table 1-1)[106–109], but the impact of these alterations on HGSOC pathogenesis are completely unknown.

Interestingly, homozygous loss of *SKP1* is a relatively rare event (occurring in only ~0.2% of HGSOCs[24]), and insights from model organisms suggest that *SKP1* is an essential gene. For example, homozygous loss of *SKP1* orthologs is lethal in *Drosophila melanogaster*[110] and *S. cerevisiae*[111]. In *Caenorhabditis elegans,* which harbors 21 *SKP1*-related genes (*i.e. skr* genes)[112], silencing of individual genes led to a variety of phenotypes including embryonic

Table 1-1. Frequency of Somatic *SKP1* Alterations in Five Cancer Types[24,106–109]

Cancer Type	Number of New Cases in North America Annually[A]	Frequency of:				Number of North Americans with Altered *SKP1* Annually[E]
		Deep Deletion (%)[B]	Shallow Deletion (%)[C]	Mutation (%)	Total Alterations (%)[D]	
Ovarian	25,530	0.2	46.0	0	46.2	11,795
Breast	298,470	0.2	17.0	0	17.2	51,337
Colorectal	171,900	0	15.6	0.4	16.0	27,504
Lung	257,450	0.9	39.1	0	40.0	102,980
Stomach	31,610	2.4	26.4	0	28.8	9,104
					Total	**202,720**

[A]Estimated incidence of newly diagnosed individuals in Canada (2019)[1] and the United States (2019)[113].
[B]Frequency of copy number alterations suggesting homozygous loss.
[C]Frequency of copy number alterations suggesting heterozygous loss.
[D]Combined frequency of deep deletion, shallow deletion, and mutation.
[E]Calculated by the total alteration frequency for a given cancer type multiplied by the total number of newly diagnosed patients.

lethality[114], larval or embryonic cell cycle arrest[112], larval or embryonic hyperplasia[112], and other morphological and growth abnormalities[114]. The impact of Skp1 depletion has also been assessed within a transgenic mouse model expressing a Cul1 deletion mutant (N252), which sequesters and inactivates Skp1[115]. Expression of the transgene within the T-cell lineage resulted in the development of T-cell lymphoma, which was rescued by overexpressing Skp1[115]. In addition, Cul1-N252 cells exhibited a variety of CIN-associated phenotypes including multinucleated cells, centrosome and mitotic spindle abnormalities, and chromosome segregation errors[115]. Collectively, these data suggest that while complete loss of SKP1 expression may not be compatible with cell viability, partial depletion of SKP1 may have a potential role in CIN and cancer initiation.

1.3.2. The Cullin Family of Proteins

Cullin-RING ubiquitin ligases (CRLs) are a class of E3 ubiquitin ligase complexes that contain a cullin protein as one of their subunits[116]. There are eight members of the cullin protein family in humans (cullins 1, 2, 3, 4a, 4b, 5, 7, and 9) that interact with diverse sets of binding partners to form more than 200 distinct CRLs[116]. In their respective CRLs, cullin proteins serve as scaffolds to enable complex assembly[116], and are activated by post-translational modification with NEDD8, a ubiquitin-like protein[117,118]. In general, cullin proteins are comprised of 3 major domains: 1) a C-terminal cullin-homology domain for interaction with a RING finger protein (which binds the E2 enzyme); 2) a neddylation domain; and 3) a variable N-terminal region for interaction with an adapter protein (where substrate binding occurs)[116]. Upon activation, cullin proteins undergo a conformational change that increases proximity between the E2 enzyme and substrate to facilitate ubiquitin transfer[119]. Of the eight human cullins, CUL1 is the best characterized and is a core component of the SCF complex, along with RBX1 as its associated

RING finger protein and SKP1 as its adapter[102]. Human *CUL1* maps to 7q36.1 and contains 22 exons spanning ~103 kb of genomic DNA[104]. *CUL1* encodes a single protein of 776 aa with a molecular mass of ~90 kDa[104].

The role of *CUL1* in regulating chromosome stability has never been evaluated. However, heterozygous loss of *CUL1* is commonly observed in a variety of cancer types (Table 1-2)[106–109], including in ~13% of HGSOCs[24]. Similar to *SKP1*, homozygous loss of *CUL1* is a relatively rare event and only occurs in 0.2% of HGSOCs[24]. In model organisms such as *Mus musculus*[120,121], *C. elegans*[122], and *Arabidopsis thaliana*[123], homozygous loss of *CUL1* orthologs results in embryonic lethality, suggesting it is also an essential gene. In two mouse models, CUL1 loss was associated with increases in Cyclin E1 protein levels[120,121]. Interestingly, *C. elegans* offspring that had access to residual maternal CUL1 protein stored within the oocyte were able to survive until the larval stage, but exhibited significant hyperplasia in all tissues[122]. Overall, further investigation of the role *CUL1* plays in CIN and cancer development is highly warranted.

Table 1-2. Frequency of Somatic *CUL1* Alterations in Five Cancer Types[24,106–109]

Cancer Type	Number of New Cases in North America Annually[A]	Frequency of:				Number of North Americans with Altered *CUL1* Annually[E]
		Deep Deletion (%)[B]	Shallow Deletion (%)[C]	Mutation (%)	Total Alterations (%)[D]	
Ovarian	25,530	0.2	12.9	0	13.1	3,344
Breast	298,470	0.2	13.3	0.2	13.7	40,890
Colorectal	171,900	0	1.9	2.6	4.5	7,736
Lung	257,450	0	13.0	2.2	15.2	39,132
Stomach	31,610	0.7	15.9	5.8	22.4	7,081
					Total	**98,183**

[A]Estimated incidence of newly diagnosed individuals in Canada (2019)[1] and the United States (2019)[113].
[B]Frequency of copy number alterations suggesting homozygous loss.
[C]Frequency of copy number alterations suggesting heterozygous loss.
[D]Combined frequency of deep deletion, shallow deletion, and mutation.
[E]Calculated by the total alteration frequency for a given cancer type multiplied by the total number of newly diagnosed patients.

1.3.3. SCF Complex Substrates are Implicated in CIN Pathways

It is generally accepted that the aberrant genes underlying CIN (*i.e.* CIN genes) normally function within key pathways that orchestrate chromosome dynamics. Indeed, many human CIN genes have been identified that encode functions within DNA replication and repair[69,124], centrosome duplication[125,126], mitotic spindle dynamics[126], kinetochore-microtubule attachment[127,128], sister chromatid cohesion[129–132], chromosome segregation[133], and cell cycle checkpoint pathways[134–136]. In addition, insights from cross-species approaches suggest the presence of many additional CIN genes that encode functions within less intuitive pathways not directly related to chromosome dynamics, such as proteasome function, transfer RNA (tRNA) synthesis, or lipid synthesis[137].

Importantly, the SCF complex regulates the cellular levels of numerous protein targets, many of which are involved in CIN-associated pathways. As highlighted above, Cyclin E1 represents one substrate of interest that is highly relevant in the context of HGSOC. There are two F-box proteins that recognize and bind Cyclin E1: SKP2[138] and FBXW7[91,139]. One study by Rajagopalan *et al.*[91] determined that knockout or silencing of *FBXW7* in a CRC context induced increases in Cyclin E1 levels and CIN phenotypes that were rescued by ~50-70% following *CCNE1* silencing[91]. Similarly, while *SKP1* silencing was shown to induce increases in CIN phenotypes within a CRC context, co-silencing of *SKP1* and *CCNE1* resulted in ~50% phenotypic rescue (McManus laboratory, unpublished observations). These data suggest that disruption of an SCF complex component may induce CIN via increases in Cyclin E1 levels, but Cyclin E1 alone does not fully account for the CIN phenotypes observed. Indeed, there are many additional SCF complex substrates that have roles in CIN-associated pathways including DNA repair proteins (*e.g.* BRCA1[140], BRCA2[141], FANCM[142]), cell cycle regulators (*e.g.* Cyclin D1[143–145], Cyclin A[138]),

and regulators of mitotic spindle dynamics (*e.g.* Aurora kinase A[146], Aurora kinase B[147,148], RASSF1[149]). The roles of SCF complex substrates in CIN and/or cancer have been more comprehensively reviewed elsewhere[150–152].

Overall, perturbation of SCF complex activity by disrupting a core component such as SKP1 or CUL1 is predicted to result in the misregulation of a large number of proteins with diverse cellular functions. Cyclin E1 is the focus of the current study due to its relevance in the pathogenesis of HGSOC, and more broadly, the work presented in this thesis explores the net phenotypic impact diminished *SKP1* or *CUL1* expression has on Cyclin E1 levels, CIN and cellular transformation.

1.4. METHODS OF EVALUATING CIN

Many techniques are capable of identifying gene copy number changes or aneuploidy within pooled cellular samples, including comparative genomic hybridization, single nucleotide polymorphism arrays, polymerase chain reaction-based methods, and flow cytometry. However, these techniques are not sufficient to define CIN within a cellular population. CIN refers to a *rate* of ongoing change that drives cell-to-cell heterogeneity, and is distinct from a static *state* such as aneuploidy. The population averaging associated with the techniques listed above effectively masks the cell-to-cell heterogeneity that is synonymous with CIN. In general, there are two methods used to evaluate CIN: 1) tracking chromosome dynamics within a single cell and its progeny over time, and 2) using single-cell techniques to quantitatively assess the cell-to-cell heterogeneity associated with CIN in a given population of cells. The first method allows for an exact rate of chromosomal gains or losses to be calculated by monitoring chromosomal changes across consecutive cell divisions, which often requires experimental protocols that do not

adversely impact cell proliferation or viability. The second method operates under the premise that the fundamental outcome of CIN is cell-to-cell karyotypic heterogeneity, which can be detected through the use of quantitative, single-cell approaches at a single timepoint. The latter method is more versatile, as it can be applied in traditional endpoint analyses (live or fixed) and on a wider variety of sample types. The CIN assays employed within this thesis fall into this second category.

The most direct way to evaluate N-CIN is to enumerate chromosomes within individual cells (or within mitotic chromosome spreads originating from individual cells) and to quantify the variation in chromosome numbers within a given population/condition. Increased cell-to-cell heterogeneity in chromosome numbers is directly indicative of N-CIN; however, this technique can be laborious and time-consuming, and is best-suited as a validation step rather than an initial screen. Thus, additional single-cell approaches rely on characterizing cell-to-cell heterogeneity in phenotypes or surrogate markers of CIN, such as changes in nuclear areas (NAs)[83,153–156] and increases in micronucleus formation (MNF; the formation of small membrane-enclosed DNA-containing bodies outside of the primary nucleus)[131,157–159]. Conceptually, changes in NAs (increases or decreases) are typically associated with large-scale changes in chromosome numbers or DNA content[154,160–162]. Accordingly, an increase in NA heterogeneity is suggestive of N-CIN[83,153,154,156]. On the other hand, micronuclei typically arise from chromosome missegregation events involving whole chromosomes or large chromosome fragments that fail to incorporate within daughter nuclei following cytokinesis and entry into G1[163]. Thus, increases in MNF are suggestive of N-CIN and/or S-CIN.

A major benefit of the NA and MNF assays is that they are easily adapted to high-content (multiplexed) screens that can be automated with respect to experimental execution and downstream analyses. However, changes in NAs and MNF can also occur independent of CIN.

For example, NAs vary throughout the cell cycle, as G1 nuclei (pre-replication) are smaller than G2 nuclei (post-replication); however, the NA differences observed between G1 and G2 are typically smaller than those that occur in CIN-positive samples[157]. Additionally, as cells progress through the cell cycle, chromosomes contained within a micronucleus may reintegrate within the primary nucleus as cells progress through a subsequent round of mitosis[164]. Overall, the quantitative assessment of NAs and MNF are indirect methods of evaluating CIN that are ideally suited to initial screens, but require validation using complementary approaches such as direct enumeration of chromosomes within mitotic chromosome spreads.

1.5. METHODS OF EVALUATING CELLULAR TRANSFORMATION

Cancer is a complex disease characterized by aberrant and uncontrolled cell growth, proliferation, and dissemination. The behavior of cancer cells is typically defined by six key hallmark capabilities that are not observed within normal cells or tissues: sustaining proliferative signaling, evading growth suppressors, resisting cell death, enabling replicative immortality, inducing angiogenesis, and activating invasion and metastasis[57,165]. Cells that have acquired these hallmark capabilities are said to be "transformed", and consequently have the potential to overcome various types of intrinsic or environmental growth constraints to form a malignant tumor[165]. Thus, "cellular transformation" describes the process by which a cell reaches the transformed state.

Cellular transformation can be directly assessed by evaluating tumorigenicity within a host (*e.g.* in a mouse model). However, there are a variety of additional assays that are commonly employed to assess various cellular transformation-associated phenotypes *in vitro*. These phenotypes include changes in growth or proliferation rates, changes in growth pattern (*e.g.* loss

of contact inhibition resulting in multilayered cell growth), changes in cell morphology, or anchorage-independent growth capacity[166]. In general, evaluating the ability of cells to grow as 3-dimensional colonies within a semi-solid matrix (*e.g.* soft agar) is considered to be the gold-standard *in vitro* assay for assessing cellular transformation, based on the anchorage-independent growth phenotype[166,167]. Normally, adhesion to the extracellular matrix is required for cell survival and proliferation, and cells that are unattached typically undergo cell death via a process known as anoikis[168]. Thus, the ability to grow in an anchorage-independent fashion is an aberrant phenotype that suggests cells may have acquired several of the hallmark capabilities such as resisting cell death and/or sustaining proliferative signaling. This phenotype is highly relevant in HGSOC, where shedding of malignant cells from the primary tumor often leads to growth of free-floating single cells or multicellular aggregates in the peritoneal fluid[29].

Importantly, assessing the molecular requirements underlying cellular transformation *in vitro* requires an appropriate cellular model. Many cell lines commonly employed in research settings are derived from human cancers, and thus are already transformed. In many cases it may be more appropriate to employ an immortalized cell line, which exhibits replicative immortality but otherwise retains aspects of normal cell growth. For example, to model early HGSOC development, cells collected from the fallopian tubes of non-cancer patients have been used to generate immortalized fallopian tube secretory epithelial cell lines (FT cells)[169]. In turn, these cell lines have been employed to model defined genetic alterations suspected to underlie cellular transformation[43,50,170–172]. A similar approach is employed in this thesis to evaluate the impact *SKP1* heterozygous loss has on FT cell transformation.

CHAPTER 2. RATIONALE, HYPOTHESES AND RESEARCH AIMS

2.1. RATIONALE

HGSOC is the most common EOC histotype as well as the most lethal[173]. The high mortality rates associated with HGSOC can largely be attributed to a lack of reliable early detection methods as well as high frequencies of drug resistance at later stages of disease. Importantly, CIN (an increased rate of chromosome gains and/or losses)[174] is suspected to be implicated in both early and late stages of disease, but is just beginning to be evaluated in ovarian cancer contexts[83]. This study seeks to understand the underlying mechanisms that may be responsible for inducing CIN in HGSOC precursor cells (*i.e.* FT cells) and the extent to which CIN contributes to early disease development.

Genomic amplification of *CCNE1* occurs in ~20% of HGSOCs[24] and is an early event driving HGSOC pathogenesis[50,84,175]. In most of these cases, genomic amplification correlates with Cyclin E1 protein overexpression[97], which is a known mechanism of CIN in other cancer types[90,91]. Cyclin E1 overexpression occurs in up to ~45-50% of HGSOCs[97,98], suggesting that additional aberrant mechanisms leading to the overexpression of Cyclin E1 protein may be implicated in HGSOC pathogenesis. Cyclin E1 protein expression levels are normally regulated by the SCF complex, which includes the proteins SKP1 and CUL1. Diminished *SKP1* expression induces increases in Cyclin E1 levels and CIN phenotypes in CRC cells (McManus laboratory, unpublished observations), but its impact in HGSOC remains unknown. Additionally, the impact diminished *CUL1* expression has on Cyclin E1 and CIN has never been evaluated in any context.

Gene silencing via siRNA is an efficient method to target a gene of interest and suppress its expression to very low levels, making it an excellent tool for functional studies investigating the roles SKP1 and CUL1 have in regulating Cyclin E1 levels and CIN (Aim 1). However,

siRNA-based silencing approaches are transient and are best-suited for short-term experiments. In addition, siRNA-based approaches cannot be used to model precise genetic alterations and/or diminish protein expression to a precise level. Interestingly, data from model organisms and human cancers suggest that complete depletion of SKP1 (Section 1.3.1.) or CUL1 (Section 1.3.2.) is not compatible with cell viability, but partial depletion may be implicated in CIN and cancer development. For example, heterozygous loss of *SKP1* is observed in a variety of cancer types including in ~46% of HGSOCs, while homozygous loss is rarely observed (0.2% of HGSOCs)[24]. Accordingly, to complement the siRNA-based approaches described above, a CRISPR/Cas9 approach will be employed to generate stable *SKP1* heterozygous knockout (*SKP1*$^{+/-}$) cells, which will be used to assess long-term changes in CIN and cellular transformation phenotypes (Aim 2).

2.2. HYPOTHESES AND RESEARCH AIMS

I hypothesize that diminished *SKP1* or *CUL1* expression will lead to increased Cyclin E1 levels that will induce CIN in HGSOC precursor cells and prime these cells for cellular transformation. I will assess this hypothesis through the following two Research Aims.

Aim 1: To evaluate the impact *SKP1* or *CUL1* silencing has on Cyclin E1 levels and CIN.

Aim 2: To evaluate the impact heterozygous loss of *SKP1* has on CIN and FT cell transformation.

CHAPTER 3. MATERIALS AND METHODS

3.1. REAGENTS

All reagents and solutions employed within this study are listed in Appendix A.

3.2. CELL CULTURE

The characteristic features of the four cell lines employed within this study are summarized in Table 3-1. HCT116 CRC cells and OVCAR3 HGSOC cells were purchased from American Type Culture Collection (Rockville, MD). Two FT cell lines, FT194 and FT246, were generated by Dr. R. Drapkin (University of Pennsylvania, USA) and generously provided by Drs. G. DiMattia and T. Shepherd (University of Western Ontario, Canada) with permission. HCT116 cells were cultured in modified McCoy's 5A medium (HyClone) supplemented with 10% fetal bovine serum (FBS) (Sigma-Aldrich). OVCAR3 cells were cultured in Roswell Park Memorial Institute-1640 (RPMI-1640) medium supplemented with 10% FBS and 0.01 mg/mL insulin (Gibco). FT194 and FT246 cells were cultured in Dulbecco's modified Eagle's medium/Nutrient mixture F12 medium (DMEM/F12; Gibco) supplemented with 2% Ultroser G (USG) serum substitute (Pall Corp.) (Appendix A).

Table 3-1. Properties of Human Cell Lines Employed in this Thesis.

Cell Line	HCT116	FT194	FT246	OVCAR3
Organism	Human	Human	Human	Human
Tissue/Cell Type	CRC	FT	FT	HGSOC
Transformed vs. Immortalized	Transformed	Immortalized	Immortalized	Transformed
Properties	Adherent	Adherent	Adherent	Adherent
Gender	Male	Female	Female	Female
Growth Medium	McCoys 5A + 10% FBS	DMEM/F12 + 2% USG	DMEM/F12 + 2% USG	RPMI-1640 + 10% FBS + 0.01 mg/mL Insulin
Doubling Time	~22 hours	~24 hours	~36 hours	~48 h
Modal Karyotype	45, XY Stable	46, XX Stable	46, XX Stable	Near triploid, Unstable
Source	American Type Culture Collection (Rockville, MD)	Dr. R. Drapkin (University of Pennsylvania)	Dr. R. Drapkin (University of Pennsylvania)	American Type Culture Collection (Rockville, MD)

3.2.1. Cell Passaging

Cells were grown in 10 cm tissue culture plates (Sarstedt) in a humidified 37°C incubator containing 5% CO_2. A dish containing cupric sulfate pentahydrate was placed at the base of the incubator to generate humidity and provide protection from microbial/fungal growth (Appendix A). Cells were passaged in a biological safety cabinet every 3-4 days. Briefly, medium was aspirated from the tissue culture dish and adhered cells were washed with sterile phosphate buffered saline (1× PBS) (Appendix A). To detach cells from the plate, 1.5 mL of 0.05% trypsin containing ethylenediaminetetraacetic acid (EDTA) (Gibco; Life Technologies) was added and plates were incubated for 5 minutes (min) at room temperature (RT) for HCT116 and FT194 cells or at 37°C for OVCAR3 and FT246 cells. Cell detachment was assessed using an inverted ID03 microscope (Zeiss) equipped with a 10× objective. To neutralize trypsin, 3 mL of complete medium and 3 mL of 1× PBS were added to the plate. Cells were washed from the bottom of the plate, collected in a 15 mL conical tube (Sarstedt), and pelleted by centrifugation at 140 × g at 21°C for 5 min in a Legend XFR centrifuge (Thermo Scientific). The supernatant was discarded and the cell pellet was resuspended in 5 mL (HCT116, FT194) or 3 mL (OVCAR3, FT246) of 1× PBS. Approximately 1 mL of cell suspension was added back to the 10 cm plate containing 10 mL of fresh complete medium. Cell culture dishes were returned to the incubator.

3.2.2. Cell Counting and Seeding

Cell passaging was performed as above to detach, pellet, and resuspend cells in 1× PBS. To eliminate cell aggregates and obtain a single-cell suspension, cells were passed through a 40 μm cell strainer (Falcon) into a 50 mL conical tube (Sarstedt). A 40 μL aliquot of the cell suspension was mixed in a 1:1 ratio with 0.2% trypan blue dye (Gibco) and a 10 μL volume of the cell/trypan blue mixture was dispensed into a cell counter slide (Cedex Smart Slide, Roche) in

duplicate. Cell counts (*i.e.* the number of viable cells/mL in the cell suspension) were determined using a Cedex XS cell counter and Cedex XS software (Roche), which automatically distinguishes live cells from dead cells based on trypan blue dye exclusion. The average viable cell count was used to calculate the dilution of cells needed for all subsequent experiments.

3.2.3. siRNA Transfection

Sets of four ON-TARGETplus siRNA duplexes targeting distinct mRNA coding regions for *SKP1* or *CUL1* and a non-targeting control siRNA were purchased from Dharmacon. Each siRNA duplex was resuspended in 1× siRNA buffer (Appendix A) to achieve a stock concentration of 20 μM and a working concentration of 10 μM. A pooled siRNA for each gene was prepared by combining equal volumes of all four distinct 10 μM siRNA duplexes. All siRNAs were stored in small aliquots at -80°C, which were thawed and re-frozen as needed up to a maximum of 5 times. To prepare for siRNA transfection, cells were seeded at an appropriate density for the type of downstream experiment as described in Table 3-2. To enable attachment to the growth vessels, cells were incubated for 24 hours (h) at 37°C prior to transient lipid-mediated transfection with RNAiMAX transfection reagent (Invitrogen). The volumes of transfection reagents employed for gene silencing were adjusted according to the vessel format and cell seeding density, as listed in Table 3-2. Each siRNA was diluted in the appropriate volume of serum-free medium, and RNAiMAX was diluted separately in serum-free medium. The siRNA and RNAiMAX solutions were mixed in a 1:1 ratio, inverted gently and incubated at RT for 20 min. Transfection mixtures were dispensed into wells containing complete medium, and plates were rocked gently and returned to the incubator.

Table 3-2. Pipetting Volumes Employed for siRNA Transfection.

Type of Experiment	Vessel Format	Cell Seeding Density	Volume siRNA in Tube 1	Volume RNAiMAX in Tube 2	Volume Medium in Well	Total Volume
Western Blots	6-well plate	70,000 cells/well	1 µL in 250 µL SFM[B]	6 µL in 250 µL SFM	2,000 µL	2,500 µL
NA/MNF[A] Analyses	96-well plate	1,000 cells/well	0.025 µL in 10 µL SFM	0.075 µL in 10 µL SFM	100 µL	120 µL
Mitotic Chromosome Spread Analyses	6-well plate	20,000 cells/well	0.29 µL in 250 µL SFM	1.71 µL in 250 µL SFM	2,000 µL	2,500 µL

[A]NA/MNF (Nuclear area/micronucleus formation)
[B]SFM (Serum-free medium)

3.3. WESTERN BLOT ANALYSES

Western blot analyses were employed to evaluate siRNA-based silencing efficiency for *SKP1* and *CUL1*, to assess changes in Cyclin E1 protein levels in response to diminished *SKP1* or *CUL1* expression, and to screen for CRISPR/Cas9-mediated gene editing events by identifying clones exhibiting diminished SKP1 protein expression.

3.3.1. Whole Cell Protein Extraction

Cells were seeded, silenced, and grown in 6-well tissue culture plates as described above (Section 3.2.3), and whole cell protein lysates were harvested 3 days (HCT116, FT194) or 4 days (FT246) post-transfection. Cell culture medium was aspirated from the plate, cells were rinsed 3× with 1× PBS at 4°C, and 200 µL of protein extraction buffer (Appendix A) was added to each well. Cells were incubated for 5 min at 4°C, following which cell remnants and protein lysates from each condition were collected in individual 1.5 mL microcentrifuge tubes. Samples were sonicated twice in 3 second pulses using a Sonifier Cell Disrupter (Branson Sonic Power Co.) with a duty cycle of 50% and an output control setting of 6. To remove insoluble cellular debris, samples were centrifuged (Biofuge Fresco; Thermo Scientific) at 16,060 × g for 2 min at 4ºC, and the supernatant containing soluble proteins was transferred into a sterile 1.5 mL microcentrifuge tube. Protein samples were stored at -20ºC.

3.3.2. Protein Quantification via Bicinchoninic Acid Assay

Protein concentrations were quantified using a Pierce Bicinchoninic Acid (BCA) Assay kit (Thermo Scientific) according to manufacturer's instructions. Briefly, Reagent A (containing BCA) and Reagent B (containing 4% cupric sulfate) were combined in a 50:1 ratio and 200 µL/well was dispensed into a 96-well plate (Corning). A set of 9 bovine serum albumin (BSA) protein standards were prepared with known concentrations ranging from 0 µg/mL to 2000 µg/mL, and

25 µL of each standard was dispensed into the plate in duplicate. Test protein samples were dispensed into the plate in triplicate (5 µL/well), along with RIPA buffer (20 µL/well). Proteins were incubated in the dark at 37°C for 1 h, and 562 nm absorbance measurements were subsequently acquired from each well using a Cytation 3 (BioTek) plate reader. A standard curve was generated from absorbance values and protein concentrations of BSA standards, and was used to determine protein concentrations of the unknown test samples. Values from the 3 readings were averaged for each sample, and multiplied by 5 to account for the dilution factor and to calculate the final protein concentrations.

3.3.3. Gel Electrophoresis and Western Blot

Protein samples were combined with RIPA buffer and 6× SDS Sample Loading Buffer (Appendix A) in the appropriate volumes to achieve equimolar amounts of protein for each condition (generally 20 µg). Proteins were denatured by incubating samples in a 95°C heating block (Eppendorf) for 12 min with orbital mixing. A 4-20% mini-Protean TGX gel (BioRad) was assembled inside a Miniprotean electrophoresis tank (BioRad) and the apparatus was filled with 1× Running Buffer (Appendix A). A 10 µL volume of Precision Plus Protein Dual Color Standards (BioRad) molecular weight ladder was dispensed into one well, and the remaining wells were each filled with 24 µL of denatured and cooled protein sample. Samples were electrophoresed at 140 V for 65 min at 4°C using a PowerPac HC (BioRad) power supply. A 0.45 µm polyvinylidene difluoride (PVDF) membrane (Millipore) was activated with methanol and rinsed 3× with Milli-Q water to prepare for protein transfer. The gel and membrane were assembled in a TransBlot Semi-Dry Transfer Cell (Bio-Rad) with 1× Transfer Buffer (Appendix A), and a constant voltage was applied (14 V) for 40 min to electrophoretically transfer proteins to the membrane. To assess protein transfer quality, PVDF membranes were stained with 5 mL of the total protein stain copper

phthalocyanine 3,4',4'',4'''-tetrasulfonic acid tetrasodium salt (CPTS) (Appendix A) for 5 min at RT. Membranes were de-stained by washing with Tris-buffered saline solution containing 0.1% Tween 20 (TBST) (Appendix A), which was followed by 1 h of blocking with 5% non-fat milk in 1× TBST (Appendix A) at RT. Primary antibodies targeting the protein of interest were diluted in 5% non-fat milk according to the dilutions listed in Table 3-3 and dispensed onto the membrane. Membranes were incubated with primary antibodies overnight at 4°C with gentle rocking. The next day, primary antibody solution was removed and blots were rinsed with 1× TBST for 3 × 10 min washes on a Belly Dancer (Stovall Life Science Inc.) set to medium speed. Secondary antibodies conjugated to horseradish peroxidase (HRP) were diluted in 5% non-fat milk (Table 3-3) and dispensed onto the membrane. Membranes were incubated with secondary antibodies for 1 h at RT with gentle rocking. Secondary antibody solution was removed and blots were rinsed with 1× TBST for 3 × 10 min washes.

Table 3-3. List of Antibodies Employed for Western Blot Analyses.

Primary Antibodies				
Antibody	**Catalogue Number**	**Dilution**	**Species**	**Source**
SKP1	ab76502	1:2000	Rabbit	Abcam
CUL1	ab75812	1:1000	Rabbit	Abcam
CCNE1	ab33911	1:1000	Rabbit	Abcam
a-Tubulin	ab7291	1:20,000	Mouse	Abcam
Cyclophilin B	ab16045	1:50,000	Rabbit	Abcam
Secondary Antibodies				
Goat α Rabbit HRP[A]	111-035-144	1:15,000	Goat	Jackson ImmunoResearch
Goat α Mouse HRP	115-035-146	1:10,000	Goat	Jackson ImmunoResearch

[A]HRP (Horseradish peroxidase)

3.3.4. Semi-Quantitative Immunoblot Analysis

To visualize the labeled proteins of interest, SuperSignal West Dura Extended Duration Substrate (Thermo Scientific) was utilized as described by the manufacturer. Briefly, the Stable Peroxide Solution and the Luminol/Enhancer Solution were combined in a 1:1 ratio, and ~750 µL of the visualization solution was dispensed onto the membrane and incubated in the dark for 5 min at RT. Excess visualization solution was removed and the membrane was placed into a clear sheet protector. A MyECL imager (Thermo Scientific) was employed to visualize proteins of interest via standard chemiluminescence. Images were acquired using exposure times adjusted to produce a strong signal without pixel saturation. Images were imported into FIJI software to perform semi-quantitative analysis of protein expression levels. Band intensities were first normalized to loading controls (α-Tubulin or Cyclophilin B) and were subsequently normalized to a control sample (*e.g.* non-targeting siRNA) to enable comparisons of protein expression levels between samples. Figures were assembled in Photoshop CS6 (Adobe).

3.4. CIN ASSAYS

Single-cell quantitative imaging microscopy approaches were employed to evaluate CIN-associated phenotypes in *SKP1*- and *CUL1*-silenced cells including changes in NAs and MNF. These analyses were validated using standard cytogenetic approaches to enumerate chromosomes within mitotic chromosome spreads.

3.4.1. Nuclear Area Assay

Cells were seeded into 96-well plates and silenced as described above (Section 3.2.3). At 4 days (HCT116, FT194) or 6 days (FT246) post-transfection, medium was aspirated from plates and cells were fixed for 10 min with 4% paraformaldehyde (Appendix A). Cells were washed

twice with 1× PBS, and nuclei were counterstained by adding 200 µL of 300 ng/mL Hoechst 33342 in 1× PBS (Appendix A) to each well. Plates were stored in the dark at 4°C for a minimum of 24 h prior to imaging to allow the Hoechst to equilibrate across all nuclei. A 3×3 matrix of non-overlapping 2D images (*i.e.* 9 images total) were acquired from each well using a Cytation 3 Cell Imaging Multi-Mode Reader (BioTek) equipped with a 16-bit, gray scale, charge-coupled device camera (Sony) and an Olympus 20× lens (0.45 numerical aperture). All image acquisition and analysis settings were adjusted using Gen5 Software (BioTek). Representative images were exported into Photoshop where figure panels were assembled. To determine NAs, the primary mask function of Gen5 software was employed to automatically detect interphase Hoechst-labeled nuclei above a minimum signal intensity threshold, which was optimized for each experiment and held constant between all experimental conditions. Inclusion filters were employed to detect objects of a pre-defined diameter (10 µm ≤ x ≥ 100 µm), while an edge exclusion filter was employed to remove partial nuclei located along the image periphery. NAs were automatically calculated and data were exported into Prism v6 (GraphPad), where descriptive statistics and two sample Kolmogorov-Smirnov (K-S) tests (detailed in below in Section 3.10.2.) were performed. Data were graphed using either box-and-whisker plots or a cumulative frequency distribution curves, with figure panels assembled in Photoshop.

3.4.2. Micronucleus Formation Assay

MNF assays were prepared in an identical fashion to NA assays (Section 3.4.1), including cell seeding, silencing, fixation, labeling, and imaging. Gen5 Image Prime and Gen5 Spot Counting image analysis software were employed for automated detection of micronuclei, which were operationally defined as small (< 1/3 the size of the nucleus), extra-nuclear, Hoechst-stained bodies exhibiting no visible attachments with the primary nucleus. A primary mask was applied in

Gen5 to detect primary interphase nuclei as described above (Section 3.4.1), and a secondary mask was applied with a defined ring width (15 μm) to roughly approximate the cell body boundary. The Gen5 Spot Detection option was employed to identify micronuclei (*i.e.* spots) located outside the primary nucleus, but within the cell boundary (Fig. 3-1). A size inclusion filter was also applied to identify micronuclei between 1 μm and 6 μm in diameter. Using the Subpopulation Analysis feature of Gen5, an exclusion filter was applied to restrict analysis to objects exhibiting mean Hoechst signal intensity below a maximum threshold (optimized for each experiment) to exclude brightly stained objects like apoptotic bodies and mitotic chromosomes. Finally, an edge exclusion filter (< 30 μm) was applied to compensate for partial nuclei along the edges of images from being considered micronuclei. The total number of micronuclei in each well was determined and normalized to the total number of nuclei; wells containing fewer than 40 nuclei were excluded from the analyses. MNF data were imported into Prism where descriptive statistics and Mann-Whitney (M-W) statistical tests (detailed below in Section 3.10.1) were performed and data were represented graphically as dot plots, with figure panels being assembled in Photoshop.

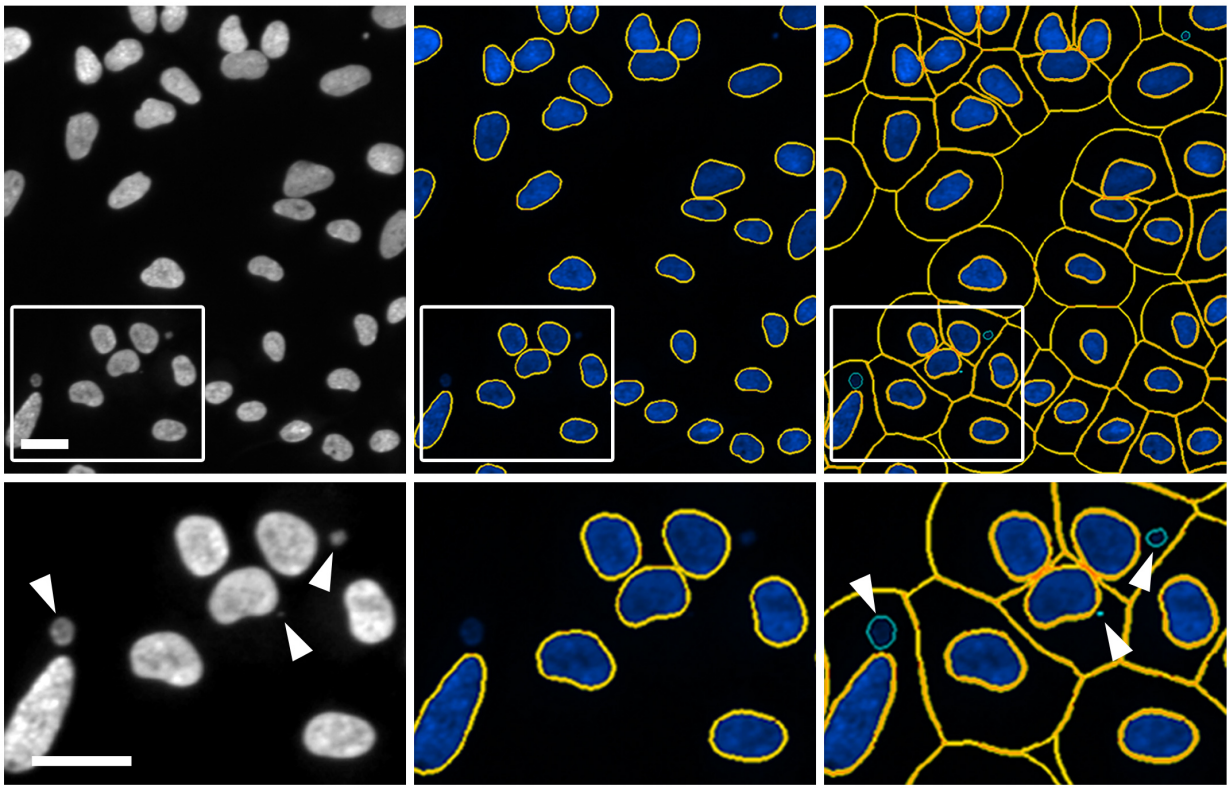

Figure 3-1. Detection of Micronuclei Using Gen5 Image Analysis Software.
Representative images depicting the software-based (Gen5) approaches used to detect MNF in Hoechst-labeled FT246 cells. A primary mask detects nuclei (middle panels), and a secondary mask approximates the cell boundary (right panels). Primary and secondary masks are shown in yellow. White arrows identify micronuclei (green boundaries), which are detected as spots within the secondary mask (right panels). Scale bar represents 30 μm.

3.4.3. Mitotic Chromosome Spreads and Chromosome Enumeration

To generate mitotic chromosome spreads, asynchronous cells were cultured and transfected on ethanol-sterilized coverslips in 6-well tissue culture plates and allowed to grow over 4 (FT194) or 6 (FT246) days as described above. Cells were subsequently treated with KaryoMAX colcemid (Gibco) at a dilution of 100 ng/mL (Appendix A) in complete medium to enrich for mitotic cells. Following a 2.5 h (FT194) or 3.5 h (FT246) incubation at 37°C, the colcemid-containing medium was removed and 2 mL of 75 mM KCl hypotonic solution (Appendix A) was added to each well for 10 min. Cells were fixed with a 3:1 mixture of methanol:acetic acid (Appendix A) in three 10 min intervals. Fixative was removed and coverslips were placed on their side to air dry. Coverslips were mounted with 10 µL of DAPI Mounting Medium (Appendix A) onto glass slides, which were stored in the dark at 4 °C for at least 24 h prior to imaging. A minimum of 100 mitotic chromosome spreads per condition were imaged using an AxioImager Z1 microscope equipped with a 63× (1.4 numerical aperture) oil-immersion, plan apochromat lens and a Zeiss HRm charge-coupled device (CCD) camera. Image files (16-bit TIFFs) were imported into FIJI software for manual chromosome enumeration and phenotypic assessment. Chromosome spreads that deviated from the modal karyotype for the cell line being employed (Table 3-1) were classified as aberrant, including small-scale numerical changes (< 10 chromosomes gained or lost) or large-scale numerical changes (≥ 10 chromosomes gained or lost). Mitotic chromosome spread analyses were performed twice per condition (N = 2) for each cell line. Graphs were generated in Prism and figures were assembled in Photoshop.

3.5. CRISPR/CAS9

CRISPR/Cas9 was employed to generate *SKP1* heterozygous knockout (*SKP1*$^{+/-}$) FT246 cells using a two-step approach. First, plasmids containing synthetic guide RNA (sgRNA) and blue fluorescent protein (tagBFP) expression cassettes (Sigma; Fig. 3-2 A; Table 3-4) were packaged into lentiviral particles (Section 3.5.2) and delivered to FT246 cells via lentiviral transduction (Section 3.5.3). One of two distinct *SKP1*-targeting sgRNAs or a non-targeting control sgRNA was employed, and fluorescence-activated cell sorting (FACS) was performed to isolate successfully transduced (BFP positive) cells (Section 3.5.5). Second, plasmids containing Cas9 and green fluorescent protein (GFP) expression cassettes (Sigma; Fig. 3-2 B) were delivered via lipid-based transfection (Section 3.5.4), and FACS was performed to isolate successfully transfected (GFP positive) cells (Section 3.5.5). This approach combines constitutive sgRNA expression with transient Cas9 expression to maximize the likelihood of an editing event, while minimizing off-target endonuclease activity associated with constitutive Cas9 (nuclease) expression.

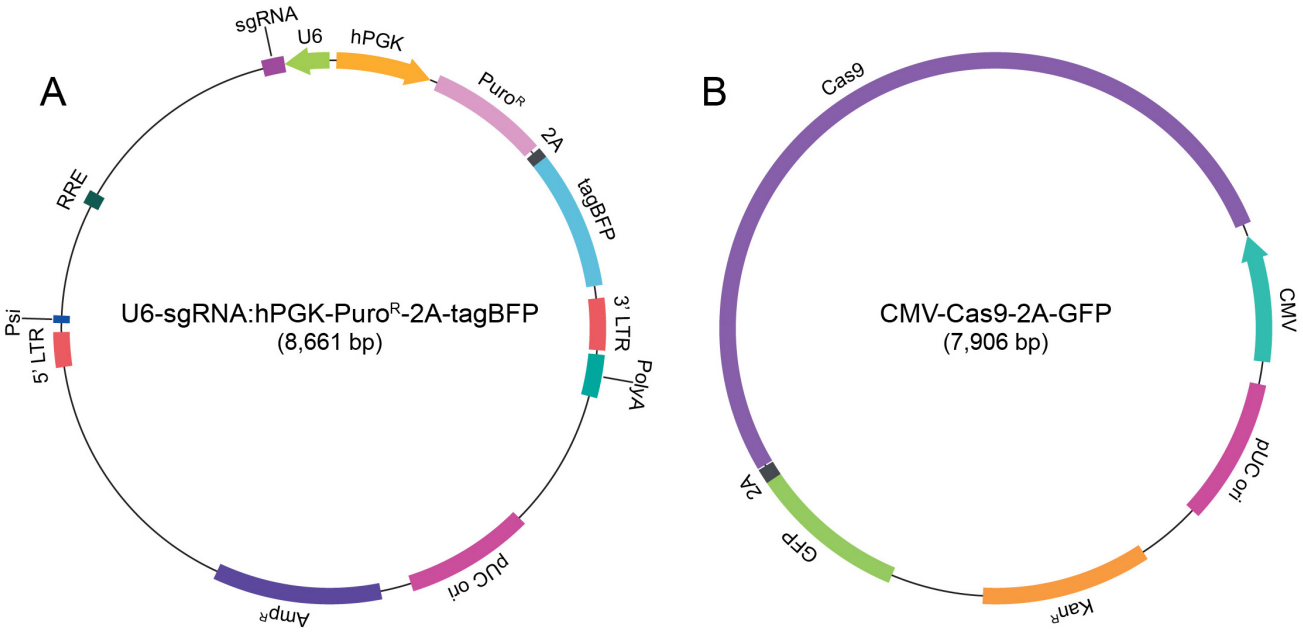

Figure 3-2. Plasmids Employed for Expression of CRISPR/Cas9 Components.
(**A**) A lentiviral transfer plasmid was employed for stable expression of a *SKP1*-targeting or non-targeting sgRNA under the control of a constitutive U6 promoter. The vector map identifies the components necessary for plasmid replication (pUC origin of replication [ori]), bacterial selection (ampicillin resistance [Amp^R]), lentiviral packaging (Psi sequence and Rev Response Element [RRE]), genomic integration within transduced cells (5' and 3' long terminal repeats [LTRs]), and isolation of successfully transduced mammalian cells including human phosphoglycerate kinase (hPGK) promoter driving constitutive bicistronic expression of a puromycin resistance gene (Puro^R) and blue fluorescent protein (tagBFP) separated by a 2A "self-cleaving" element. (**B**) A non-lentiviral plasmid was employed for transient Cas9 expression, under the control of a cytomegalovirus (CMV) promoter that was introduced into target cells via lipid-mediated transfection. The vector map identifies components necessary for plasmid replication (pUC ori), bacterial selection (kanamycin resistance [Kan^R]) and isolation of successfully transfected mammalian cells (green fluorescent protein [GFP] expression).

Table 3-4. sgRNA Sequences and *SKP1* Target Sites.

sgRNA	Sequence[A]	Target Site
sg*SKP1*-1	5’ GAGGAGGAGGGUCAUCCUUG 3’	*SKP1* Exon 3
sg*SKP1*-2	5’ UUCUCAUCAUCUUCAGGAGG 3’	*SKP1* Exon 3

[A]Each sgRNA is composed of a variable 20 nt sequence at its 3’ end (shown above) which is complementary to a region within *SKP1*, and a constant 82 nt sequence at its 5’ end that enables ribonucleoprotein complex formation with the Cas9 endonuclease. The constant sequence for both sgRNAs is: 5’ UUUUUUCGUGGCUGAGCCACGGUGAAAAAGUUCAACUAUUGCCUGA UCGGAAUAAAAUUGAACGAUAAAGAUCGAGAUUUUG 3’.

3.5.1. *Escherichia Coli* Transformation and Plasmid Preparation

To amplify sgRNA or Cas9 expression plasmids, Stellar Competent *Escherichia coli* cells (Clontech) were transformed with appropriate plasmids as per manufacturer protocol. Briefly, 50 µL of *E. coli* cells were combined with ~5 ng of plasmid stock in a 1.5 mL tube. Tubes containing the chemically competent *E. coli* were placed on ice for 30 min, heat shocked in a water bath at 42°C for 60 sec, and returned to ice for another 2 min. Super Optimal broth with Catabolite repression (SOC) medium (Takaro Bio) warmed to 37°C was added to competent cell mixture to a final volume to 500 µL. Samples were incubated for 1 h at 37°C with moderate agitation. A 1/100 dilution and a 1/10 dilution of transformation reaction in SOC medium was prepared, and 100 µL of each dilution was plated onto separate Luria-Bertani (LB) agar petri dishes containing 60 µg/mL carbenicillin (sgRNA plasmids) or 50 µg/mL kanamycin (Cas9 plasmid) (Appendix A). Plates were incubated overnight in a 37°C bacterial incubator. The following day, a well-isolated colony was selected and used to inoculate 15 mL of LB broth solution containing 60 µg/mL carbenicillin (sgRNA plasmids) or 50 µg/mL kanamycin (Cas9 plasmid) (Appendix A). Broth cultures were grown overnight at 37°C with moderate agitation. Plasmids were subsequently isolated and purified using the QIAprep Spin Miniprep kit according to the manufacturer protocol (Qiagen). DNA concentrations and purities were determined using a Nano-Drop spectrophotometer (Thermo Scientific). To prepare for lentiviral packaging, purified sgRNA expression plasmids were concentrated to 1 µg/µL using a centrifugal evaporator, and all plasmid samples were stored at -20°C.

3.5.2. Production of Lentiviral Particles

Concentrated sgRNA expression plasmids were packaged into lentiviral particles using a Lenti-X HTX Packaging System (Clontech) as per manufacturer protocol. Briefly, 4.5×10^6

Lenti-X HEK 293T lentiviral packaging cells were seeded into 10 cm collagen-coated tissue culture plates (Corning) with DMEM high glucose medium containing 10% tetracycline-free FBS (Appendix A), and grown in a 37°C humidified incubator containing 5% CO_2. Plasmids were complexed with Lenti-X HTX packaging components and transfected into Lenti-X HEK 293T cells 24 h post-seeding. Cells were incubated in a lentiviral-specific incubator for 4 h, after which medium was replaced, and cells were incubated for an additional 48 h. To test for the presence of lentivirus, 20 μL of packaging cell supernatant was applied to a Lenti-X GoStix strip (Clontech), which produces a positive signal (band) when virus production is within a usable range for transduction (> 5 x 10^5 infectious units/mL). Exact lentiviral titers were not determined. After obtaining a positive GoStix result, the remaining supernatant was collected, passed through a low protein binding 0.2 μm filter, and cooled to 4°C. Clarified supernatant was combined in a 3:1 ratio with Lenti-X concentrator (Clontech) and incubated at 4°C overnight. Samples were centrifuged at 1,500 × g for 45 minutes 4°C to obtain a lentiviral pellet, which was resuspended in 1 mL sterile 1× PBS at 4°C and stored at -80°C.

3.5.3. Lentiviral Transduction

Lentiviral transduction was employed to deliver *SKP1*-targeting or control sgRNA expression plasmids to FT246 cells. Cells were seeded into a 24-well cell culture plate (50,000 cells per well × 1 well per condition) and allowed to attach for 24 h, following which wells were washed once with 1× PBS. In a lentiviral-specific biological safety cabinet, virus stock was diluted in a 1:2 ratio with serum-free medium and 200 μL of diluted virus mixture was added to each well containing cells. For dual transduction experiments (*i.e.* simultaneous transduction with two distinct viruses), an equivalent volume of each virus stock was added to serum-free medium for an individual virus-to-medium ratio of 1:4 and a total virus-to-medium ratio of 1:2. Cells were

incubated for 4 h in a lentiviral-specific incubator at 37°C, following which wells were topped up to 500 µL with complete medium and incubated overnight. After ~24 h, lentivirus-containing medium was removed from each well and safely discarded, wells were washed 3 times with 1× PBS, and 500 µL of fresh complete medium was added. Cells were expanded by growing to confluency, passaging confluent wells, and seeding back into a larger vessel format until a sufficient number of cells (a minimum of ~2 million cells per condition or 2 confluent wells of a 6-well plate) was obtained for FACS (Section 3.5.5).

3.5.4. Lipid-Mediated Transfection for Cas9 Plasmid Delivery

Cas9 expression plasmids were delivered to a bulk population of tagBFP-positive FT246 cells via lipid-mediated transfection with Effectene reagent (Qiagen). Transfection was performed as per manufacturer protocol. Briefly, cells were grown to ~80% confluency in a 10 cm tissue culture plate, at which time cell culture medium was aspirated and replaced with 7 mL of fresh complete medium. To prepare transfection reagent, 2 µg of Cas9 plasmid DNA was combined in a tube with 300 µL of Buffer EC and 16 µL of Enhancer reagent. The mixture was incubated for 5 min at RT, following which 60 µL of Effectene transfection reagent was added, and the mixture was incubated for an additional 10 min. The transfection mixture was topped up with 3 mL of complete medium, mixed gently, and the full reaction volume was dispensed into one plate of cells. Plates were incubated for 10 h at 37°C, at which time medium was replaced with fresh complete medium, and plates were returned to the incubator. Cells were prepared for FACS at ~24 h post-transfection.

3.5.5. Fluorescence-Activated Cell Sorting

FACS was employed to isolate FT246 cells expressing fluorescent markers (tagBFP and GFP) which suggest successful delivery of CRISPR/Cas9 components. All FACS was performed

by Monroe Chan in the Regenerative Medicine Flow Cytometry facility at the University of Manitoba. Sorting was performed in two steps: 1) following lentiviral transduction with sgRNA expression plasmids, FACS was employed to isolate tagBFP-positive cells, and 2) following lipid-mediated transfection with a Cas9 expression plasmid, FACS was employed to isolate tagBFP-positive and GFP-positive cells. Untransduced (*i.e.* tagBFP-negative and GFP-negative) or untransfected (*i.e.* tagBFP-positive and GFP-negative) FT246 cells were used as controls to establish gating parameters for the detection of tagBFP or GFP, respectively. To prepare samples for sorting, cell counts were performed as detailed above (Section 3.2.2), and the resulting cell suspension was centrifuged a second time to wash the cell pellet. Supernatant was removed by aspiration, and cells were resuspended in sort buffer (Appendix A) to achieve a final cell density of ~10 million cells per mL. Propidium iodide (PI) was added to the sort buffer of test samples to distinguish between viable (PI-negative) and nonviable (PI-positive) cells, while control samples without PI were used to adjust gating parameters. Samples were transported to the FACS facility on ice, and all PI-negative cells expressing the appropriate fluorescent marker(s) (GFP and/or tagBFP) were collected as a bulk population in complete medium containing 1× penicillin-streptomycin (Gibco). The total number of cells collected was recorded. Samples were transferred to 5 mL conical tubes and centrifuged at 140 × g for 5 min. Cells were resuspended in ~100 μL of 1× PBS and plated in an appropriate vessel (containing complete medium) based on the number of cells collected (*i.e.* a single well of a 24-well plate for < 40,000 cells, or a single well of a 6-well plate for ≥ 40,000 cells). Cells were expanded by growing to confluency, passaging confluent wells, and re-seeding into a larger vessel.

3.5.6. Clonal Expansion and Screening for *SKP1* Gene Edits

To isolate individual CRISPR-edited clones from the dual-sorted tagBFP-positive and GFP-positive bulk population, cells were seeded into a 96-well plate at an average density of 0.5 cells per well (*i.e.* 1 cell for every 2 wells on average) in order to minimize wells containing multiple cells. Plates were monitored regularly over the course of several weeks to identify wells containing exactly 1 colony (*i.e.* clonal populations generated from a single cell). As single colony-containing wells reached confluency (~1 month after seeding into the 96-well plate), clones were expanded and separated into multiple vessels for multiple downstream analyses. For each clone, protein was extracted from a single well of a 24-well plate and Western blots were performed to evaluate SKP1 protein levels as detailed in Section 3.3. Clones exhibiting diminished SKP1 expression relative to a non-targeting control clone were selected for further DNA sequencing analyses.

3.5.7. Genomic DNA Extraction

Whole genomic DNA was extracted from all suspected *SKP1* heterozygous knockout clones using a DNeasy Blood & Tissue Kit (Qiagen). Briefly, cells from a confluent 10 cm tissue culture plate were treated with trypsin and centrifuged as described above (Section 3.2.1). Supernatant was discarded and the cell pellet was resuspended in 200 µL of 1× PBS. Cells were treated with 20 µL proteinase K (Qiagen) and 40 µL RNase A (Appendix A). Samples were subsequently treated as per the DNeasy Blood & Tissue Kit manufacturer protocol, and DNA was eluted in 200 µL molecular biology grade water (HyClone). DNA concentrations and purities were determined using a Nano-Drop spectrophotometer (Thermo Scientific), and all samples were stored at -20°C.

3.5.8. Polymerase Chain Reaction

Polymerase chain reaction (PCR) was employed to amplify the CRISPR/Cas9-targeted region within exon 3 of the *SKP1* locus for downstream sequencing and cloning applications. PCR primers were designed to flank *SKP1* exon 3 and position the Cas9 cut site near the centre of the 791 base-pair (bp) amplicon. This primer design enables reliable sequencing of the edit site in both the forward and reverse direction using the same primer set (see Section 3.5.11). These primers were further modified for compatibility with downstream cloning via the addition of a 15 nt complementary sequence to the 5' end of each primer that hybridizes with the pUC19 cloning vector (see Section 3.5.10). Primer sequences are listed in Table 3-5. For applications requiring high-fidelity DNA amplification (*i.e.* DNA subcloning and sequencing), Q5 High-Fidelity DNA Polymerase (New England BioLabs) was employed. For all other applications (*i.e.* colony PCR), Taq DNA Polymerase (Thermo Scientific) was employed. PCR reactions were prepared according to manufacturer protocols for the DNA polymerase being used. Briefly, nuclease-free water (HyClone), Q5 or Taq reaction buffer, dNTPs (Thermo Scientific), forward and reverse primers (Sigma), and Q5 or Taq polymerase were combined to achieve the final concentrations listed in Table 3-6 or Table 3-7, respectively, and PCR mixture was dispensed into PCR strip tubes. For Q5 reactions, 100 ng genomic DNA template (~1 μL) was added to each tube. For Taq reactions, *E. coli* colonies were mixed directly into PCR tubes (see Section 3.5.10). Tubes were transferred to a PCR thermocycler (BioRad), and thermocycling was performed using the conditions listed in Table 3-8 (Q5) or Table 3-9 (Taq). PCR products were stored at 4°C.

Table 3-5. Primers Employed for Polymerase Chain Reaction and DNA Sequencing.

Primer	Sequence[A]	T_m[B]
Forward	5’ CGGTACCCGGGGATCTGGATTAGCTTTCAAAGGGGT 3’	64°C
Reverse	5’ CGACTCTAGAGGATCTCAGTGTCAATGAAGTTAGCAAAT 3’	62°C

[A]Primers are composed of a 5’ sequence complementary to a PUC19 cloning plasmid (red text) and a 3’ sequence complementary to *SKP1* (black text).
[B]Primer melting temperatures are calculated from the 3’ *SKP1*-targeting region only.

Table 3-6. Pipetting Volumes Employed for Q5 High-Fidelity Polymerase Chain Reaction.

Component	Volume per 50 µL Reaction	Final Concentration
5× Q5 Reaction Buffer	10 µL	1×
10 mM dNTPs	1 µL	200 µM
10 µM Forward Primer	2.5 µL	0.5 µM
10 µM Reverse Primer	2.5 µL	0.5 µM
2 U/µL Q5 High-Fidelity DNA Polymerase	0.5 µL	0.02 U/µL
Template DNA	100 ng	5 ng/µL
Nuclease-Free Water	to 50 µL	

Table 3-7. Pipetting Volumes Employed for Taq Polymerase Chain Reaction.

Component	Volume per 50 µL Reaction	Final Concentration
10× Taq Buffer	5 µL	1×
10 mM dNTPs	1 µL	200 µM
10 µM Forward Primer	2.5 µL	0.5 µM
10 µM Reverse Primer	2.5 µL	0.5 µM
5 U/µL Hot-Start Taq DNA Polymerase	0.25 µL	0.025 U/µL
Nuclease-Free Water	to 50 µL	

Table 3-8. Thermocycling Conditions for Q5 High-Fidelity Polymerase Chain Reaction.

Step	Temperature	Time	Number of Cycles
Initial Denaturation	98°C	30 sec	1
Denaturation	98°C	10 sec	30
Annealing	63°C	30 sec	
Extension	72°C	30 sec	
Final Extension	72°C	2 min	1
Hold	10°C		

Table 3-9. Thermocycling Conditions for Taq Polymerase Chain Reaction.

Step	Temperature	Time	Number of Cycles
Initial Denaturation	95°C	3 min	1
Denaturation	95°C	30 sec	30
Annealing	48.3°C	30 sec	
Extension	72°C	1 min	
Final Extension	72°C	10 min	1
Hold	10°C		

3.5.9. Agarose Gel Electrophoresis

Agarose gel electrophoresis was employed to visualize PCR products and confirm specific amplification of the *SKP1* exon 3 (791 bp) DNA fragment. To prepare a 1.0% agarose gel, 0.5 g agarose (Invitrogen) was combined with 50 mL of 1× Tris-acetate-EDTA (TAE) buffer (Appendix A) and heated until agarose was fully dissolved. Agarose was allowed to cool slightly, and 5 µL of SYBR Safe DNA Gel Stain (Thermo Scientific) was added. Agarose solution was mixed, poured into a cast, and allowed to solidify. The agarose gel was transferred to an electrophoresis tank filled with 1× TAE buffer, and DNA ladder was loaded into one well (5 µL of O'GeneRuler 1 kb Plus DNA Ladder [Thermo Scientific]). DNA samples were mixed in a 6:1 ratio with 6× DNA loading dye (Thermo Scientific) and 5 µL was loaded into each remaining well of the agarose gel. The gel was electrophoresed for ~30 min at 100 V and visualized under ultraviolet light in a MyECL imager (Thermo Scientific).

3.5.10. DNA Subcloning

To isolate and characterize individual *SKP1* alleles, DNA subcloning was performed using Q5-amplified DNA and an In-Fusion Cloning Kit (Takara Bio). PCR products were prepared for cloning via spin column purification (QIAquick PCR Purification Kit [Qiagen]). In-Fusion cloning reactions were set up by combining 4 µL of In-Fusion Enzyme Premix with 50 ng of pUC19 linearized cloning vector and 50 ng of purified PCR product. Reactions were topped up to 20 µL with molecular biology grade water (HyClone). Samples were incubated for 15 min at 50°C, and transferred to ice. To amplify vectors containing successfully cloned inserts, 2.5 µL of In-Fusion reaction mixture was used to transform 50 µL of Stellar Competent *E. Coli* cells as detailed in Section 3.5.1. The transformation mixture was plated on LB agar plates containing 60 µg/mL carbenicillin, and plates were incubated overnight in a 37°C bacterial incubator. To screen for

E. coli cells containing the amplified *SKP1* allele, a minimum of 10 well-isolated individual colonies were selected for colony PCR (Section 3.5.8), and the resulting PCR products were electrophoresed on a 1.0% agarose gel (see Section 3.5.9). Colonies that produced a single PCR product of the expected size (791 bp) were used to inoculate 15 mL of LB broth containing 60 µg/mL carbenicillin. Broth cultures were grown overnight at 37°C with moderate agitation. Plasmids were subsequently isolated and purified using a QIAprep Spin Miniprep kit according to the manufacturer protocol (Qiagen), and eluted in molecular biology grade water (HyClone).

3.5.11. DNA Sequencing and Sequence Analyses

DNA sequencing was employed to characterize the CRISPR/Cas9-mediated gene edits in suspected *SKP1*$^{+/-}$ FT246 cells. All DNA sequencing was performed using the Sanger Sequencing service offered by McGill University and Génome Québec Innovation Centre (Montreal, Canada), and samples were prepared according to facility sample submission guidelines. Two DNA sequencing steps were performed for each *SKP1*$^{+/-}$ clone. First, unpurified PCR products (*i.e.* prior to subcloning and isolating the two individual alleles) were sent for preliminary sequencing to identify the clones with suspected gene editing events and predict the nature of the edits. Sequencing was performed in both the forward and reverse direction using the same primer set as described in Section 3.5.8 (also see Table 3-4). Chromatogram files were uploaded to CRISP-ID (http://crispid.gbiomed.kuleuven.be), an online tool for predicting the size and location of CRISPR-mediated insertions or deletions (indels) based on alignment to a reference sequence (*i.e.* wild-type *SKP1*). Importantly, this program is able to detect and resolve multiple alleles within a heterogeneous mixture, allowing for the identification of putative *SKP1*$^{+/-}$ clones. To confirm preliminary sequencing results, alleles were subcloned (see Section 3.5.10) and a minimum of 6 purified plasmids for each clone were sent for a second round of DNA sequencing using only

the reverse primer described in Section 3.5.8. Clones were determined to be *SKP1* heterozygotes if two distinct *SKP1* alleles (*i.e.* wild-type and mutated) were detected among the 6 sequenced plasmids.

3.6. CIN TIMECOURSE

To evaluate the temporal dynamics of CIN within FT246 *SKP1*$^{+/-}$ clones, the three CIN assays described in Section 3.4. were repeated at regular time intervals over the course of ~2.5 months. Beginning with as early a passage population as possible following CRISPR/Cas9 (*i.e.* immediately following FACS and clonal expansion; denoted "passage 0" [p0]), cells were seeded into 96-well plates (4,000 cells/well × 12 wells/condition) for NA and MNF analyses, or onto sterile coverslips within 6-well plates (60,000 cells/well) for mitotic chromosome spread analyses. Cells were grown for 72 h, then CIN phenotypes were assessed as detailed in Sections 3.4.1 - 3.4.3. Cell cultures originating from the p0 sample were maintained by passaging cells approximately every 4 days, and CIN assays were repeated at every 4th passage for a total of 5 timepoints.

3.7. FLUORESCENCE IMAGING MICROSCOPY

Fluorescence imaging microscopy was employed to characterize various features of FT246 *SKP1*$^{+/-}$ clones and parental FT246 cells, including protein expression levels via indirect immunofluorescence and cell morphology via Wheat Germ Agglutinin (WGA) labeling.

3.7.1. Indirect Immunofluorescence

Indirect immunofluorescence was performed to characterize TP53 and PAX8 protein expression levels within FT246 *SKP1*$^{+/-}$ clones and parental FT246 cells. Cells were seeded onto

sterile coverslips within 6-well plates and upon reaching ~50% confluency, cells were fixed with 4% paraformaldehyde for 10 minutes and washed once with 1× PBS. Cells were permeabilized in 1× PBS containing 0.5% Triton X (Appendix A) for 10 minutes, and were subsequently washed twice with 1× PBS. Primary antibody dilutions in 1× PBS were prepared according to Table 3-10. Coverslips were placed cell side-down on top of a 30 µL aliquot of the antibody dilution and incubated for 1 h in a humidified chamber. Cells were washed once with 1× PBS containing 0.1% Triton X (Appendix A) and twice with 1× PBS. Secondary antibody dilutions in 1× PBS were prepared according to Table 3-10. Coverslips were placed on top of a 30 µL aliquot of the secondary antibody dilution and incubated for 1 h in a humidified chamber protected from the light. Additional washes in 0.1% Triton X (1×) and 1× PBS (2×) were performed and coverslips containing cells were mounted onto glass slides containing a 7.4 µL aliquot of DAPI Mounting Medium (Appendix A). Images were acquired using an AxioImager Z1 Microscope (Zeiss) equipped with an AxioCam HR CCD camera (Zeiss) and a 20× Plan-Neofluar objective lens (0.5 numerical aperture) or a 63× Plan-Apochromat oil immersion objective lens (1.40 numerical aperture). Immersol 518F immersion oil (Zeiss) with a 1.518 refractive index was utilized with the 63× oil immersion objective. 49HE DAPI and 38HE FITC filter sets (Zeiss) were employed to acquire DAPI and Alexafluor488 channels, respectively. Exposure times were optimized for each channel independently and maintained constant for all conditions to enable comparisons of protein expression levels. Images were imported into Photoshop where figure panels were assembled.

Table 3-10. List of Antibodies Employed for Indirect Immunofluorescence.

Primary Antibodies				
Antibody	**Catalogue Number**	**Dilution**	**Species**	**Source**
TP53	M7001	1:200	Mouse	Dako
PAX8	ab189249	1:200	Rabbit	Abcam
Secondary Antibodies				
Anti-Mouse AlexaFluor488	ab150117	1:200	Goat	Abcam
Anti-Rabbit AlexaFluor488	ab150081	1:200	Goat	Abcam

3.7.2. Wheat Germ Agglutinin Labeling

To visualize cell bodies of FT246 *SKP1*$^{+/-}$ clones, a WGA Alexa Fluor 488 Conjugate Labeling Kit (Thermo Scientific) was employed. Cells were grown on sterile coverslips within 6-well plates at various seeding densities and were fixed in 1.5 mL of 4% paraformaldehyde for 10 min at RT. Paraformaldehyde was removed and cells were rinsed 3× with 1.5 mL Hank's balanced salt solution (1× HBSS) for mammalian cells (Thermo Scientific). Coverslips were incubated cell-side down on parafilm containing 30 µL aliquots of 5 µg/mL WGA solution prepared from a 1 mg/mL stock (Appendix A) for 10 min at RT. When cell membrane labeling was complete, cells on coverslips were washed twice with 1× HBSS and permeabilized in ~2 mL of 0.5% Triton X for 10 min at RT, and rinsed twice with 1× PBS. Coverslips were counterstained with 7.4 µL of Mounting Medium containing DAPI, and mounted onto glass slides. Images were acquired as detailed in Section 3.7.1. and imported into Photoshop to assemble figure panels.

3.8. CELL PROLIFERATION ASSAYS

Two complementary approaches were employed to characterize growth and/or proliferation rates of various cell lines used within this thesis: Real-time Cell Analysis (RTCA) and nuclear enumeration assays.

3.8.1. Real-time Cell Analysis

The xCELLigence RTCA system (Acea Biosciences) consists of microplates lined with gold microelectrodes on their lower surface and an RTCA-dual purpose plate reader which is housed within a 37°C incubator. This system enables kinetic measurements of electrical impedance (*i.e.* cell index), which is expected to increase as cells attach to the plate and grow or proliferate. Cells were seeded in quadruplicate at a density of 1,000 cells per well into a 16-well xCELLigence

RTCA E-plate, and cell index readings were acquired every 15 minutes for ~2 weeks or until wells became confluent and growth curves reached a plateau. Data from RTCA software were exported into Prism, where a single growth curve was generated for each condition by plotting the average cell index as a function of time.

3.8.2. Nuclear Enumeration Assay

Cells were seeded into a 96-well optical-bottom tissue culture plate at a density of 500 cells/well. After 48 h, medium was aspirated from 6 of the 96 wells and replaced with 100 μL of fresh medium containing 300 ng/mL Hoechst, following which the plate was incubated for 1 h at 37°C. A 4×4 matrix of non-overlapping images was subsequently acquired from each of the Hoechst-containing wells using a Cytation3 microscope as described in Section 3.4.1. Plates were returned to the 37°C incubator, and the above steps were repeated every 48 h using 6 new wells at each timepoint until wells reached confluency (~16 days). Gen5 automated image analysis software was employed to enumerate nuclei within each image and generate well totals (*i.e.* the sum of nuclear counts from all 16 images within a given well). Nuclear enumeration data were exported to Prism, where cell proliferation curves were generated by plotting the mean of 6 replicate nuclear counts as a function of time.

3.9. SOFT AGAR COLONY FORMATION ASSAY

Soft agar colony formation assays were employed to evaluate anchorage-independent growth capacity of *SKP1*$^{+/-}$ clones. To prevent cells from adhering to the bottom of the tissue culture plate, a two-layer soft agar approach was employed. First, a support layer of 0.6% agar was prepared by mixing 2× complete medium (Appendix A) in a 1:1 ratio with sterile 1.2% agarose (Appendix A) and dispensing 2 mL of this mixture into each well of a 6-well plate. All reagents

were maintained at ~40-50°C during preparation to prevent premature solidification of agar, and cooled to RT after dispensing into the plate. Cell passaging and counting was performed as detailed above, and cells were diluted in 2× medium to achieve 50,000 cells per mL. Second, a cell-containing layer of 0.4% agar was prepared by mixing the 2× cell suspension in a 1:1 ratio with sterile 0.8% agarose (Appendix A) at 40°C, and dispensing 2 mL of this mixture into each well containing solidified bottom agar for a final seeding density of 50,000 cells per well. Plates were cooled to RT and supplemented with 2 mL of complete liquid medium. Media were replenished once per week for a total of 4 weeks, at which time cells were fixed with 4% paraformaldehyde for 20 minutes, and stained with 0.005% crystal violet solution (Appendix A) for 45 minutes. Macroscopically visible colonies were manually enumerated. To quantify microscopic colony formation, a Cytation3 microscope and 4× objective were employed to capture an 8×8 image matrix of images within each well. To capture colonies located in multiple focal planes within the layer of top agar, each 8×8 image matrix was collected as a z-stack containing 11 slices for a total of 704 images per well. Using Gen5 image analysis software, all 704 images were stitched together to generate a single image (z-projection), from which microscopically visible colonies ≥ 100 μm in diameter were enumerated.

3.10. STATISTICAL ANALYSES

The number of experimental replicates (N) and technical replicates (n) are indicated for all experiments presented in this thesis. For all experiments with $N > 1$, results from one representative experimental replicate are presented. All statistical analyses were performed using Prism v6 (GraphPad).

3.10.1. Mann-Whitney Tests

The M-W test is a non-parametric statistical test that compares the rank orders of two data sets (*i.e.* experimental vs. control), and calculates a *P*-value based on the difference in mean ranks between the two conditions. In this thesis, M-W *P*-values < 0.05 are considered statistically significant, and suggest that the two mean ranks are unlikely to be as far apart as observed based on random chance alone.

3.10.2. Kolmogorov-Smirnov Tests

The two sample K-S test is a non-parametric statistical test that compares the cumulative frequency distributions of two data sets (*i.e.* experimental vs. control), and calculates a *P*-value based on the maximum difference between the two distributions. In this thesis, K-S *P*-values < 0.05 are considered statistically significant, and suggest that the two cumulative frequency distributions are unlikely to be as far apart as observed based on random chance alone.

CHAPTER 4. RESULTS

4.1. AIM 1: TO EVALUATE THE IMPACT *SKP1* OR *CUL1* SILENCING HAS ON CYCLIN E1 LEVELS AND CIN.

Cyclin E1 overexpression is implicated in CIN[90] and HGSOC pathogenesis[50], and Cyclin E1 protein expression levels are normally regulated by the SCF complex, which includes the proteins SKP1 and CUL1. *SKP1* silencing has previously been shown to induce increases in Cyclin E1 levels and CIN phenotypes in HCT116 CRC cells (McManus laboratory, unpublished observations), but its impact in HGSOC remains unknown. Additionally, the impact diminished *CUL1* expression has on Cyclin E1 levels and CIN has never been evaluated in any context. Accordingly, *SKP1* or *CUL1* silencing was performed in both a CRC and an HGSOC cellular context and CIN phenotypes were evaluated including changes in NAs, increases in MNF, and changes in chromosome numbers.

4.1.1. Characterization of Fallopian Tube Secretory Epithelial Cell Lines.

To identify a suitable HGSOC precursor model in which to assess CIN, the karyotypes of two FT cell lines (FT194 and FT246) were assessed by spectral karyotyping (SKY; performed by Zelda Lichtensztejn) and mitotic chromosome spread analyses (see Section 4.1.5.). SKY analyses revealed FT194 cells contain 46 chromosomes, along with a three-way chromosomal rearrangement involving chromosomes 5, 14, and 20 which was recurrent across 15 spectral karyotypes assessed (Fig. 4-1). Accordingly, the karyotype for FT194 cells can be expressed as 46, XX, der(5;14;20)t(5;14;20) (cytogenetic nomenclature by Dr. Reena Ray Sisk). Enumeration of chromosomes within 100 mitotic chromosome spreads confirmed FT194 cells have a modal chromosome number of 46 (identified in ~80% of mitotic chromosome spreads).

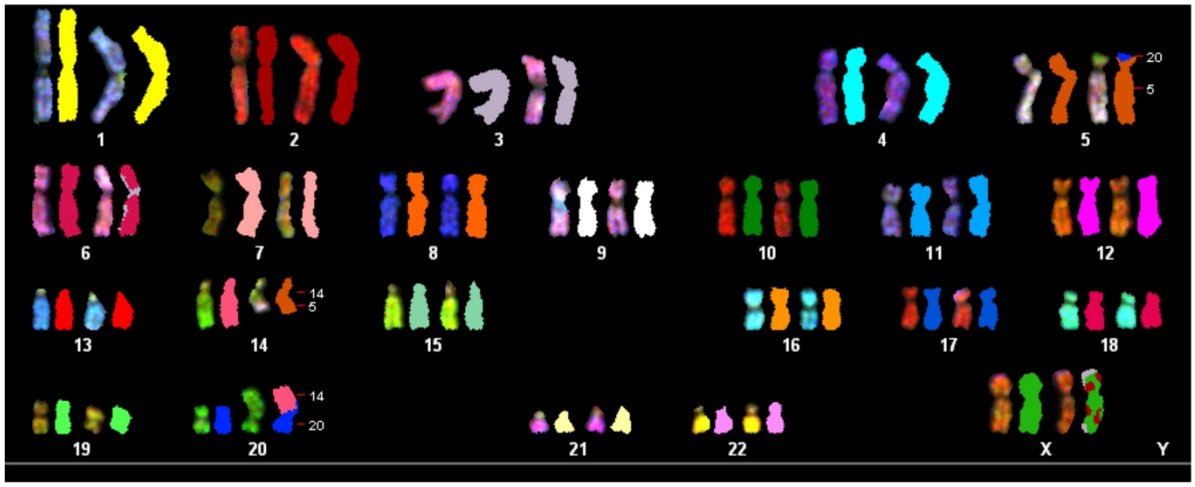

Figure 4-1. Spectral Karyotyping of FT194 Cells.
Representative spectral karyotype for FT194 cells based on 15 karyotypic analyses. FT194 cells have a modal chromosome number of 46, along with a chromosomal rearrangement involving chromosomes 5, 14, and 20. The modal FT194 karyotype can be expressed as 46, XX, der(5;14;20)t(5;14;20). Experimental execution, data analyses, and figure preparation performed by Zelda Lichtensztejn; cytogenetic nomenclature by Dr. Reena Ray Sisk.

Within the FT246 cell population, analysis of 25 spectral karyotypes revealed several characteristic chromosomal rearrangements including a derivative chromosome 7 containing a fragment from chromosome 3 (which was present in 100% of spectral karyotypes), along with additional rearrangements that are depicted in Fig. 4-2. Based on these sets of rearrangements, two predominant subclones were identified (hereafter referred to as FT246 subclones 1 and 2), which contain 46 and 44 chromosomes, respectively. FT246 subclone 1 harbors two derivative copies of chromosome 10 which each contain a translocated fragment from the long arm of the X chromosome (*i.e.* a non-reciprocol translocation). The karyotype for FT246 subclone 1 can be expressed as 46,XX,der(7)t(3;7),-10,-10,+der(10)t(10;X)×2,del(X)(q?). FT246 subclone 2 contains a distinct set of rearrangements, including monosomy for chromosomes 13 and 21, a derivative chromosome 4 containing a fragment from chromosome 1, and the presence of a marker chromosome (*i.e.* a small chromosome fragment that could not be identified by hybridization to a specific chromosomal probe set) that is expected to be composed of centromeric DNA. The karyotype for subclone 2 (including the marker chromosome in the total count) can be expressed as 45,XX,der(4)t(1;4),der(7)t(3;7),-13,-21,+mar. These specific sets of chromosomal rearrangements were found to be recurrent across 25 spectral karyotypes evaluated. Enumeration of chromosomes within 100 mitotic chromosome spreads for untreated FT246 cells revealed that ~54% of spreads contain 46 chromosomes, while ~22% of spreads contain 44 chromosomes plus the marker fragment, which most likely reflect the relative proportions of the two subclones within the overall population. Thus, despite some pre-existing variation in chromosome numbers within the parental FT246 cell line, their modal chromosome number is 46. Collectively, these data establish the baseline karyotypes of untreated FT194 and FT246 cells, which will enable the

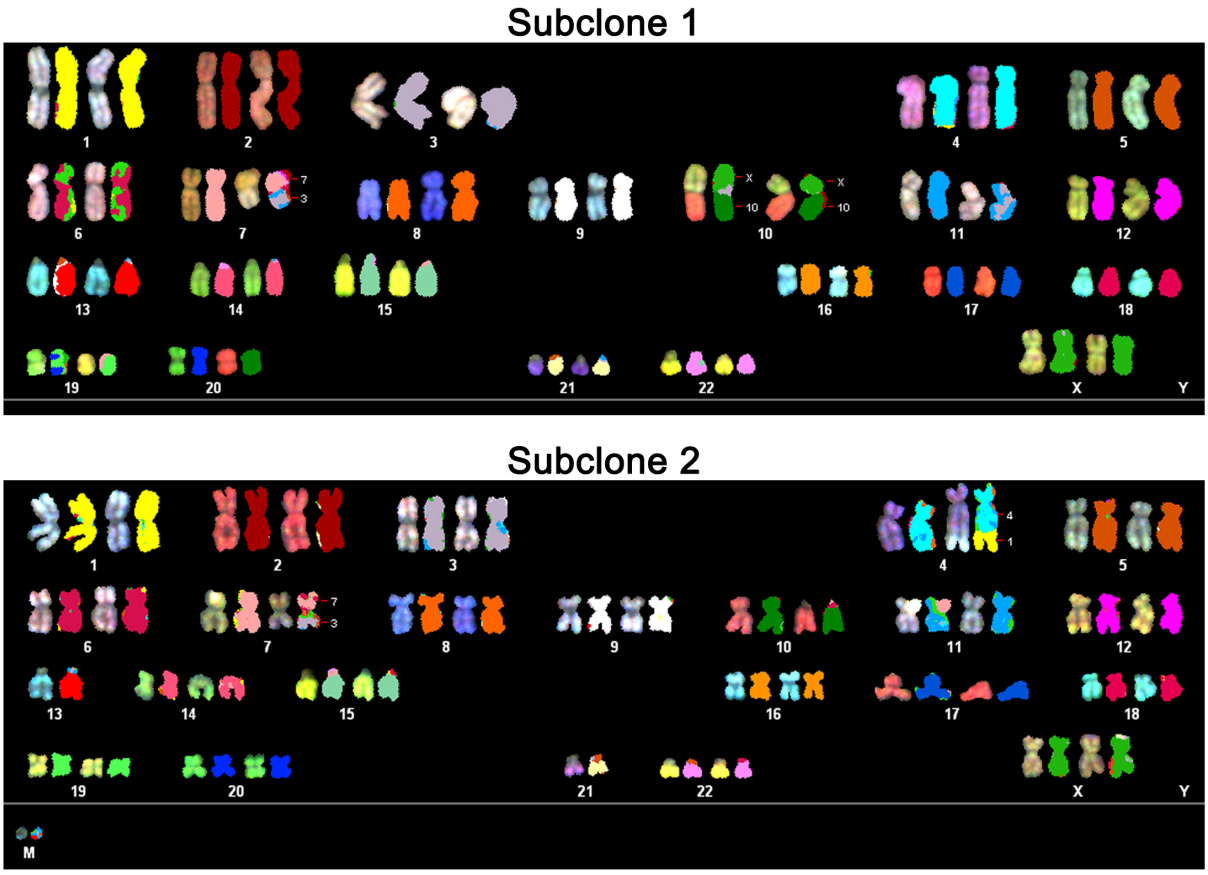

Figure 4-2. Spectral Karyotyping of FT246 Cells.
Representative spectral karyotypes for FT246 cells based on 25 karyotypic analyses. Two predominant subclones were identified within the FT246 cell line, with karyotypes of 46,XX,der(7)t(3;7),-10,-10,+der(10)t(10;X)×2,del(X)(q?) (subclone 1; top panel) and 45,XX,der(4)t(1;4),der(7)t(3;7),-13,-21,+mar (subclone 2; bottom panel). Experimental execution, data analyses, and figure preparation performed by Zelda Lichtensztejn; cytogenetic nomenclature by Dr. Reena Ray Sisk.

interpretation of downstream experiments investigating the mechanisms and pathways leading to the induction of CIN (*i.e.* deviation from these baseline karyotypes).

In addition to characterizing the karyotypes of FT194 and FT246 cells, cell proliferation rates were evaluated via RTCA to identify appropriate cell seeding densities and experimental endpoints for downstream assays. Cell index is a measurement of electrical impedance, and increases as cells attach to the plate surface and grow or proliferate. Cells were seeded into an RTCA microplate at a range of cell densities, and the change in cell index was monitored as a function of time. The resulting RTCA proliferation curves for FT194 and FT246 cells are shown in Fig. 4-3, and are characterized by an initial plateau (suggesting a lag phase prior to cell growth or proliferation) followed by a steady increase in cell index (from which the slope of the curve indicates the rate of growth/proliferation), and a final plateau (suggesting maximal confluency). For cell seeding densities of 1,000, 2,000, or 4,000 cells per well, proliferation rates for both the FT194 and FT246 cells are robust, but are preceded by a cell density-dependent lag phase. At lower cell seeding densities (500 cells per well), proliferation rates appear to be impaired, as indicated by a qualitative decrease in the slope of the curve. In addition, at a fixed cell seeding density, FT246 cells appear to have a reduced proliferation rate relative to FT194 cells and take ~1.5 times longer to reach confluency (*e.g.* at an initial density of 1,000 cells per well, FT194 and FT246 cells take ~4 and 6 days to reach a plateau, respectively). Accordingly, downstream experimental endpoints were adjusted to reflect these differences in proliferation rates for FT194 and FT246 cells.

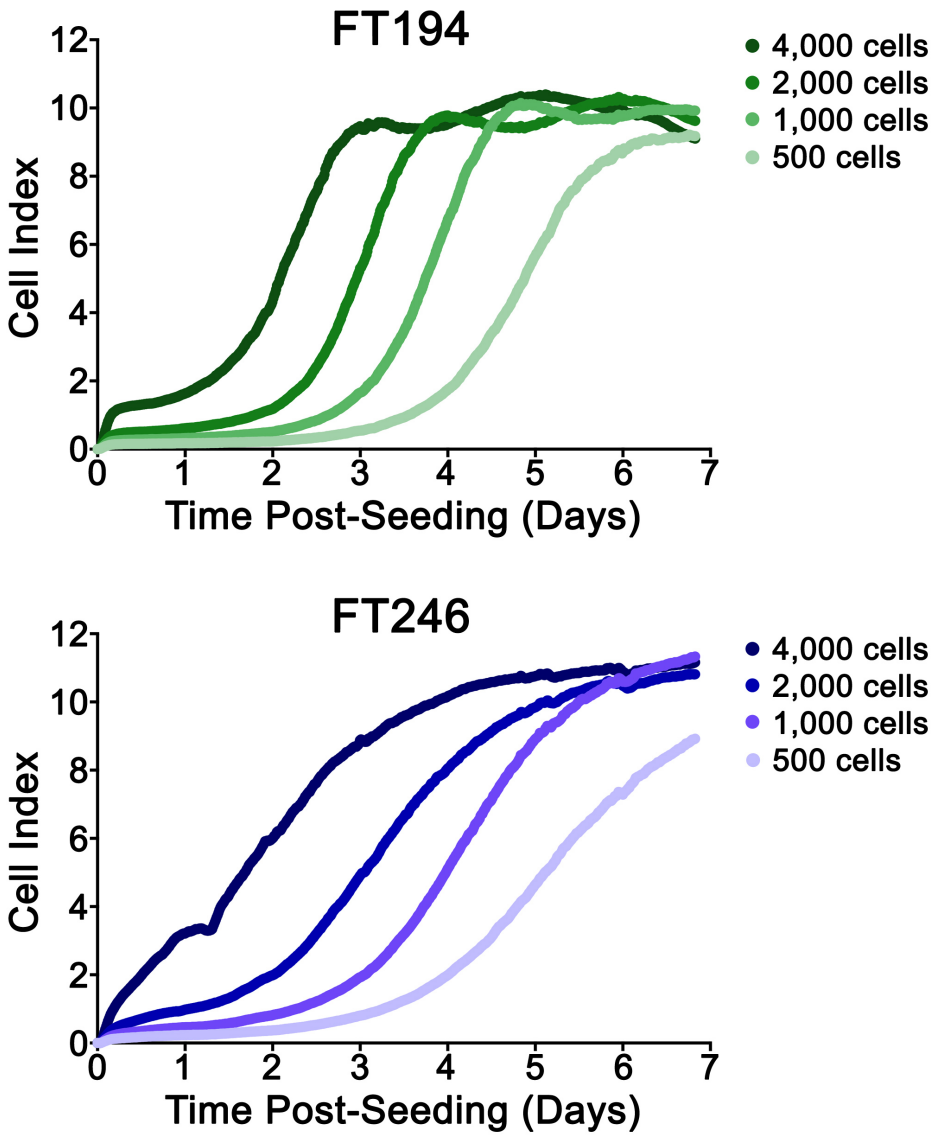

Figure 4-3. FT Cell Proliferation Curves.
RTCA proliferation curves for FT194 (top) and FT246 (bottom) cells at varying cell seeding densities. An increase in cell index is indicative of an increase in cell growth and/or proliferation. N=2; n=4.

4.1.2. *SKP1* or *CUL1* Silencing Induces Increases in Cyclin E1 Levels.

To begin to evaluate the impact diminished *SKP1* or *CUL1* expression has on Cyclin E1 levels and CIN, the silencing efficiency of four individual siRNA duplexes or a pooled siRNA (*i.e.* containing equal molar amounts of the four individual siRNA duplexes) targeting *SKP1* or *CUL1* was evaluated by semiquantitative Western blot analysis. For each gene, two of the four siRNA duplexes consistently resulted in efficient silencing ($\leq$ 10% of endogenous protein expression) across three different cell lines (HCT116, FT194, and FT246), namely si*SKP1*-1 and si*SKP1*-2 (Fig. 4-4) or si*CUL1*-3 and si*CUL1*-4 (Fig. 4-5). Accordingly, these siRNAs were employed in all downstream experiments, along with the pooled siRNA (si*SKP1*-Pool or si*CUL1*-Pool).

To evaluate the impact diminished *SKP1* or *CUL1* expression has on Cyclin E1 levels, semiquantitative analysis was performed to compare Cyclin E1 levels within the *SKP1* or *CUL1* silenced cells to corresponding non-targeting controls. In general, *SKP1* or *CUL1* silencing was associated with increases in Cyclin E1 levels within HCT116, FT194, and FT246 cell lines. The samples exhibiting the strongest *SKP1* or *CUL1* silencing efficiencies (*i.e*. the greatest decreases in SKP1 or CUL1 expression) were typically associated with the most pronounced increases in Cyclin E1 levels. HCT116, FT194, and FT246 cells silenced with si*SKP1*-Pool resulted in 9.1-, 10.1-, and 2.8-fold increases in Cyclin E1 levels, respectively (Fig. 4-4), while si*CUL1*-Pool silencing resulted in 6.0-, 2.4-, and 1.8-fold increases within the three cell lines, respectively (Fig. 4-5). Thus, diminished *SKP1* or *CUL1* expression induces increases in Cyclin E1 levels, which is predicted to underlie CIN in CRC or FT cells.

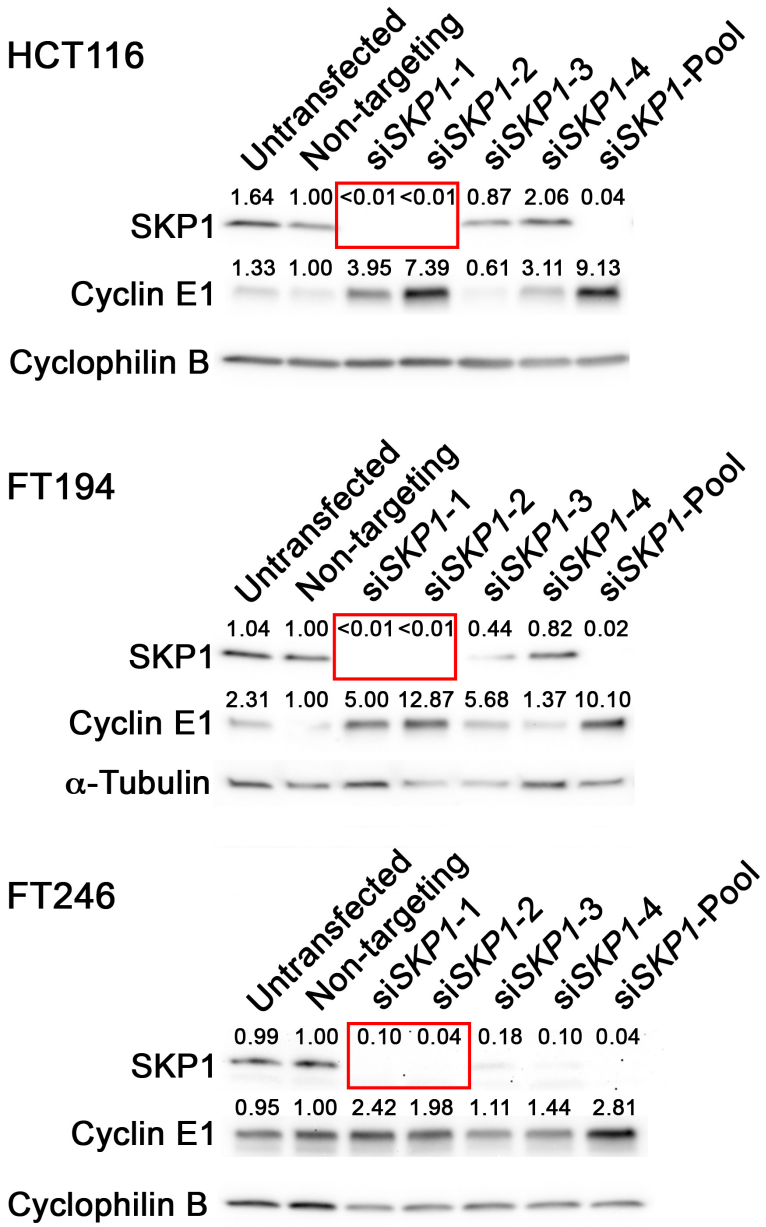

Figure 4-4. Diminished SKP1 Expression is Associated with Increased Cyclin E1 Levels. Semi-quantitative western blots depicting the *SKP1* silencing efficiency of individual (si*SKP1*-1, si*SKP1*-2, si*SKP1*-3, si*SKP1*-4) and four pooled (si*SKP1*-Pool) siRNAs within HCT116 (top), FT194 (middle), and FT246 (bottom) cell lines. Note the increases in Cyclin E1 levels within the *SKP1* silenced cell populations. Fold changes in SKP1 or Cyclin E1 expression relative to non-targeting controls are indicated, using cyclophilin B or α-tubulin as loading controls. The red bounding box identifies the individual siRNA duplexes showing greatest silencing efficiency, namely si*SKP1*-1 and si*SKP1*-2. N=3.

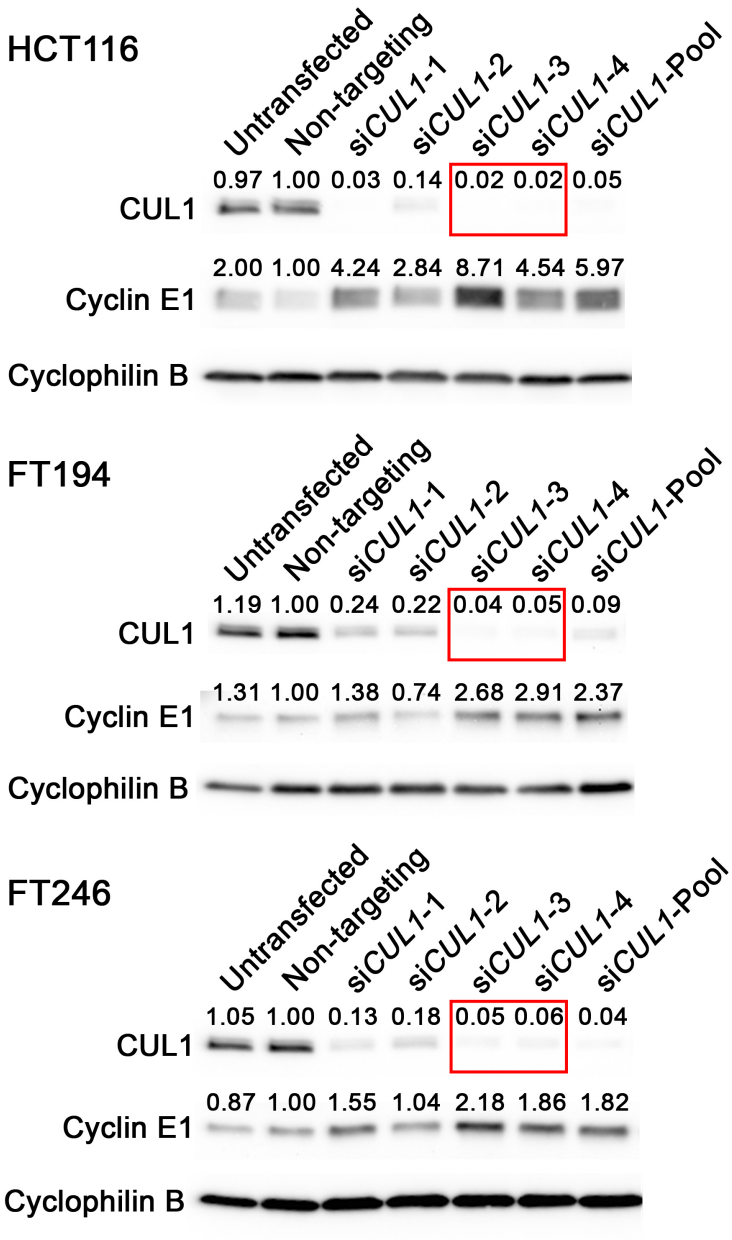

Figure 4-5. Diminished CUL1 Expression is Associated with Increased Cyclin E1 Levels. Semi-quantitative western blots depicting the *CUL1* silencing efficiency of individual (si*CUL1*-1, si*CUL1*-2, si*CUL1*-3, si*CUL1*-4) and four pooled (si*CUL1*-Pool) siRNAs within HCT116 (top), FT194 (middle), and FT246 (bottom) cell lines. Note the increases in Cyclin E1 levels within the *CUL1* silenced cell populations. Fold changes in CUL1 or Cyclin E1 expression relative to non-targeting controls are indicated, using cyclophilin B as a loading control. The red bounding box identifies the individual siRNA duplexes showing greatest silencing efficiency, namely si*CUL1*-3 and si*CUL1*-4. N=3.

4.1.3. *SKP1* or *CUL1* Silencing Induces Increases in CIN Phenotypes in HCT116 Cells.

While *SKP1* silencing has previously been shown to induce CIN within a CRC cellular context (McManus laboratory, unpublished observations), the impact reduced *CUL1* expression has on CIN has never been determined. To begin to investigate the role *CUL1* has in regulating chromosome stability and to bridge the gap between previous findings and the current HGSOC study, *SKP1* or *CUL1* silencing was performed in HCT116 CRC cells and changes in CIN-associated phenotypes (NAs or MNF) were evaluated using single-cell quantitative imaging microscopy. As shown in Fig. 4-6 A, both *SKP1* and *CUL1* silencing induced qualitative changes in NAs. In agreement with previous findings, *SKP1* silencing resulted in statistically significant changes in NA cumulative frequency distributions (Fig. 4-6 B; Table S1). The cumulative frequency distribution curves for *SKP1* silenced cells span across a broad range of NAs, which is indicative of increased cell-to-cell NA heterogeneity and CIN. Similarly, *CUL1* silencing resulted in a broadening of the curves and statistically significant changes in NA cumulative frequency distributions relative to controls (Fig. 4-6 C; Table S2). In addition, both *SKP1* and *CUL1* silencing induced statistically significant increases in MNF within HCT116 cells relative to controls (Table S3), with mean fold increases of 12.57 and 7.68 for si*SKP1*-Pool and si*CUL1*-Pool, respectively (Fig. 4-7). Interestingly, *SKP1* silencing reproducibly induced a more extreme CIN phenotype compared to *CUL1* silencing with both the NA and the MNF assay. Collectively, these data confirm previous findings showing that *SKP1* is a CIN gene in CRC cells, and further identify *CUL1* as a putative novel CIN gene in CRC.

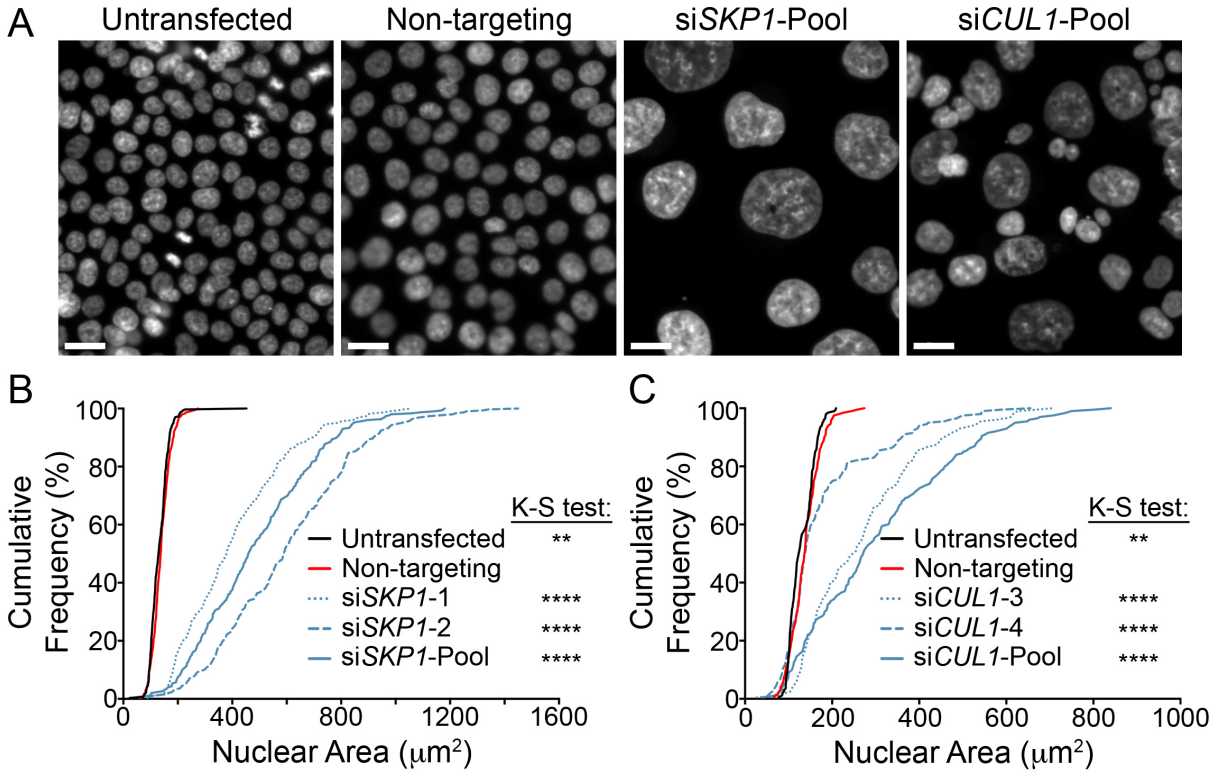

Figure 4-6. *SKP1* or *CUL1* Silencing Induces Changes in NAs in HCT116 Cells.
(A) Representative images of Hoechst-counterstained nuclei showing qualitative changes in NAs following *SKP1* or *CUL1* silencing. Scale bar represents 20 μm. **(B)** NA cumulative frequency distributions following *SKP1* silencing relative to controls. K-S tests reveal statistically significant changes (*i.e.* rightward shift) in NA cumulative frequency distributions relative to non-targeting controls. N=3; 300 nuclei analyzed/condition. **(C)** NA cumulative frequency distributions following *CUL1* silencing relative to controls. K-S tests reveal statistically significant changes (*i.e.* rightward shift) in cumulative NA frequency distributions relative to non-targeting controls. N=3; 300 nuclei analyzed/condition. Statistical significance is indicated (**, p-value < 0.01; ****, p-value < 0.0001).

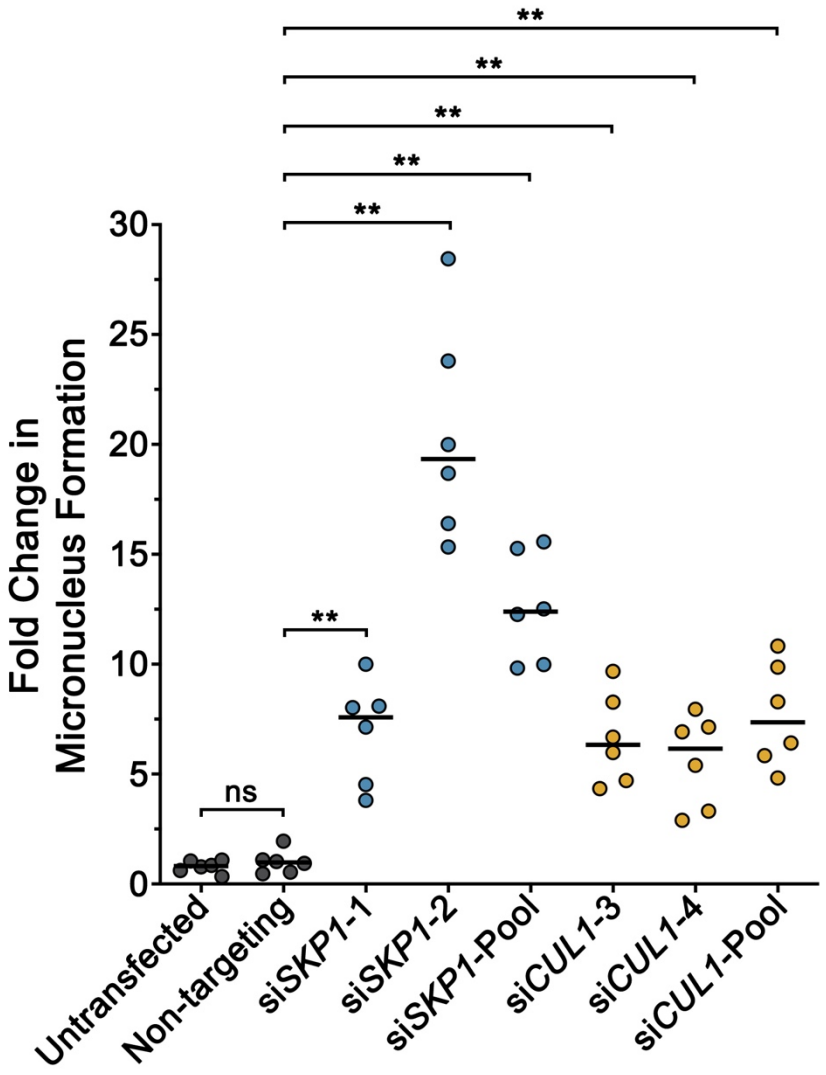

Figure 4-7. *SKP1* or *CUL1* Silencing Induces MNF in HCT116 Cells.
Dot plot depicting mean fold changes in MNF following *SKP1* or *CUL1* silencing, relative to non-targeting controls. Black lines identify the median of 6 replicate wells. N=3; n=6. Statistical significance is indicated (M-W test; ns, not significant; **, *P*-value < 0.01).

4.1.4. *SKP1* or *CUL1* Silencing Induces Increases in CIN Phenotypes in FT Cells.

To extend the findings from CRC into an HGSOC-relevant cellular context, *SKP1* or *CUL1* silencing was performed in FT194 and FT246 cell lines and the resulting changes in NAs and MNF were assessed using single-cell quantitative imaging microscopy as above. Fig. 4-8 and Fig. 4-9 depict the changes in NAs within FT194 and FT246 cells, respectively. Similar trends were observed in both FT cell lines, where *SKP1* silencing resulted in pronounced and statistically significant changes in NA cumulative frequency distributions (Table S4, Table S5), while *CUL1* silencing resulted in more subtle, but still significant changes in NA cumulative frequency distributions (Table S6, Table S7). Fig. 4-10 and Fig. 4-11 depict the changes in MNF within FT194 and FT246 cells, respectively, following *SKP1* or *CUL1* silencing. Similar to the NA results, *SKP1* silencing resulted in more pronounced MNF relative to *CUL1* silencing in both cell lines. Nonetheless, all *SKP1* or *CUL1* silenced conditions induced statistically significant increases in MNF, with the exception of si*CUL1*-4 (Table S8, Table S9). Collectively, these data indicate that the CIN phenotypes observed within HCT116 cells following *SKP1* and *CUL1* silencing also translate into an FT cellular context.

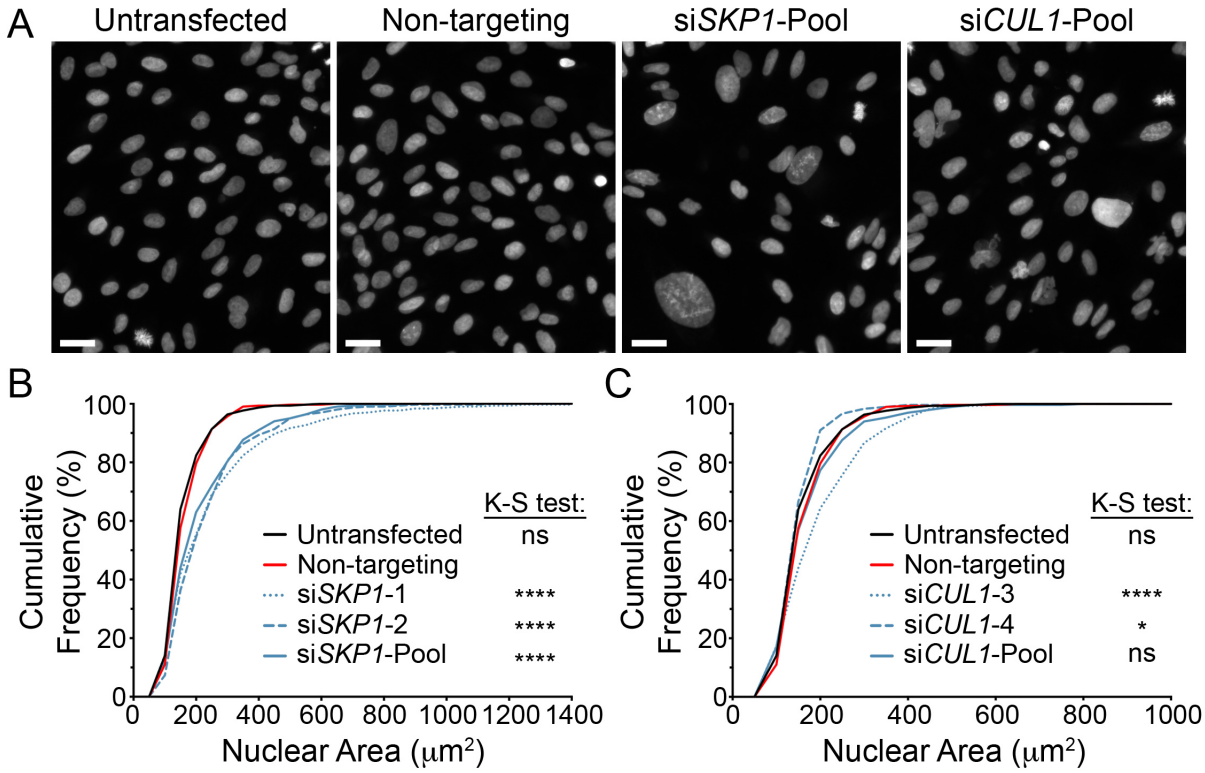

Figure 4-8. *SKP1* or *CUL1* Silencing Induces Changes in NAs in FT194 Cells.
(A) Representative images of Hoechst-counterstained nuclei showing qualitative changes in NAs following *SKP1* or *CUL1* silencing. Scale bar represents 30 μm. **(B)** NA cumulative frequency distributions following *SKP1* silencing relative to controls. K-S tests reveal statistically significant changes (*i.e.* rightward shift) in NA cumulative frequency distributions relative to non-targeting controls. N=3; 300 nuclei analyzed/condition. **(C)** NA cumulative frequency distributions following *CUL1* silencing relative to controls. K-S tests reveal statistically significant changes (*i.e.* rightward or leftward shift) in cumulative NA frequency distributions relative to non-targeting controls. N=3; 300 nuclei analyzed/condition. Statistical significance is indicated (ns, not significant; *, *P*-value < 0.05; ****, *P*-value < 0.0001).

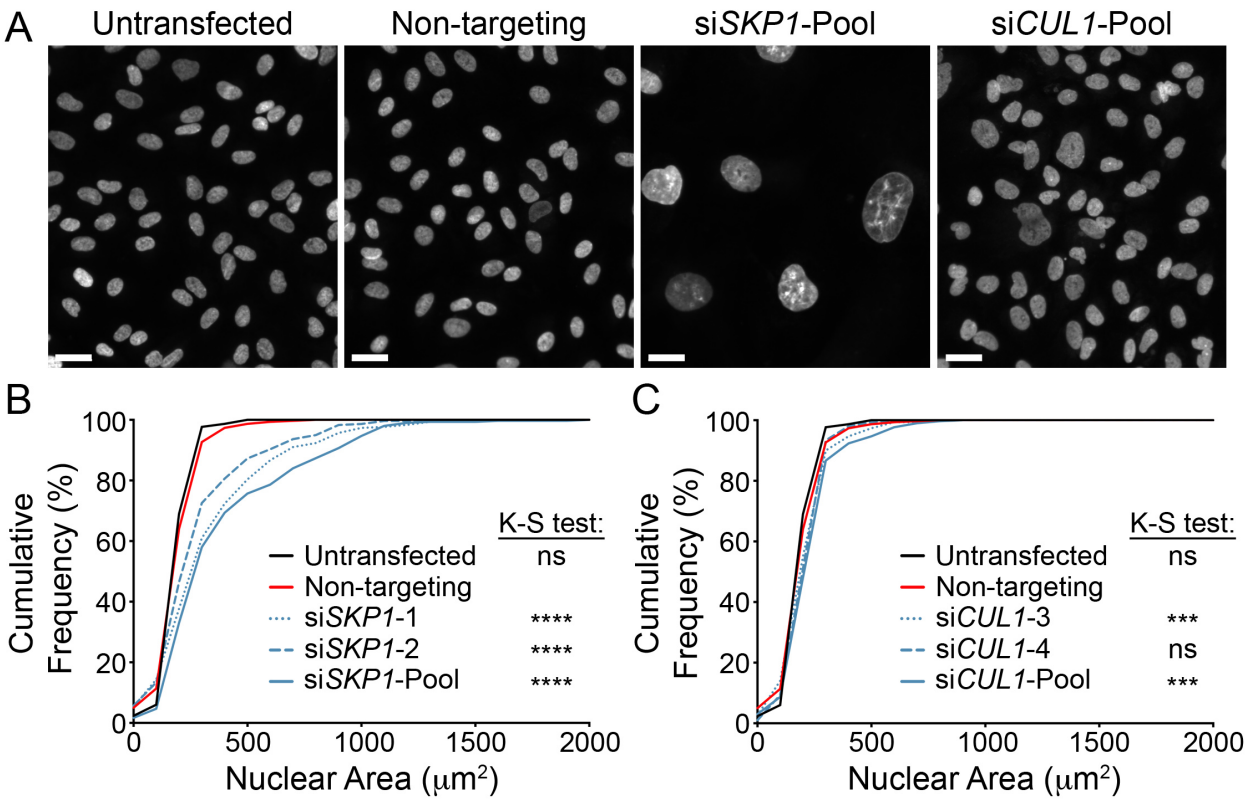

Figure 4-9. *SKP1* or *CUL1* Silencing Induces Changes in NAs in FT246 Cells.
((A) Representative images of Hoechst-counterstained nuclei showing qualitative changes in NAs following *SKP1* or *CUL1* silencing. Scale bar represents 30 μm. **(B)** NA cumulative frequency distributions following *SKP1* silencing relative to controls. K-S tests reveal statistically significant changes (*i.e.* rightward shift) in NA cumulative frequency distributions relative to non-targeting controls. N=3; 300 nuclei analyzed/condition. **(C)** NA cumulative frequency distributions following *CUL1* silencing relative to controls. K-S tests reveal statistically significant changes (*i.e.* rightward shift) in cumulative NA frequency distributions relative to non-targeting controls. N=3; 300 nuclei analyzed/condition. Statistical significance is indicated (ns, not significant; ***, p-value < 0.001; ****, p-value < 0.0001).

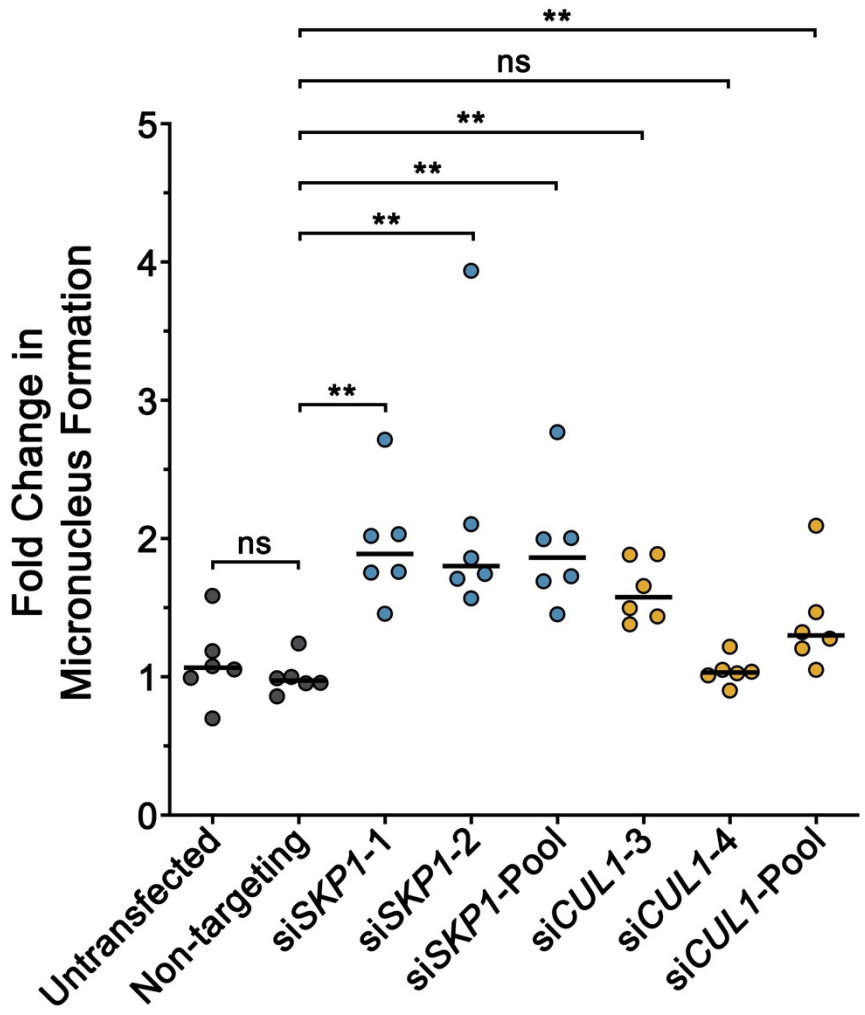

Figure 4-10. *SKP1* or *CUL1* Silencing Induces MNF in FT194 Cells.
Dot plot depicting mean fold changes in MNF following *SKP1* or *CUL1* silencing, relative to non-targeting controls. Black lines identify the median of 6 replicate wells. Statistical significance is indicated (M-W test; ns, not significant; **, *P*-value < 0.01). N=3; n=6.

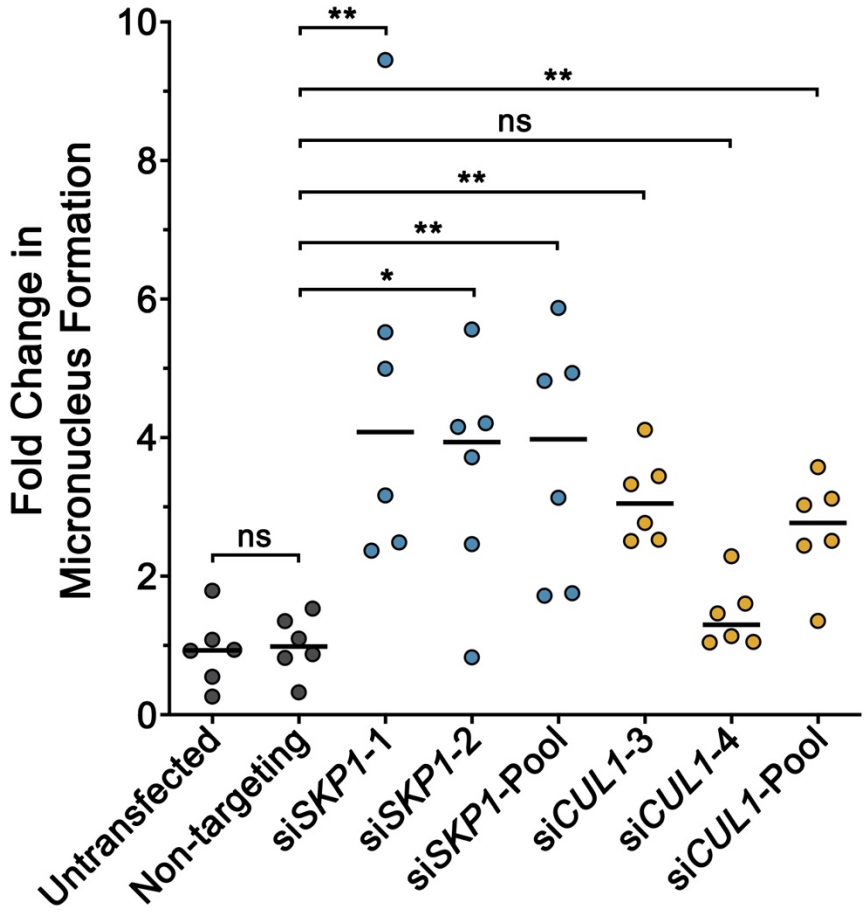

Figure 4-11. *SKP1* or *CUL1* Silencing Induces MNF in FT246 Cells.
Dot plot depicting mean fold changes in MNF following *SKP1* or *CUL1* silencing, relative to non-targeting controls. Black lines identify the median of 6 replicate wells. Statistical significance is indicated (M-W test; ns, not significant; *, *P*-value < 0.05; **, *P*-value < 0.01). N=3; n=6.

4.1.5. Diminished *SKP1* or *CUL1* Expression Induces CIN in FT Cells.

While the NA and MNF data provide preliminary evidence that *SKP1* or *CUL1* silencing induces CIN in FT194 and FT246 cells, these phenotypes do not enable direct assessment of chromosome numbers, and are therefore not synonymous with CIN. To directly evaluate chromosome numbers, mitotic chromosome spread analyses were performed in FT194 and FT246 cells following *SKP1* or *CUL1* silencing. A total of 100 mitotic chromosome spreads were enumerated for each *SKP1* or *CUL1* silenced condition and controls within FT194 (Fig. 4-12) and FT246 (Fig. 4-13) cells. Deviations from the modal chromosome complement for each cell line (46 chromosomes) were categorized as small-scale (< 10) or large-scale (≥ 10) chromosome gains or losses.

Within the FT194 cells, *SKP1* and *CUL1* silencing resulted in an overall increase in the percentage of mitotic spreads containing an abnormal number of chromosomes, which included both gains and losses. Large-scale chromosome gains were prevalent, particularly among the *SKP1* silenced cells, while large-scale chromosome losses were not observed. The distributions in chromosome numbers within *SKP1* or *CUL1* silenced FT194 cells were found to be statistically different than non-targeting controls (Table S10).

Due to the presence of 2 distinct subclones within the wild-type FT246 cell line (containing 46 or 44 chromosomes), the baseline percentage of "abnormal" mitotic spreads within control FT246 cells is elevated relative to FT194 cells (*i.e.* the "small-scale chromosome losses" class includes the FT246 subclone 2 which contains 44 chromosomes). Following *SKP1* or *CUL1* silencing, increases in small-scale chromosome gains and losses were observed. Large-scale changes were less common, and this is reflected in the statistical analyses (Table S11), which did not identify significant differences in chromosome number distributions as K-S tests are most

sensitive to changes within tail regions (*i.e.* extreme phenotypes). Importantly however, following *SKP1* or *CUL1* silencing in FT246 cells, the overall percentages of abnormal chromosome numbers were further increased from ~46% within the non-targeting control to ~71% and ~69% within cells silenced with *SKP1*-Pool and *CUL1*-Pool, respectively. Taken together with the NA and MNF data, these findings validate *SKP1* and *CUL1* as novel CIN genes in two independent FT cellular contexts.

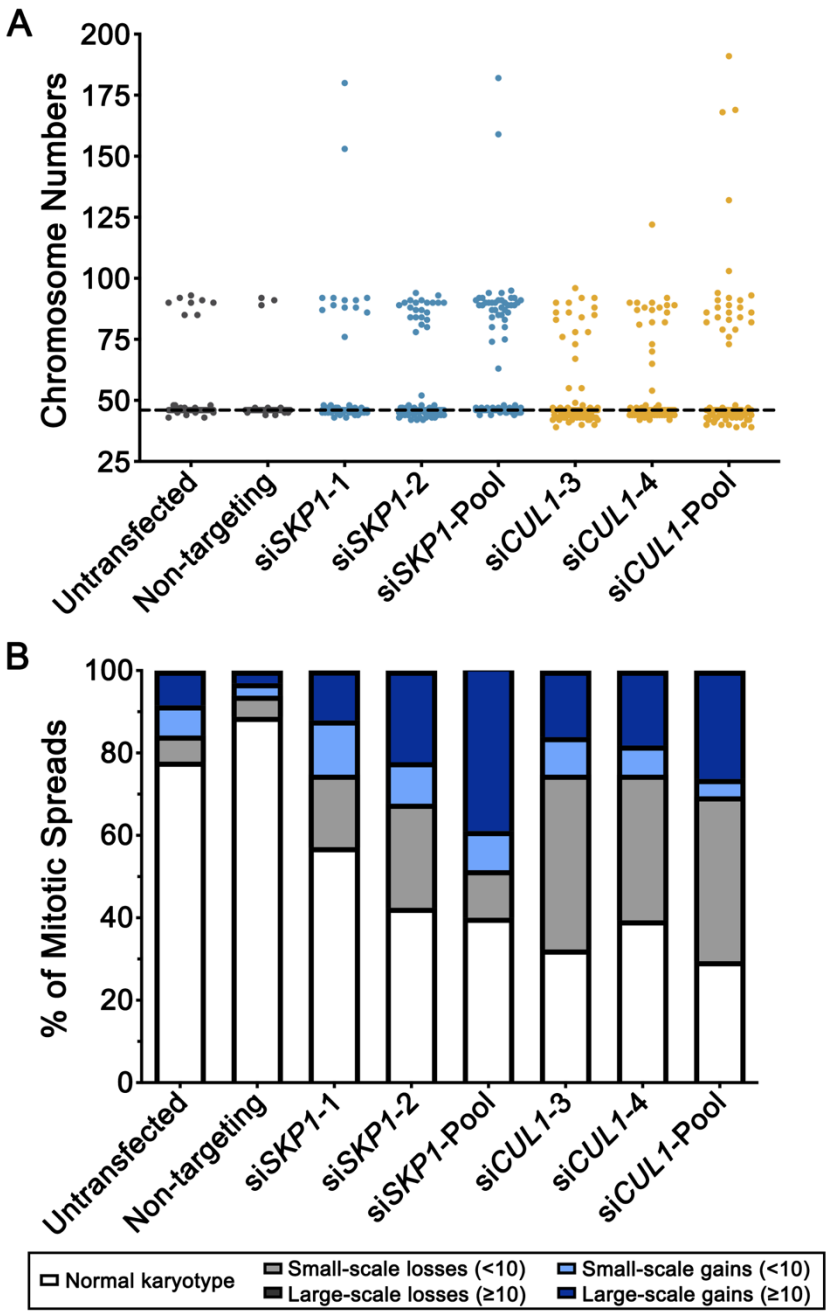

Figure 4-12. *SKP1* or *CUL1* Silencing Induces Chromosome Gains and Losses in FT194 Cells.

(A) Dot plot depicting chromosome numbers in control cells and following *SKP1* or *CUL1* silencing. The horizontal dotted line identifies the modal number of chromosomes for control cells (n=46). **(B)** Bar chart depicting the frequencies of small-scale (< 10) or large-scale (≥ 10) chromosome gains and losses relative to the modal chromosome number. N=2; 100 mitotic spreads analyzed per condition.

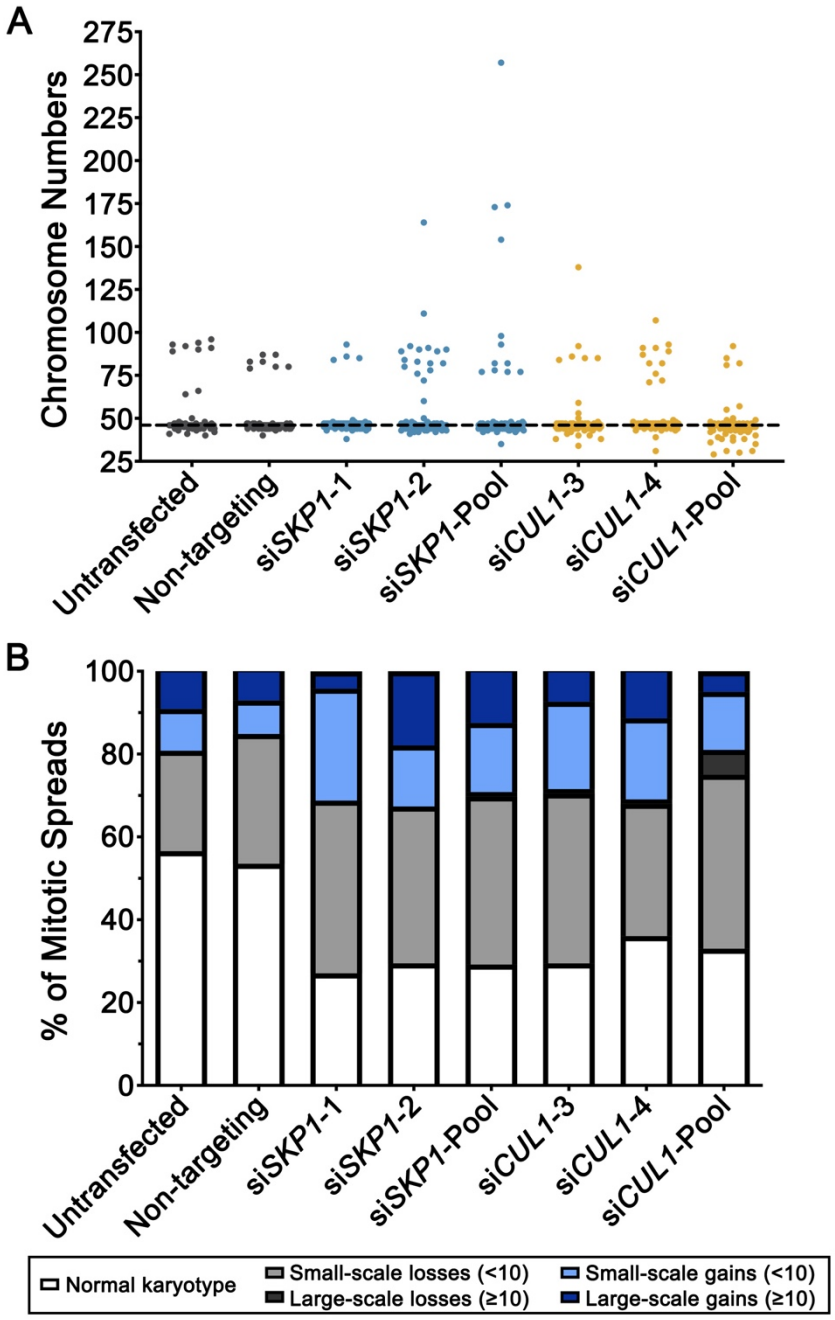

Figure 4-13. *SKP1* or *CUL1* Silencing Induces Chromosome Gains and Losses in FT246 Cells.

(A) Dot plot depicting chromosome numbers in control cells and following *SKP1* or *CUL1* silencing. The horizontal dotted line identifies the modal number of chromosomes for control cells (n=46). **(B)** Bar chart depicting the frequencies of small-scale (< 10) or large-scale (≥ 10) chromosome gains and losses relative to the modal chromosome number. N=2; 100 mitotic spreads analyzed per condition.

4.2. AIM 2: TO EVALUATE THE IMPACT HETEROZYGOUS LOSS OF *SKP1* HAS ON CIN AND FT CELL TRANSFORMATION.

Heterozygous loss of *SKP1* represents a clinically relevant model of alterations that are observed in ~46% of HGSOC patient samples[24], suggesting reduced expression may be implicated in HGSOC development and progression. On the other hand, homozygous loss of *SKP1* occurs in only 0.2% of HGSOCs, and insights from model organisms suggest that *SKP1* is an essential gene. Accordingly, a CRISPR/Cas9 approach was employed to generate stable *SKP1* heterozygous knockout (*SKP1*$^{+/-}$) clones in FT246 cells. This approach is complementary to the transient siRNA-based *SKP1* silencing methods described in Aim 1, but it enables the assessment of changes in CIN and cellular transformation phenotypes over time. Two FT246 *SKP1*$^{+/-}$ clones were generated and validated, and the temporal dynamics of CIN were assessed using established single cell quantitative imaging microscopy approaches. Cellular transformation-associated phenotypes were subsequently evaluated, including cell proliferation rates and anchorage-independent growth capacity.

4.2.1. Isolation and Validation of *SKP1*$^{+/-}$ Clones in FT246 Cells.

To generate *SKP1*$^{+/-}$ FT246 cells, two distinct sgRNAs targeting unique *SKP1* regions were employed. Both sgRNAs (hereafter referred to as sg*SKP1*-1 and sg*SKP1*-2) recognize a sequence within *SKP1* exon 3 (of 5 exons) and are expected to induce a DNA double-strand break (DSB) at those loci when complexed with the Cas9 endonuclease (Fig. 4-14). This CRISPR/Cas9 approach exploits the endogenous nonhomologous end joining (NHEJ) and nonsense-mediated mRNA decay (NMD) pathways to achieve heterozygous loss of *SKP1*. Conceptually, the repair of Cas9-induced DSBs by NHEJ (an error-prone DNA repair pathway) is expected to introduce indels

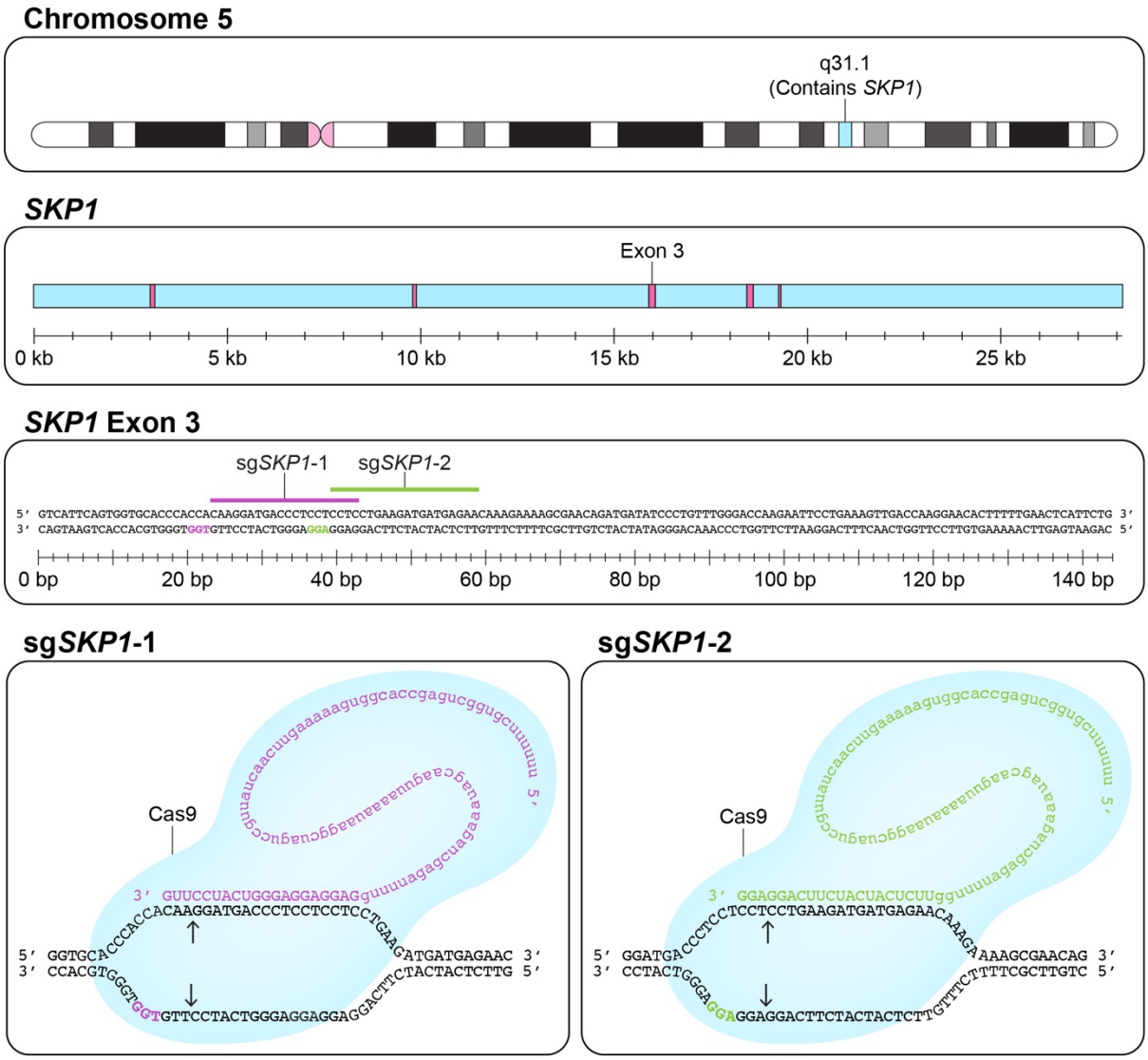

Figure 4-14. Expected Site of CRISPR/Cas9-Mediated Gene Editing.
Schematic depicting the *SKP1* binding site of two distinct sgRNAs (sg*SKP1*-1 and sg*SKP1*-2) employed for CRISPR/Cas9-mediated gene editing. *SKP1* localizes to 5q31.1 and consists of 5 exons spanning ~28 kilobases (kb) of DNA. *SKP1* exon 3 is 144 base pairs (bp) in length and is the site of sgRNA binding. Each sgRNA is composed of a variable 20 nt sequence at its 3' end (colored text with capital letters) which is complementary to a region within *SKP1*, and a constant 82 nt sequence at its 5' end (colored text with lowercase letters) that enables ribonucleoprotein complex formation with the Cas9 endonuclease. Cas9 induces a DNA DSB at the sites indicated by black arrows, which occur 3 bp upstream of the protospacer-adjacent motif (PAM; colored text) on the strand opposite to sgRNA binding.

of varying sizes within *SKP1* exon 3, some of which are expected to shift the reading frame and lead to a premature termination codon (PTC) in the resulting mRNA. NMD is typically activated following the introduction of a PTC located ≥50-55 nucleotides (nt) upstream of the last (3'-most) exon-exon junction, leading to degradation of the mRNA and loss of protein production from that allele[176,177]. Plasmids driving the co-expression of an sgRNA (sg*SKP1*-1, sg*SKP1*-2, or a non-targeting control sgRNA) and a tagBFP marker were delivered to FT246 cells via lentiviral transduction, and cells were sent for FACS to identify and isolate the successfully transduced populations (Fig. 4-15 A). Conservative gating parameters were used to collect only the cells with strong tagBFP expression and avoid collecting untransduced, tagBFP-negative cells. A total of 962,133 non-targeting, 124,130 sg*SKP1*-1, and 113,105 sg*SKP1*-2 cells were obtained as bulk populations, which represent transduction efficiencies of ~22.54%, 2.15%, and 1.78%, respectively (based on the number of cells sent for sorting). This variation in transduction efficiency may be a result of variation in lentiviral titers, as exact titers were not determined. Following sorting, cells were expanded, and a plasmid driving co-expression of Cas9 and GFP was subsequently delivered to the tagBFP-positive cell populations via lipid-based transfection. A second round of FACS was performed to isolate cells exhibiting strong expression of both tagBFP and GFP (Fig. 4-15 B). A total of 5,868 non-targeting, 8,162 sg*SKP1*-1, and 11,585 sg*SKP1*-2 cells were collected, which represent transfection efficiencies of ~0.92%, 0.59%, and 1.48%, respectively. In general, non-viral gene delivery methods (*e.g.* lipid-based transfection) have reduced efficiencies relative to viral delivery methods (*e.g.* lentiviral transduction)[178], which may explain the low Cas9 transfection efficiencies.

Individual clones from each of the three populations were isolated by performing a limiting dilution and expanding from a single cell. A total of 28 sg*SKP1*-transduced clones (10 sg*SKP1*-1

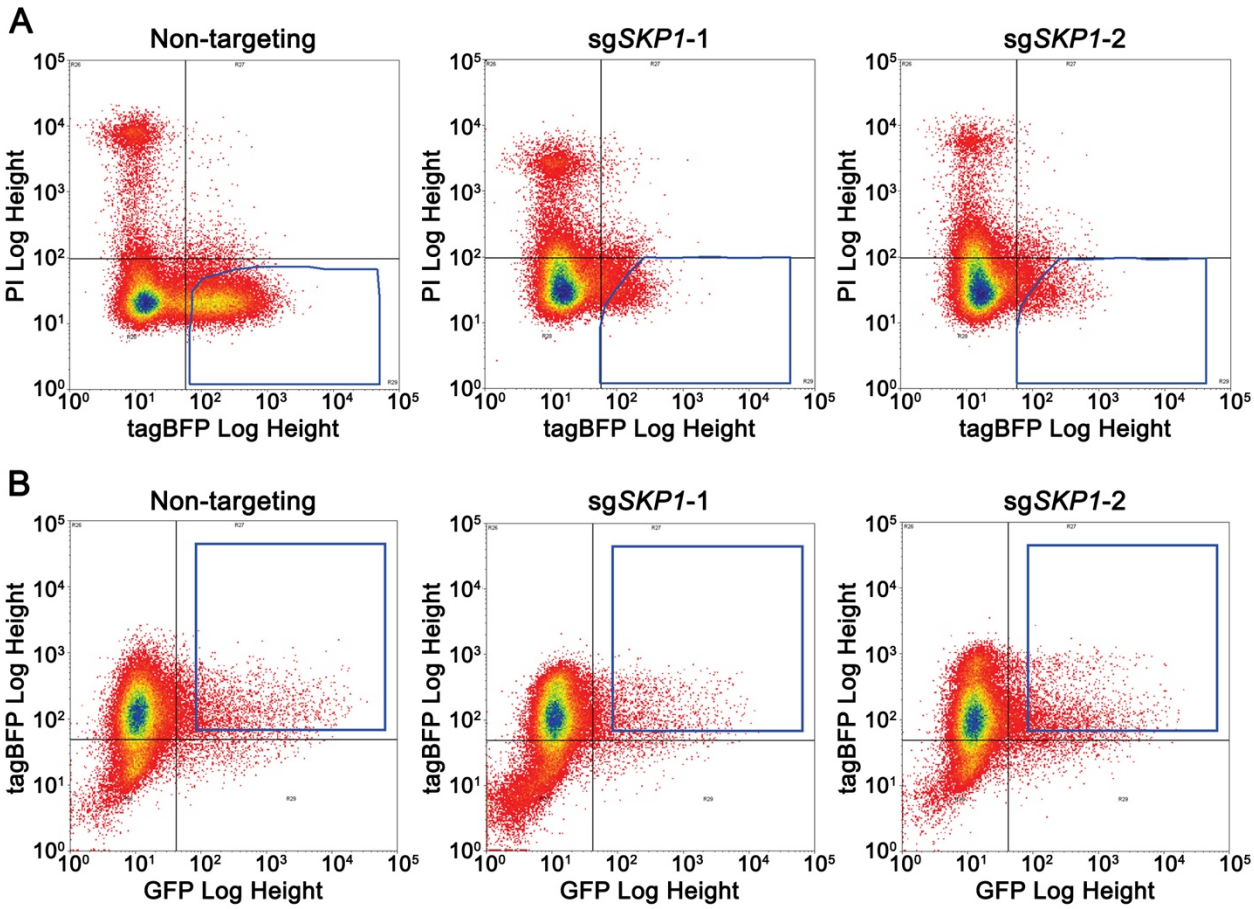

Figure 4-15. Isolation of Cells Containing CRISPR/Cas9 Components via FACS.
(A) FACS was performed on FT246 cells following lentiviral transduction with an sgRNA/tagBFP-expression plasmid (non-targeting, sg*SKP1*-1, or sg*SKP1*-2). Cells were sorted based on propidium iodide (PI; viability indicator) labeling and tagBFP expression. The blue bounding box identifies cells with low PI (*i.e.* viable) and high tagBFP expression (*i.e.* successfully transduced), which were collected as a bulk population for downstream experiments. **(B)** FACS was performed on tagBFP-positive FT246 cells following transient lipid-mediated transfection with a Cas9/GFP-expression plasmid. Cells were sorted based on PI labeling, tagBFP expression, and GFP expression. The blue bounding box identifies cells with high tagBFP expression and high GFP expression (*i.e.* successfully transfected), which were collected as a bulk population for downstream experiments.

and 18 sg*SKP1*-2) were screened for *SKP1* editing events via Western blot, and 10 clones (3 sg*SKP1*-1 and 7 sg*SKP1*-2) were selected to send for DNA sequencing based on an apparent reduction in SKP1 protein expression (Fig. 4-16). DNA sequencing confirmed heterozygous loss of *SKP1* within two clones (sg*SKP1*-1 Clone 3 and sg*SKP1*-2 Clone 9; hereafter named $SKP1^{+/-}$ 1 and $SKP1^{+/-}$ 2, respectively), based on the presence of an out-of-frame indel within one allele (Fig. 4-17 A). Specifically, $SKP1^{+/-}$ 1 retains one wild-type *SKP1* allele, and harbors a single bp (out-of-frame) insertion in its second allele, resulting in a PTC 2 codons downstream of the edit site in the mRNA. $SKP1^{+/-}$ 2 is a compound heterozygote harboring a single bp (out-of-frame) insertion in one allele, resulting in a PTC 1 codon downstream of the edit site in the mRNA, and a 6 bp (in-frame) deletion in its second allele, which is predicted to encode a mutant SKP1 protein in which two prolines are deleted (Fig. 4-17 B). In both clones, the out-of-frame insertions and PTC occur sufficiently far upstream to theoretically render each mRNA sensitive to NMD. In support of this possibility, semi-quantitative western blot analysis confirmed diminished SKP1 protein expression within $SKP1^{+/-}$ 1 and 2 relative to controls (Fig. 4-17 C). Interestingly, SKP1 expression was reduced to ~48% within $SKP1^{+/-}$ 1 and ~23% within $SKP1^{+/-}$ 2 relative to a non-targeting control clone. Collectively, these data confirm that FT246 $SKP1^{+/-}$ 1 and 2 are suitable for modeling *SKP1* heterozygous loss and the impact it has on CIN and FT cell transformation.

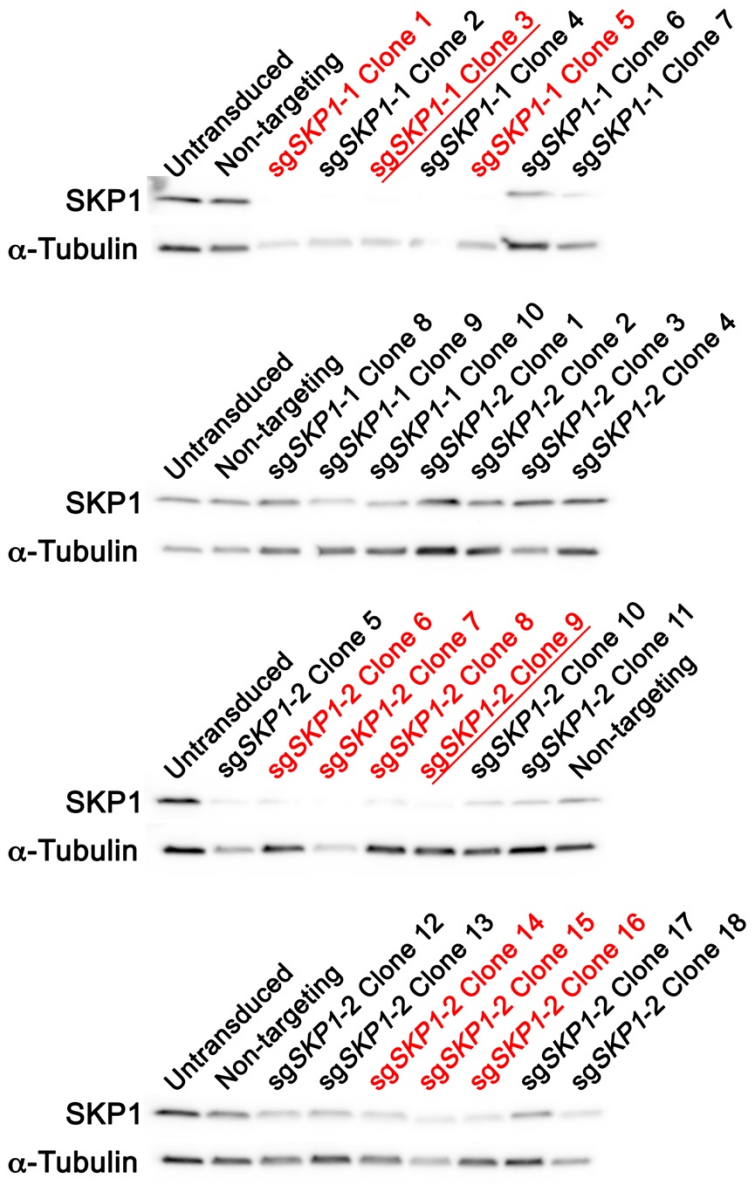

Figure 4-16. Screening for FT246 *SKP1*$^{+/-}$ Clones.
Western blots depicting SKP1 expression levels in 28 distinct FT246 clones isolated following CRISPR/Cas9 targeting of *SKP1* with one of two sgRNAs (sg*SKP1*-1 [10 clones] or sg*SKP1*-2 [18 clones]). Red text identifies 10 clones (3 sg*SKP1*-1 and 7 sg*SKP1*-2) that were selected and sent for DNA sequencing based on apparent decreases in SKP1 expression relative to controls and α-tubulin loading control. Underlined text identifies 2 clones in which heterozygous loss of *SKP1* was confirmed by DNA sequencing.

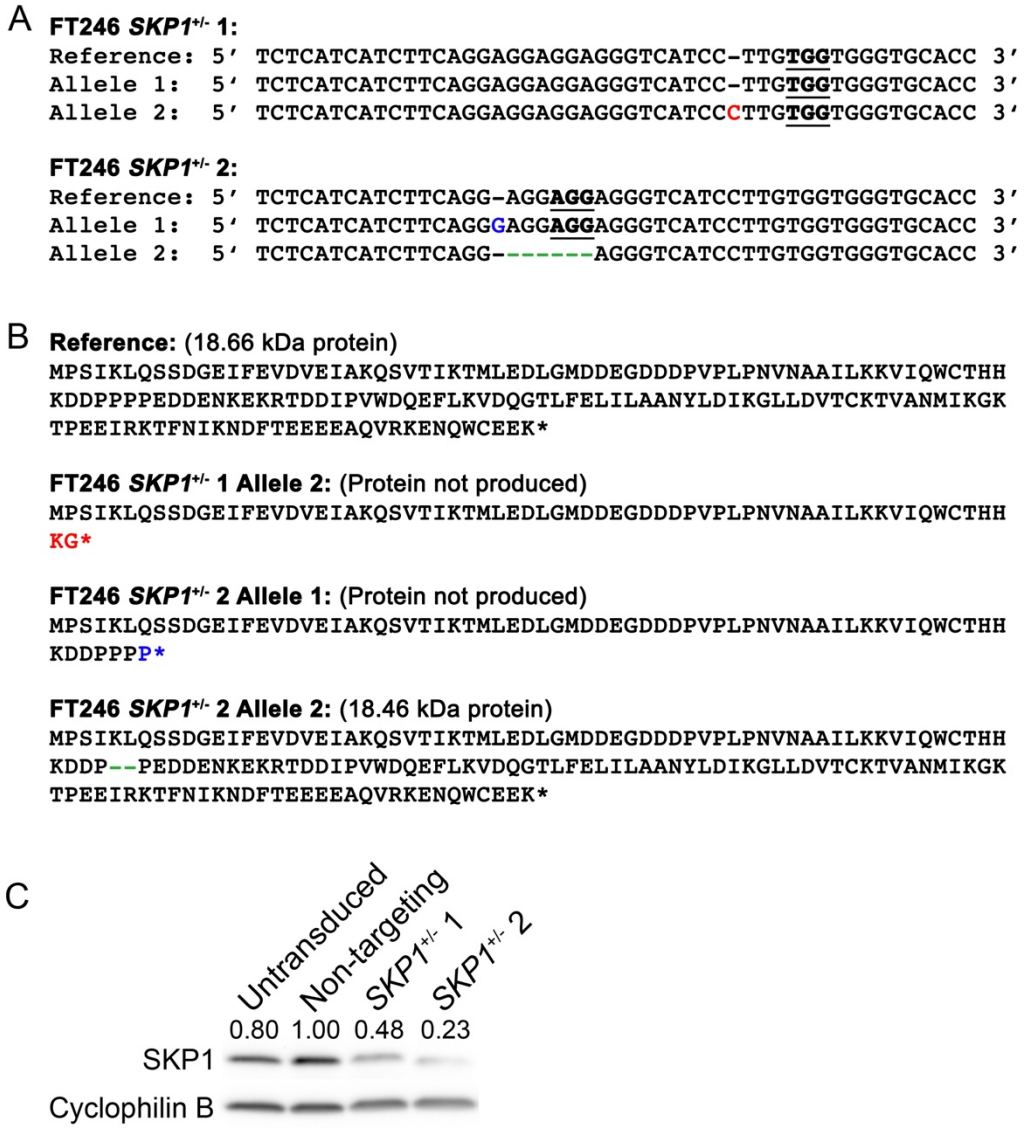

Figure 4-17. Validation of *SKP1* Heterozygotes.
(A) DNA sequencing results for individual *SKP1* alleles showing small indels (colored text) at the expected CRISPR edit site located 3 bp upstream of the NGG recognition sequence (protospacer adjacent motif [PAM]; underlined). *SKP1*$^{+/-}$ 1 retains one wild-type allele and harbors a 1 bp (out-of-frame) insertion in the second allele. *SKP1*$^{+/-}$ 2 harbors a 1 bp (out-of-frame) insertion in one allele, and a 6 bp (in-frame) deletion in the second allele. **(B)** Potential SKP1 amino acid sequences resulting from CRISPR-induced gene edits. Affected amino acids are shown in colored text. The out-of-frame edits in *SKP1*$^{+/-}$ 1 and *SKP1*$^{+/-}$ 2 are predicted to cause a frameshift and premature termination codon resulting in mRNA degradation by nonsense-mediated mRNA decay (*i.e.* the truncated protein shown above is not produced). In addition, the in-frame deletion within the second allele of *SKP1*$^{+/-}$ 2 is predicted to produce a mutant SKP1 protein containing a deletion of 2 adjacent prolines. Note that the exact position of the 2-proline deletion within the 4-proline stretch is unknown. **(C)** Semi-quantitative western blot showing reduced expression of SKP1 within *SKP1*$^{+/-}$ cells relative to controls. Cyclophilin B serves as a loading control.

4.2.2. Evaluating the Temporal Dynamics of CIN in *SKP1*$^{+/-}$ Cells.

To determine the long-term impact heterozygous loss of *SKP1* has on CIN, similar phenotypes (NA, MNF and chromosome enumeration) were assessed in both *SKP1*$^{+/-}$ 1 and *SKP1*$^{+/-}$ 2 at regular time intervals (*i.e.* every 4 passages) over a period of ~2.5 months. Both clones exhibited changes in NAs relative to a non-targeting control clone at all timepoints, with *SKP1*$^{+/-}$ 1 primarily exhibiting decreases in NAs and *SKP1*$^{+/-}$ 2 exhibiting increases in NAs as well as increased NA heterogeneity (Fig. 4-18). These NA changes were found to be statistically significant relative to the corresponding control at each timepoint using a K-S test (Table S12). In addition, *SKP1*$^{+/-}$ 2 (but not *SKP1*$^{+/-}$ 1) exhibited statistically significant increases in MNF relative to controls at each timepoint (Fig. 4-19; Table S13). Of the two *SKP1*$^{+/-}$ clones, the NA and MNF changes observed within *SKP1*$^{+/-}$ 2 most closely reflect the changes observed following *SKP1* silencing, and demonstrate the cell-to-cell heterogeneity that accompanies CIN. However, it is important to note that the NA assay is most sensitive to the detection of large-scale chromosome gains, and may not readily identify numerical changes involving only a small number of chromosomes. Similarly, the MNF assay is an indicator of S-CIN or small-scale chromosome missegregation events, but may not identify all instances of chromosome gains or losses. Thus, to validate the NA and MNF findings and gain more direct insight into the karyotypes of the two *SKP1*$^{+/-}$ clones, mitotic chromosome spread analyses were performed at the same 5 timepoints as above. Enumeration of 100 mitotic chromosome spreads for each condition revealed abnormal chromosome numbers within both *SKP1*$^{+/-}$ clones and dynamic fluctuations in chromosome complements over time (Fig. 4-20 A). Cumulative frequency distributions of chromosome numbers for both *SKP1*$^{+/-}$ clones were found to be statistically different than controls

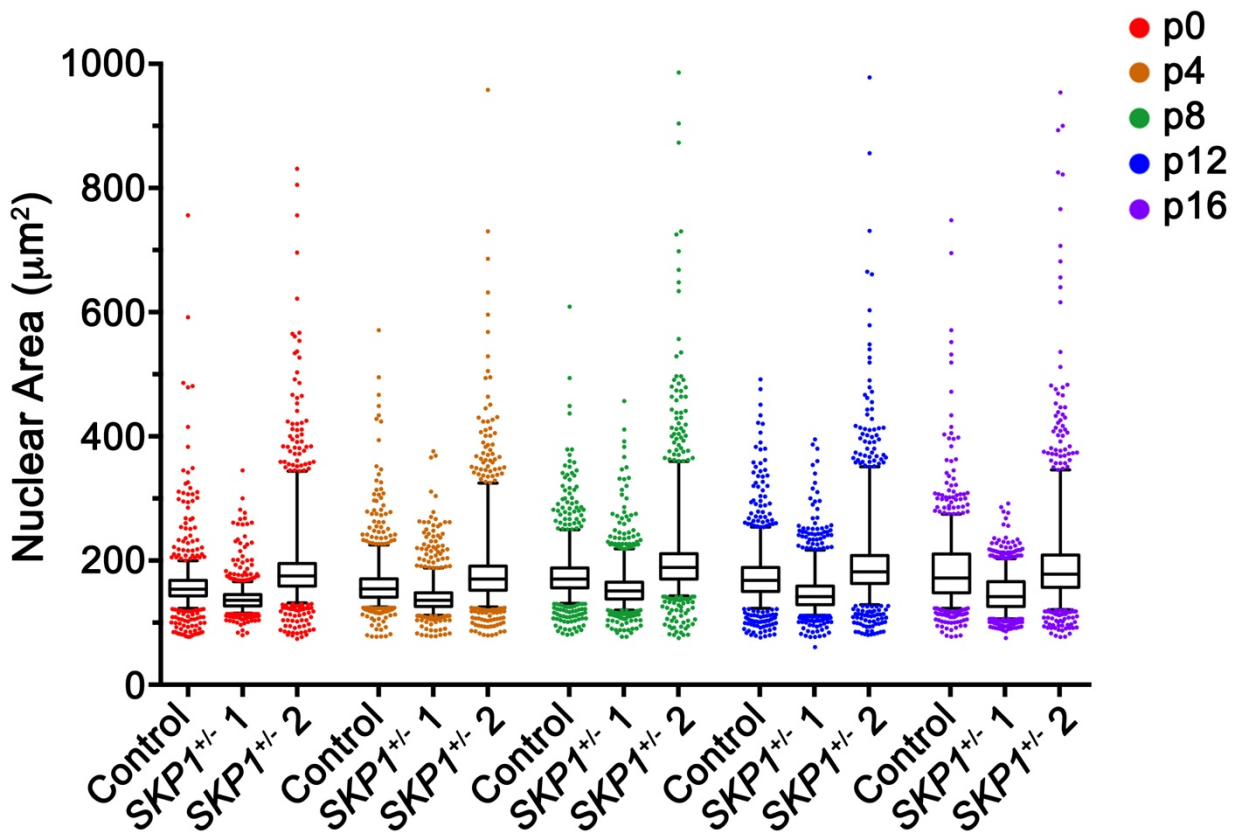

Figure 4-18. Heterozygous Loss of *SKP1* Induces Changes in NAs in FT246 Cells.
Box-and-whisker plots depicting NAs in two *SKP1*$^{+/-}$ clones and a non-targeting control at regular time intervals (*i.e.* every 4 passages [p]) over a period of 2.5 months. Boxes represent the interquartile ranges, with whiskers extending to the 5th and 95th percentiles. N=1; 100 nuclei × 12 replicate wells were analyzed per condition per timepoint.

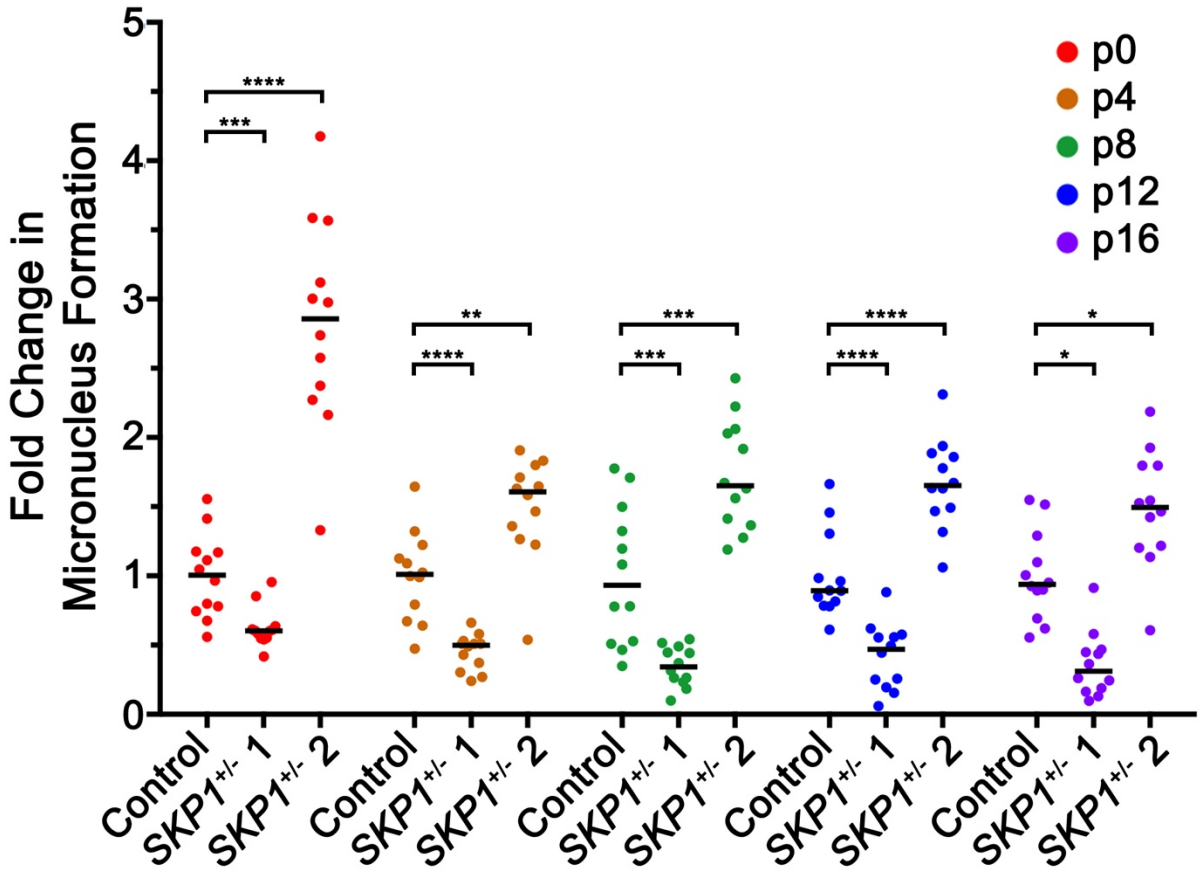

Figure 4-19. FT246 *SKP1*$^{+/-}$ Clone 2 Exhibits Increases in MNF.
Dot plot depicting fold changes in MNF in two *SKP1*$^{+/-}$ clones relative to a non-targeting control at regular time intervals (*i.e.* every 4 passages [p]) over a period of 2.5 months. Black lines identify the median of 12 replicate wells. Statistical significance at each timepoint relative to the non-targeting control is indicated (M-W test; *, *P*-value < 0.05; **, *P*-value < 0.01; ***, *P*-value < 0.001; ****, *P*-value < 0.0001). N=1; n=12.

at each timepoint using a K-S test (Table S14). Importantly, the non-targeting control clone and *SKP1*$^{+/-}$ 2 were found to have a modal chromosome number of 46, while *SKP1*$^{+/-}$ 1 had a modal chromosome number of 44, suggesting that these clonal derivative cell lines were generated from distinct subclones that were present within the parental FT246 cell line. Accordingly, changes in chromosome numbers were categorized as small-scale (< 10) or large-scale (≥ 10) gains or losses relative to the modal chromosome number specific to each clone (Fig. 4-20 B).

Interestingly, *SKP1*$^{+/-}$ 1 was most susceptible to chromosome losses (small-scale and large-scale), which were most frequently observed at p0, p12, and p16. On the other hand, *SKP1*$^{+/-}$ 2 exhibited both losses (small-scale) and gains (small-scale and large-scale) of chromosomes, which were generally observed at all five timepoints. The overall frequencies of abnormal chromosome numbers (*i.e.* deviations from the modal number) ranged from ~20-55% for *SKP1*$^{+/-}$ 1 and ~55-80% for *SKP1*$^{+/-}$ 2. In general, these data suggest a more "extreme" level of CIN exists within *SKP1*$^{+/-}$ 2 relative to *SKP1*$^{+/-}$ 1, which may be due to their different genetic backgrounds, a difference in underlying mechanism responsible for the specific class of chromosomal changes observed, or a potential difference in the evolutionary trajectory of these populations during clonal expansion. Despite these differences, mitotic chromosome spread analyses confirmed ongoing cell-to-cell heterogeneity and N-CIN within both *SKP1*$^{+/-}$ clones, which may have implications for their predisposition to cellular transformation.

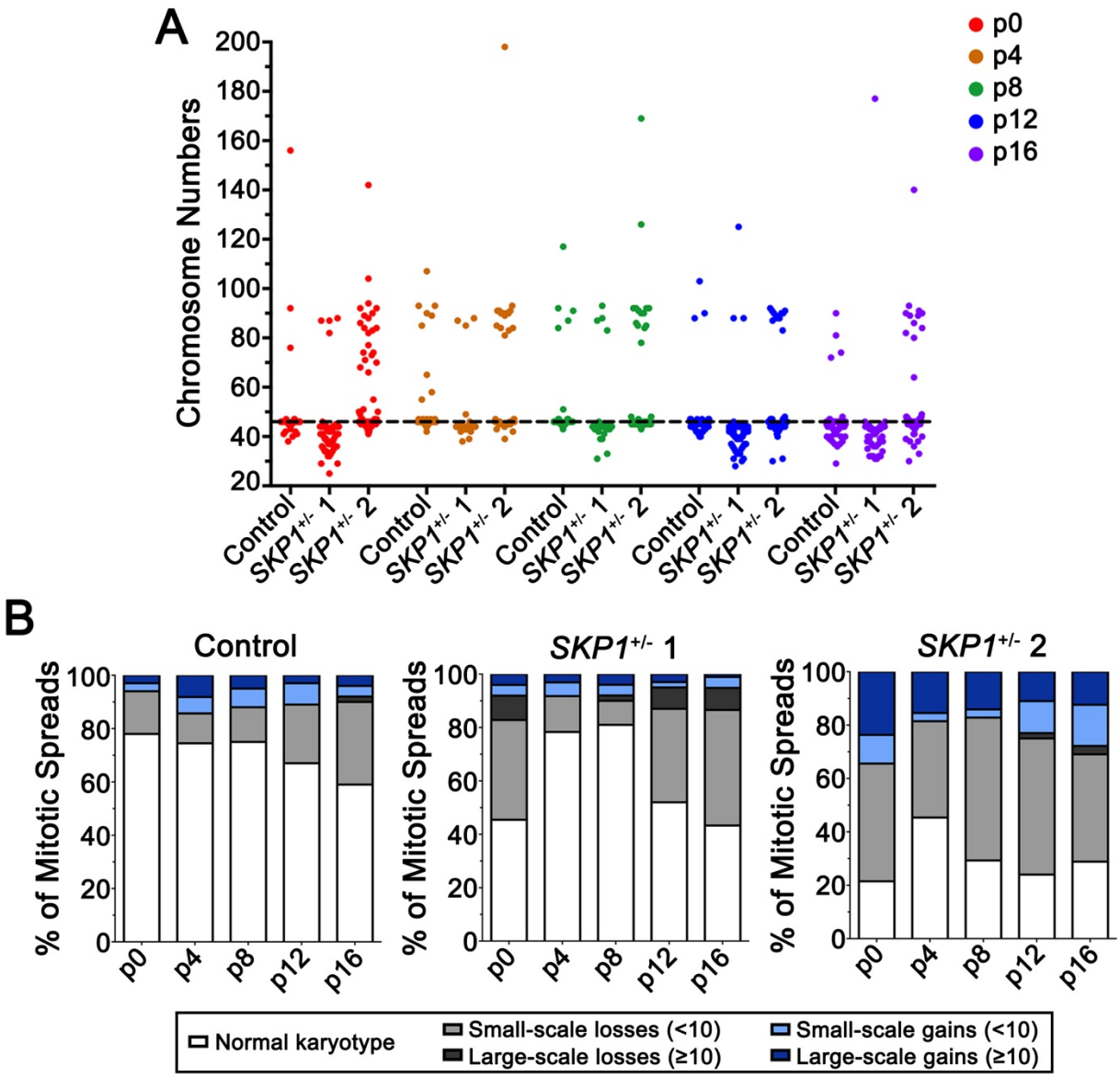

Figure 4-20. Heterozygous Loss of *SKP1* Induces Dynamic Changes in Chromosome Numbers.

(A) Dot plot depicting chromosome numbers in two *SKP1*$^{+/-}$ clones and a non-targeting control at regular time intervals (*i.e.* every 4 passages [p]) over a period of 2.5 months. The horizontal dotted line identifies the modal chromosome number of control cells (n=46). **(B)** Bar charts depicting the frequencies of small-scale (< 10) or large-scale (≥ 10) chromosome gains and losses relative to the modal chromosome number (n=46 for control and *SKP1*$^{+/-}$ 2; n=44 for *SKP1*$^{+/-}$ 1). N=1; 100 mitotic spreads were analyzed per condition per timepoint.

4.2.3. Derivative FT246 Cells Retain Expression of PAX8 and Absence of TP53.

TP53 mutations leading to altered TP53 expression and function (loss-of-function [LOF] or oncogenic gain-of-function [GOF]) are required for FT cell transformation and occur in virtually all HGSOCs[24,40,41]. Parental (untransduced) FT246 cells harbor *TP53* shRNA and are expected to model the LOF commonly observed in HGSOC samples. In addition to the absence of TP53 expression, parental FT246 cells are expected to express PAX8, a Müllerian lineage marker that is expressed within the fallopian tube epithelium and in serous ovarian cancers but not in normal ovarian tissue[179,180]. To determine whether the three clonal derivative FT246 cell lines (non-targeting, *SKP1*$^{+/-}$ 1 and *SKP1*$^{+/-}$ 2) retain these parental phenotypes, indirect immunofluorescent labeling was performed using antibodies targeting either TP53 (both wild-type and mutant forms) or PAX8, and images were acquired using identical exposure times. OVCAR3 HGSOC cells were used as a positive control as they express both mutant oncogenic TP53 (R248Q)[181] and PAX8[179]. HCT116 CRC cells were used as a negative control for PAX8 expression. As shown in Fig. 4-21, TP53 is completely absent within all parental (untransduced) and derivative (non-targeting, *SKP1*$^{+/-}$ 1, *SKP1* $^{+/-}$ 2) FT246 cells, as expected. While PAX8 expression appears greatest in OVCAR3 and untransduced FT246 cells, it is also present in both *SKP1*$^{+/-}$ clones (Fig. 4-22). Collectively, these data confirm that the derivative FT246 cell lines (and importantly *SKP1*$^{+/-}$ 1 and *SKP1*$^{+/-}$ 2) retain the critical features of the parental FT246 cell line.

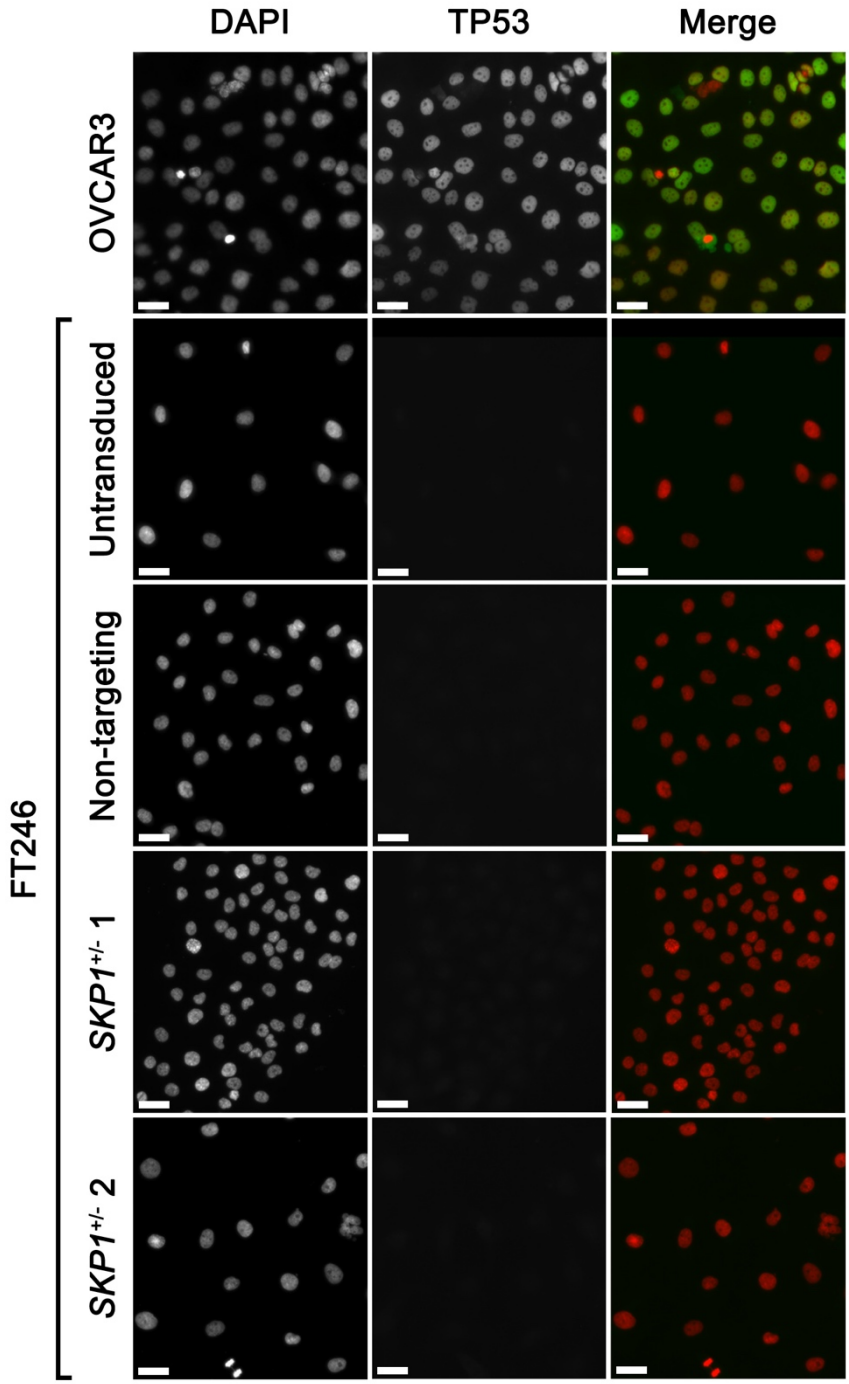

Figure 4-21. TP53 is Not Expressed in Parental and Derivative FT246 Cells.
Representative low resolution images of nuclear TP53 labeling within parental and derivative FT246 cell lines. OVCAR3 serves as a positive control. Images were acquired using identical exposure times, and therefore qualitative changes in TP53 labeling are indicative of changes in TP53 expression levels. Scale bar represents 30 μm. N=1.

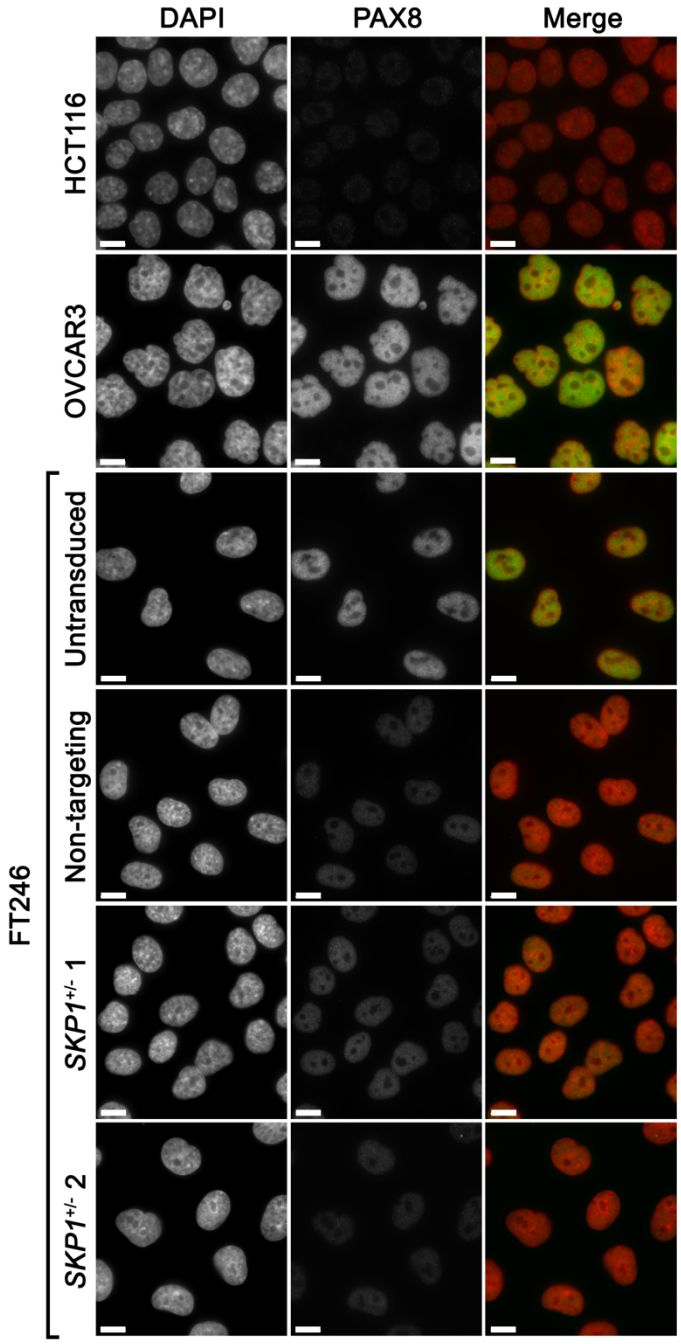

Figure 4-22. PAX8 is Expressed in Parental and Derivative FT246 Cells.
Representative images of nuclei following PAX8 labelling within parental and derivative FT246 cell lines. HCT116 cells and OVCAR3 cells serve as negative and positive controls, respectively. Images were acquired using identical exposure times. Parental FT246 cells (untransduced) and FT246 derivatives (non-targeting, *SKP1*$^{+/-}$ 1, *SKP1* $^{+/-}$ 2) express PAX8, which is indicative of their Müllerian origin. Scale bar represents 10 μm. N=1.

4.2.4. Evaluating Cellular Transformation Parameters in *SKP1*$^{+/-}$ Cells.

To evaluate the extent to which heterozygous loss of *SKP1* and the resulting cell-to-cell N-CIN contributes to cellular transformation of FT246 cells (in combination with the complete absence of TP53), two cellular transformation parameters were evaluated: 1) cell proliferation rates; and 2) anchorage independent growth capacity. To assess cell proliferation rates, RTCA proliferation curves were generated for FT246 *SKP1*$^{+/-}$ 1 and *SKP1*$^{+/-}$ 2 and compared to controls (parental [untransduced] FT246 cells and a non-targeting clonal derivative) (Fig. 4-23). The RTCA curves for all four cell lines exhibit an initial lag phase, followed by a steady increase (log phase) in cell index, and a final plateau (stationary phase). The slopes of the cell index curves for control cells and *SKP1*$^{+/-}$ 1 are comparable, while *SKP1*$^{+/-}$ 2 appears to have an increased slope and reaches stationary phase at an earlier timepoint relative to the other conditions (~5 days post-seeding vs. ~7 days post-seeding). These data suggest *SKP1*$^{+/-}$ 2 has a growth advantage, or alternatively, may have a larger cell size causing an overall increase in cell index.

To complement RTCA data and to better distinguish between growth (*i.e.* cell sizes) and proliferation (*i.e.* cell numbers), nuclear enumeration assays were employed to evaluate the rate of change in nuclear numbers over a period of 16 days (Fig. 4-24). All cell lines exhibited a logistic growth pattern[182], which is characterized by a decrease in proliferation rate as the population approaches a maximum number of nuclei, suggesting a confluent well. Interestingly, there were large differences in the maximum number of nuclei achieved for the various cell lines, particularly between the two *SKP1*$^{+/-}$ clones. At the experimental endpoint, an average of 1835, 1506, 2227, and 1112 nuclei per well were detected for untransduced, non-targeting, *SKP1*$^{+/-}$ 1 and *SKP1*$^{+/-}$ 2 cells, respectively. While a small amount of variation can be expected due to the distribution of cells within the wells, this represents a ~2-fold increase in the final nuclear density for *SKP1*$^{+/-}$ 1

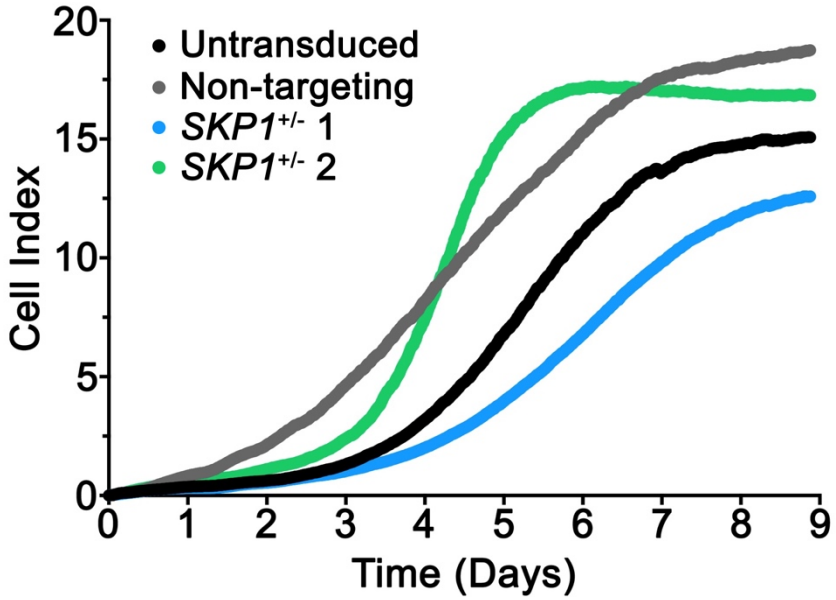

Figure 4-23. FT246 *SKP1*$^{+/-}$ Clone 2 Exhibits an Apparent Increase in Proliferation Rate. RTCA proliferation curves for control and *SKP1*$^{+/-}$ FT246 cells. The slope of the curve is qualitatively increased in *SKP1*$^{+/-}$ 2 relative to the other cell types, which suggests an increased cell growth or proliferation rate. N=2; n=4.

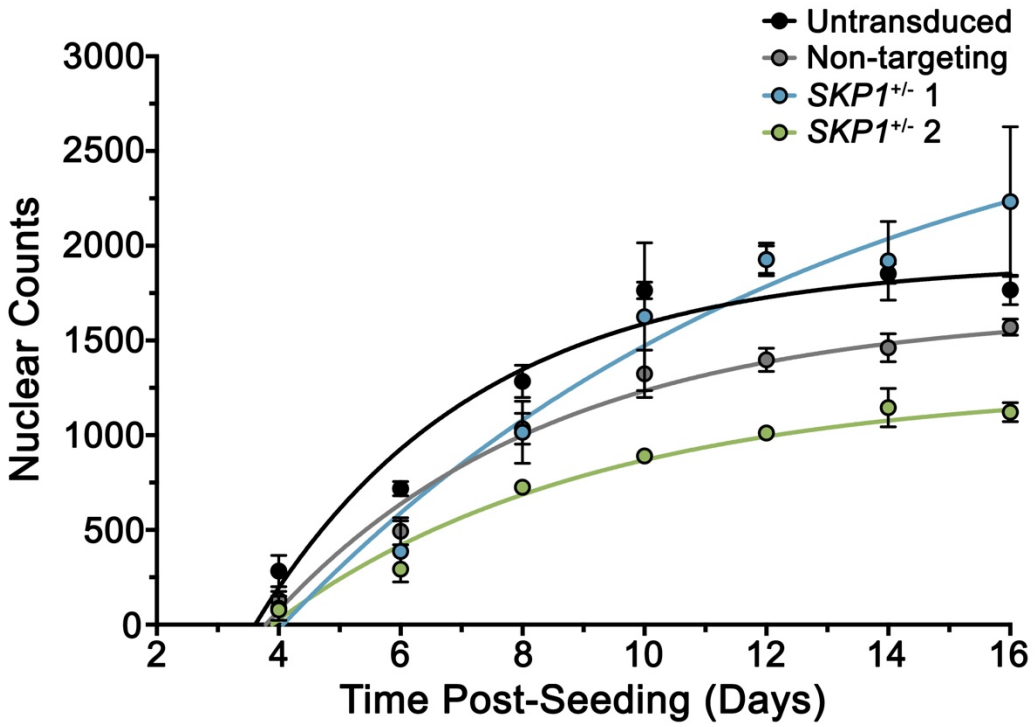

Figure 4-24. Nuclear Densities Vary Between FT246 *SKP1*$^{+/-}$ Clones.
Nuclear enumeration curves for FT246 SKP1$^{+/-}$ and control cells follow a logistic growth model and reach a plateau at variable nuclear densities. N=2; n=6.

compared to *SKP1*$^{+/-}$ 2, which contrasts with the apparent increase in growth/proliferation of *SKP1*$^{+/-}$ 2 as measured by RTCA. To investigate potential morphological factors (*e.g.* cell body size) accounting for the differences in nuclear densities, fluorescently-conjugated WGA labeling was employed to visualize cell bodies of *SKP1*$^{+/-}$ clones and control cells. This approach revealed striking differences in morphology between the two *SKP1*$^{+/-}$ clones, with *SKP1*$^{+/-}$ 1 exhibiting small and tightly-packed cell bodies, and *SKP1*$^{+/-}$ 2 exhibiting heterogeneous cell body sizes, some of which were very large (Fig. 4-25). Thus, the more rapid growth/proliferation of *SKP1*$^{+/-}$ 2 suggested by the RTCA data could simply reflect an increase in cell size.

To determine whether heterozygous loss of *SKP1* contributes to the acquisition of anchorage-independent growth capacity in FT246 cells, soft agar colony formation assays were conducted for each line. Cells were embedded in a soft agar matrix and colony formation was assessed after 4 weeks of growth. Only the HCT116 positive control cell line formed colonies that were macroscopically visible with crystal violet staining (an average of 4 colonies out of 50,000 cells seeded per well; Fig. 4-26 A,C). In addition, microscopically visible colonies ≥ 100 μm in diameter were observed in HCT116 cells (an average of 21 colonies out of 50,000 cells seeded per well), and to a lesser extent in FT246 *SKP1*$^{+/-}$ 2 (an average of 0.33 colonies out of 50,000 cells seeded) (Fig. 4-26 B,D). Interestingly, while OVCAR3 cells did not form any microscopic colonies ≥ 100 μm, these cells exhibited a qualitative increase in the number of smaller colonies that did not meet the 100 μm size threshold set for automated analyses (Fig. 4-26 B) which may be a result of their slower cell proliferation rate. In general, under these experimental conditions, heterozygous loss of *SKP1* does not appear to induce profound increases in cellular transformation phenotypes.

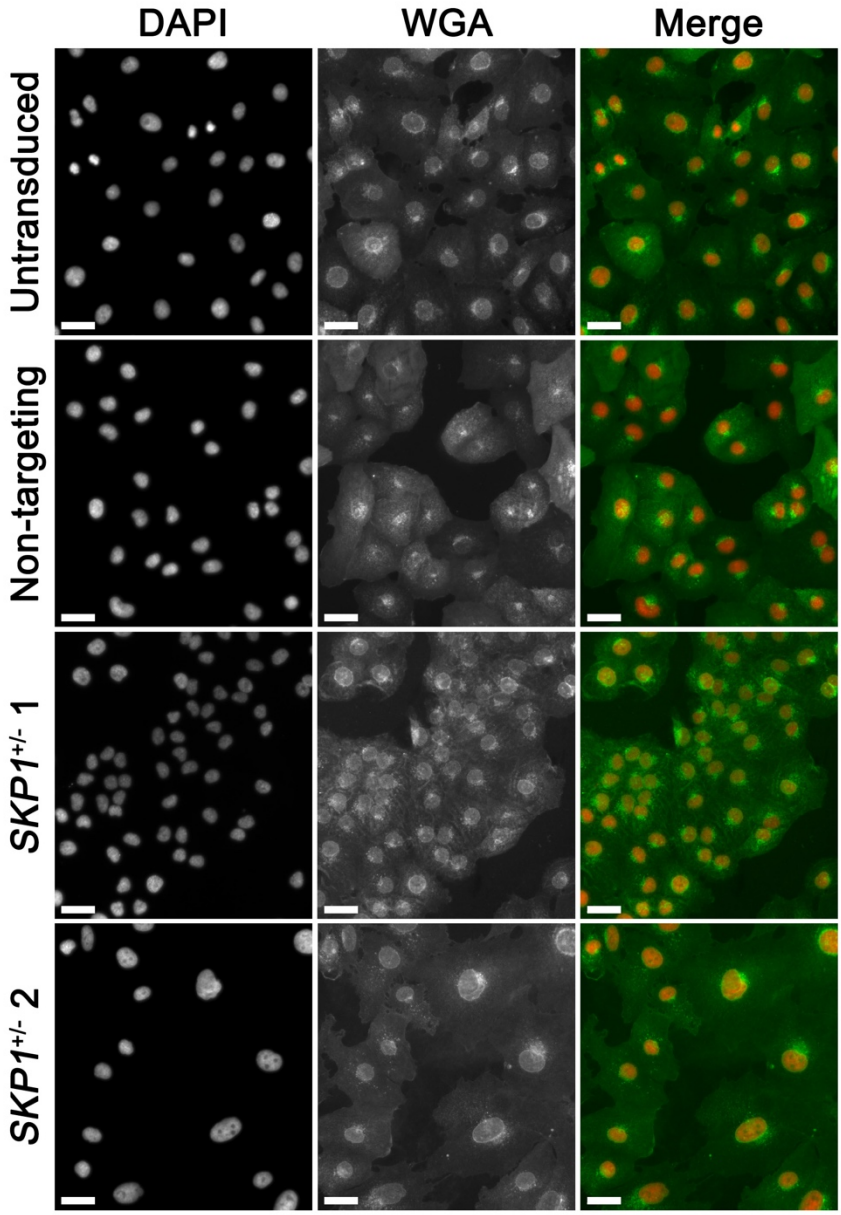

Figure 4-25. FT246 *SKP1*$^{+/-}$ Clones are Morphologically Distinct.
Representative images of *SKP1*$^{+/-}$ and control FT246 cells following labeling with fluorescently-conjugated WGA to identify cell body boundaries. *SKP1*$^{+/-}$ 1 is characterized by small, tightly-packed cell bodies, while *SKP1*$^{+/-}$ 2 is characterized by heterogeneous and/or very large cell body sizes. Scale bar represents 30 μm. N=1.

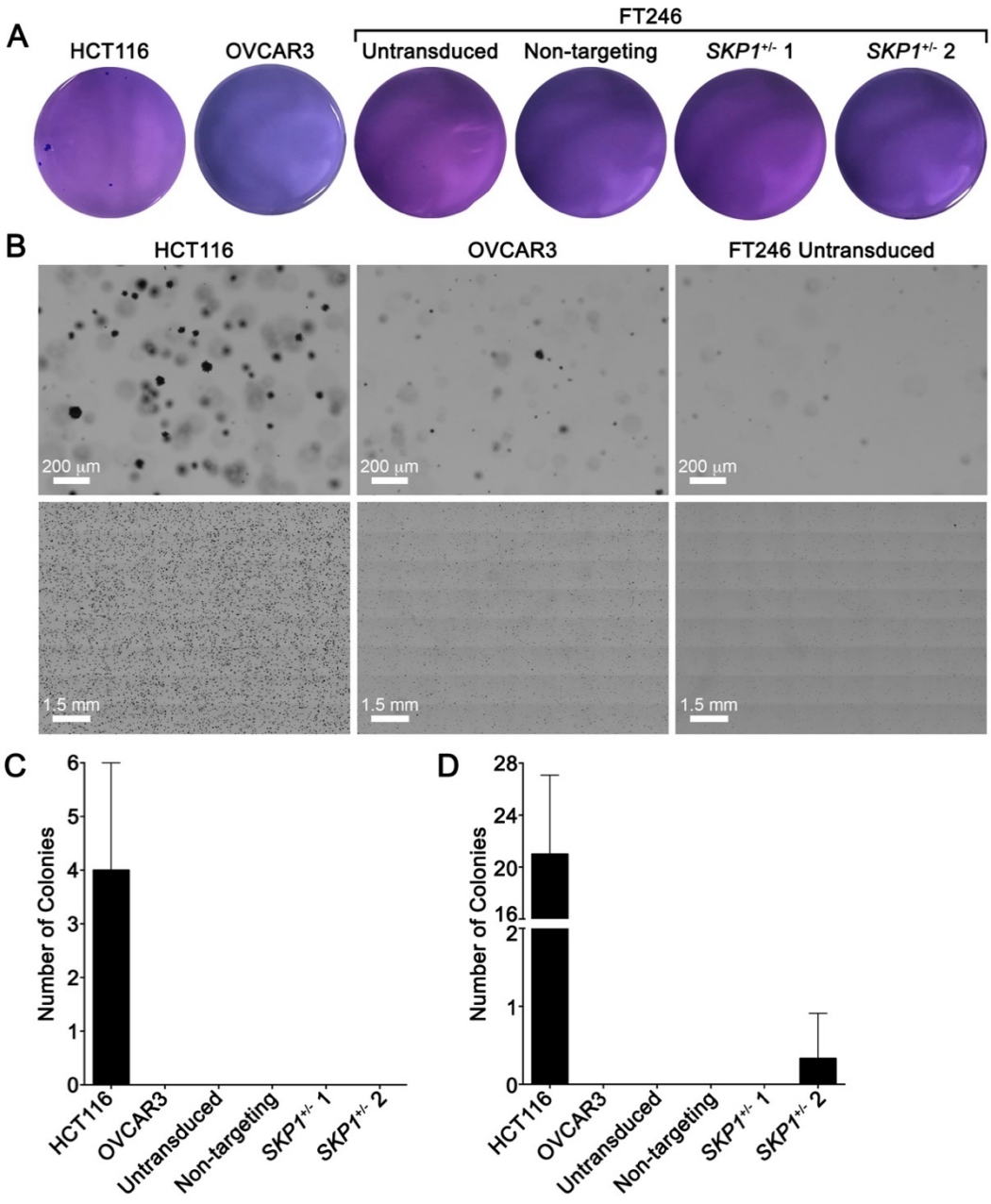

Figure 4-26. Heterozygous Loss of *SKP1* Does Not Induce Colony Formation in Soft Agar. **(A)** Representative images of macroscopic colony formation in soft agar for the indicated cell types. HCT116 cells were used as a positive control. **(B)** Representative images of microscopic colony formation in soft agar for the indicated cell types. Top panel depicts a single 4× image at a single focal plane. Bottom panel depicts a montage image produced from a total of 704 (4×) images (8×8 matrix of images × 11 slices). **(C)** Bar chart depicting the mean number of macroscopically visible colonies per well ± the standard deviation. **(D)** Bar chart depicting the mean number of microscopically visible colonies (≥ 100 μm) per stitched image ± the standard deviation. N=2; n=3.

CHAPTER 5. CONCLUSIONS AND DISCUSSION

5.1. SUMMARY AND CONCLUSIONS

In this thesis, two complementary approaches were employed to study the effects of diminished *SKP1* or *CUL1* expression, which are suspected to underlie CIN in the early stages of HGSOC development. The first part of this study utilized siRNA-based approaches to induce transient silencing of *SKP1* or *CUL1*, which resulted in strong decreases in SKP1 and CUL1 protein levels ($\leq$ 10% of endogenous levels) and corresponding increases in Cyclin E1 levels. Statistically significant increases in CIN phenotypes were observed following *SKP1* or *CUL1* silencing within three distinct cell lines (HCT116, FT194, and FT246), including changes in NAs, increases in MNF, and changes in chromosome numbers. Interestingly, CIN phenotypes were more extreme within the *SKP1*-silenced cells relative to *CUL1*-silenced cells across all three cell lines, implying SKP1 and CUL1 may have disparate functions beyond the SCF complex. In addition, these data identify *SKP1* and *CUL1* as novel CIN genes within various cellular contexts including in HGSOC precursor cells.

While the low levels of SKP1 and CUL1 expression achieved with siRNA-mediated gene silencing provided critical insight into the roles SKP1 and CUL1 have in regulating Cyclin E1 levels and chromosome stability, these models may not reflect the type of alterations that are most frequently observed within clinical samples. For example, in HGSOC patient samples, homozygous loss of *SKP1* is a rare occurrence (0.2% of cases), while heterozygous loss is observed within ~46% of patients[24]. Thus, the second part of this study focused on modeling these clinically relevant alterations and evaluating the impact heterozygous loss of *SKP1* has on CIN and FT cell transformation. Two FT246 *SKP1*$^{+/-}$ clones were generated using CRISPR/Cas9 and CIN was assessed over time. This work revealed dynamic changes in chromosome numbers and distinct

CIN phenotypes between the two clones. However, the two *SKP1*$^{+/-}$ clones did not exhibit increases in transformation-associated phenotypes including cell proliferation rates or anchorage-independent growth capacity, suggesting additional genetic or environmental factors may be required to induce FT cell transformation. Overall, this work is the first to investigate the underlying origins of CIN in HGSOC and provides a foundation on which to continue investigating the early events contributing to HGSOC pathogenesis.

5.2. HETEROGENEITY IN CIN PHENOTYPES

In this study, perturbation of the SCF complex was induced via three different mechanisms (*SKP1* silencing, *CUL1* silencing, and *SKP1* heterozygous knockout) and within three distinct cell lines (HCT116, FT194 and FT246). While each of these approaches reproducibly induced increases in CIN phenotypes, the type and severity of CIN phenotypes differed between approaches (*e.g. SKP1* silencing vs. *CUL1* silencing or *SKP1*$^{+/-}$ 1 vs. *SKP1*$^{+/-}$ 2). This section describes examples of various factors that may account for variability in CIN phenotypes in general, between *SKP1* and *CUL1*-silenced cells, and between the two FT246 *SKP1*$^{+/-}$ clones that were characterized in this thesis.

5.2.1. CIN is Heterogeneous but Non-Random.

An overly simplistic model of CIN may involve any number or combination of chromosomes being gained or lost completely at random. In this model, CIN-positive samples would theoretically exhibit an increase in both gains and losses of chromosomes, and complete heterogeneity in the distribution of chromosome numbers. However, even in a CIN-positive sample, karyotypic patterns are not completely random and certain chromosome complements may emerge more frequently than others[183–185]. As an example from the current study, chromosome

numbers following *SKP1* or *CUL1* silencing or within *SKP1*$^{+/-}$ clones appear to follow a bimodal distribution, with a population of mitotic chromosome spreads within the near diploid range and another population within the near tetraploid range, and very few mitotic spreads with chromosome complements between these two populations.

In general, there are several reasons why the random model of chromosome gains or losses may not be observed in practice. In some cases, the specific mechanism underlying CIN may only be conducive to certain classes of chromosomal changes. For example, mechanisms such as endoreduplication (repeated rounds of DNA synthesis in the absence of cell division) may underlie whole genome duplication and increases in ploidy, but would not be expected to cause other types of numerical changes such as chromosome losses[186]. Alternatively, the formation of micronuclei containing whole missegregated chromosomes and subsequent micronuclear rupture may represent a mechanism by which small numbers of chromosomes are lost but not gained[187,188].

In addition, certain chromosome complements may confer survival advantages or disadvantages, and cells harboring unfavorable chromosome complements may be lost from the population. For example, very few instances of large-scale chromosome losses were observed in the current study, with the exception of FT246 *SKP1*$^{+/-}$ 1, in which large-scale chromosome losses were observed at some, but not all timepoints in CIN timecourse experiments. The underrepresentation of large-scale chromosome losses within these samples (defined in this thesis as the loss of $\geq$ 10 chromosomes) may be due to the fact that cells containing small numbers of chromosomes are unlikely to be viable under normal conditions. Within *SKP1*$^{+/-}$ 1, an underlying mechanism may be driving large-scale chromosome losses, but the resulting chromosome complements may not be sustainable through multiple rounds of mitosis. Interestingly, a study by Ravichandran *et al.*[189] evaluated how yeast cells adapt to CIN over time, and showed that particular

karyotypes or specific chromosomal aneuploidies may provide an early growth or survival advantage but the chromosome complements that are considered "favorable" may change over time and in response to selective pressures within the environment. Overall, the authors concluded that the benefits of a particular aneuploid karyotype must outweigh the negative consequences such as gene dosage imbalances associated with whole chromosome copy number alterations or genetic interactions between specific aneuploid chromosomes[189]. Thus, even in the presence of CIN, certain chromosomal copy number changes may be more frequently observed within human cancers[184,190].

Beyond the selective advantages or disadvantages they confer, there may be additional biological factors leading to the preferential gain or loss of specific chromosomes over others. For example, Worrall *et al.*[185] showed that specific chromosomes are particularly vulnerable to drug-induced chromosome missegregation and described chromosomal features potentially underlying these biases, such as chromosome size or centromere size. Collectively, these examples demonstrate that even in the presence of CIN, there are biological restrictions on the type and severity of CIN phenotypes that may be observed, which may begin to explain why different CIN phenotypes were observed under different sets of conditions in the current study.

5.2.2. *SKP1* and *CUL1* Silencing Induce Different Levels of CIN.

In the current study, both *SKP1* and *CUL1* silencing induced increases in CIN phenotypes, which were generally more pronounced within the *SKP1*-silenced cells. This result held true across three cell lines (HCT116, FT194, FT246) and various CIN assays, especially the NA and MNF assays. This result was surprising, as SKP1 and CUL1 are components of the same complex and the mechanisms underlying CIN in each case would be predicted to be similar. While it is possible that these differences may stem from technical factors such as differences in gene silencing

efficiencies, semiquantitative western blot analyses following *SKP1* or *CUL1* silencing consistently show a comparable and strong reduction in both SKP1 and CUL1 levels (*i.e.* ≤ 10% of endogenous levels).

A second possibility is that SKP1 and/or CUL1 have additional cellular functions independent of the SCF complex. In fact, several studies have shown that SKP1 may interact with other binding partners beyond the conventional SCF complex components[191–194]. As described in Section 1.3., the SCF complex is part of a larger family of cullin-based E3 ubiquitin ligase complexes (*i.e.* CRLs). Beyond CUL1, there are 7 additional cullins (2, 3, 4A, 4B, 5, 7, or 9) that interact with distinct sets of adaptor proteins and substrate receptors to form distinct CRLs[195]. Due to the existence of multiple cullin proteins with similar binding motifs and functionality, there may be potential for functional compensation by another cullin in response to diminished *CUL1* expression. In fact, CUL7 has been shown to form an SCF-like complex containing SKP1 and RBX1[196], which could potentially mitigate the CIN phenotypes associated with loss of CUL1.

Finally, *SKP1* and *CUL1* silencing may have different impacts on the kinetics of SCF complex assembly or disassembly. A recent study showed that the cellular repertoire of SCF complexes is dynamic and the assembly of specific SCF complexes (*i.e.* containing one of 68 different F-box proteins) is dictated by substrate abundance[197]. Under normal conditions, the molar ratio of SKP1 to CUL1 is not 1:1 and in fact the total concentration of different substrate receptors (SKP1 with an associated F-box protein) greatly exceeds CUL1 concentration[198], therefore access to CUL1 is competitive. Thus, disrupting these stoichiometric ratios may alter the cellular repertoire of assembled SCF complexes and may account for the differences in phenotypic severity between *SKP1* and *CUL1* silencing. Overall, further studies investigating the functional differences between SKP1 and CUL1 including potential compensatory pathways are warranted.

5.2.3. *SKP1*$^{+/-}$ Clones 1 and 2 are Phenotypically Distinct.

SKP1$^{+/-}$ 1 exhibits mild CIN phenotypes that are predominantly small-scale and large-scale chromosome losses. It is also characterized by small nuclei, a low rate of MNF, and small cell bodies. Contrastingly, *SKP1*$^{+/-}$ 2 exhibits CIN phenotypes that are more similar in both type and severity to those observed within *SKP1*-silenced cells. More specifically, *SKP1*$^{+/-}$ 2 exhibits both gains and losses of chromosomes (including large-scale chromosome gains), heterogeneous NAs, increased MNF, and heterogeneous cell body sizes (some being extremely large). There are three important differences between the two clones that may account for the phenotypic differences observed: 1) *SKP1*$^{+/-}$ 2 expresses SKP1 at lower levels than *SKP1*$^{+/-}$ 1, which may explain the increased CIN severity within *SKP1*$^{+/-}$ 2 cells; 2) *SKP1*$^{+/-}$ 2 does not express wild-type SKP1, but rather a mutant SKP1 in which 2 proline residues are deleted which is predicted to adversely impact SKP1 structure and/or function; and 3) *SKP1*$^{+/-}$ 1 and *SKP1*$^{+/-}$ 2 appear to originate from distinct FT246 subclones pre-existing within the parental FT246 cell line (*i.e.* containing 44 or 46 chromosomes, respectively), suggesting distinct genetic backgrounds that may impact their susceptibility to gaining or losing chromosomes.

Beyond the differences between the two clones, the phenotypic differences observed may also suggest a different evolutionary trajectory during the clonal expansion process. Both clones began from a single cell harboring a defect in a putative CIN gene (*i.e.* heterozygous loss of *SKP1*). By definition, an increased rate of chromosome gains and losses would be expected to occur during the clonal expansion process, leading to karyotypic differences within and between each population/clone. It is conceivable that the two populations (*SKP1*$^{+/-}$ 1 and *SKP1*$^{+/-}$ 2) may have evolved in different ways depending on the chromosome complements existing during the early stages of clonal expansion and the impact these karyotypes had on cell survival. Overall, the

specific set of CIN phenotypes observed following diminished expression of SCF complex components may depend on the degree to which SCF complex function is perturbed and/or the specific substrates that are misregulated. In turn, these changes may confer survival advantages or disadvantages which shape the evolutionary trajectory of the population as a whole.

5.3 REQUIREMENTS FOR FT CELL TRANSFORMATION

In this study, heterozygous loss of *SKP1* in FT246 cells induced increases in CIN phenotypes which were sustained within the population over an extended period of time. However, the induction of CIN within two distinct *SKP1*$^{+/-}$ clones did not, by itself induce cellular transformation. One potential explanation for these findings is that while CIN may generate a level of karyotypic heterogeneity which "primes" cells to be transformed, it must be coupled with additional genetic or environmental factors which enable selection and outgrowth of a transformed subclone. Alternatively, while karyotypes are constantly evolving within a CIN-positive sample, it may require more time to accrue the specific set of genetic changes required for full cellular transformation.

It is widely accepted that *TP53* mutation is an important initial event that contributes to the development of HGSOC, but is not sufficient on its own to induce cellular transformation. *In vitro* models using immortalized FT cell lines provide insight into the additional genetic alterations that may cooperate with mutated *TP53* to induce FT cell transformation[43,50,170–172]. Ultimately, the set of genetic alterations that are considered "advantageous" and sufficient to induce cellular transformation are likely to depend upon the environment in which the cells are grown or cultured. Thus, understanding the *in vivo* fallopian tube microenvironment and incorporating key

microenvironmental conditions into experimental models (detailed further in Section 5.3.3) will be critical to elucidate the early etiological events driving oncogenesis.

5.3.1. *TP53* Mutations in HGSOC.

TP53 mutations are present in > 96% of HGSOCs[24,40,41] and can be detected within precursor lesions in the fallopian tube epithelium, suggesting it is an early event in HGSOC pathogenesis[14,42]. Across various cancer types, *TP53* mutations occur most often within exons 4-8 which encode the DNA-binding domain of the TP53 protein[199]. These alterations include missense, nonsense, or splice site mutations as well as indels affecting the *TP53* reading frame, and can result in different functional outcomes that are typically classified as either LOF (functional inactivation) or aberrant oncogenic GOF[41].

In the context of HGSOC, IHC can be used to detect altered TP53 expression and infer *TP53* mutational status within tissue samples derived from either the primary tumor or the fallopian tubes. TP53 LOF alterations manifest as complete absence of TP53 protein following IHC, while GOF alterations result in an abnormal accumulation of mutant TP53 within the nucleus[41]. In addition, some cases of abnormal cytoplasmic TP53 expression due to mutations affecting the TP53 nuclear localization signaling domain have been observed[41]. IHC is also used clinically to distinguish between high-grade and low-grade serous ovarian cancers, which are characterized by the presence or absence of *TP53* mutations, respectively[41,173,200]. In one study of primary tumor samples collected from 171 HGSOC patients, 169 samples (99%) were found to have *TP53* mutations, of which 66% were predicted to be GOF mutations and 33% were predicted to be LOF[41]. In this cohort, the most common single amino acid substitutions were R175H, Y220C, R273H, and R196X[41]. Importantly, *TP53* mutations are a requirement for FT cell transformation,

but studies within cell lines or genetically engineered mouse models suggest that they must be coupled with additional genetic alterations in order for cellular transformation to occur[9,43,50,170].

The two FT cell lines employed within this thesis are TP53-compromised due to either expression of the SV40 large T antigen in FT194 cells, which binds to and functionally inactivates TP53[201], or due to the expression of *TP53* shRNA in FT246 cells which was shown in this study to cause complete absence of TP53 expression. Thus, both of these models are expected to be functionally similar to the *TP53* LOF alterations that are commonly observed in HGSOC. However, it is important to note that GOF and LOF *TP53* mutations may have distinct impacts on tumor initiation, disease progression, or patient outcomes. Candeias *et al.*[202] showed that the oncogenic GOF associated with common *TP53* missense mutations stems from the production of short TP53 isoforms which confer enhanced survival, proliferation, invasion and adhesion. In genetically engineered mouse models of *TP53* mutations, GOF alterations exhibited increased tumorigenicity and metastasis relative to LOF alterations[203,204]. However, epidemiological studies in HGSOC patients have shown associations between TP53 LOF and reduced overall survival or increased disease recurrence[205,206]. These data suggest that the functional class of *TP53* alteration may have implications for tumor initiation and disease pathogenesis, which is an important consideration when investigating the requirements for FT cell transformation.

5.3.2. Current Models of FT Cell Transformation.

While several studies have previously induced transformation of immortalized FT cells via overexpression of various oncogenes[43,171,172], the current study is the first to evaluate the role CIN plays in FT cell transformation. Table 5-1 summarizes previous models in which immortalized FT cell lines were transformed via the introduction of one or more transgenic elements. One study by Karst *et al.*[50] showed that overexpression of Cyclin E1 within FT282 cells induced cellular

transformation-associated phenotypes including increases in cell proliferation rates, clonogenic growth, loss of contact inhibition, and mild increases in anchorage-independent growth (*i.e.* soft agar colony formation). However, *in vivo* tumorigenicity assays were not performed in this study, and the authors noted that the phenotypes were less aggressive relative to their earlier work using $HRAS^{G12V}$ or C-MYC to induce FT cell transformation[43]. Thus, the authors concluded that additional genetic events beyond Cyclin E1 amplification may be required for full transformation[50].

The work presented in this thesis builds upon the model of Karst *et al.*[50], showing that reduced degradation of Cyclin E1 stemming from diminished expression of SCF complex components is an additional mechanism by which Cyclin E1 can be overexpressed. The current study further shows that the induction of CIN may be the means by which Cyclin E1 overexpression induces its various phenotypic effects. However, increases in cellular transformation phenotypes were not observed within $SKP1^{+/-}$ FT246 cells. It is possible that the extent of Cyclin E1 overexpression within the current study was not equivalent to that induced by Karst *et al.*[50], or alternatively, that these differences may be due to the genetic background of the specific FT cell lines employed. As highlighted above, the FT194 and FT246 cell lines employed within this thesis are models of TP53 LOF, whereas the FT282 cell line employed by Karst *et al.*[50] expresses $TP53^{R175H}$, one of the most common point mutations affecting *TP53* in HGSOC[41] and other cancers[199,207] which has been shown to have GOF effects[208,209].

All four of the remaining studies presented in Table 5-1 demonstrate transformation of FT cells harboring TP53 LOF alterations including expression of the SV40 large T antigen, *TP53* shRNA, or dominant-negative TP53. Interestingly, Hua *et al.*[170] employed the same cell lines that are described in this thesis (FT194 and FT246). A key difference between these studies and the

Table 5-1. *In Vitro* Models of FT Cell Transformation.

Cell Line	Factors Required for Immortalization[A]	Factors Required for Transformation[B]	TP53 Functional Class[C]	Transformation Assay	Ref.
FT282	hTERT, $TP53^{R175H}$	Cyclin E1	GOF	Soft agar colony formation	50
FT33	hTERT, SV40 T, SV40 t	$HRAS^{G12V}$	LOF	Soft agar colony formation, *in vivo* tumorigenicity	43
		C-MYC			
	hTERT, *TP53*-shRNA, $CDK4^{R24C}$	C-MYC, *PPP2R5C*-shRNA	LOF		
FTEC74, FTEC76	hTERT, SV40 T, Cyclin D1, $CDK4^{R24C}$, *BRCA1*-shRNA, $HRAS^{G12V}$, $C\text{-}MYC^{T58A}$		LOF	Soft agar colony formation, *in vivo* tumorigenicity	172
Not named	hTERT, SV40 T	$HRAS^{G12V}$, $C\text{-}MYC^{T58A}$	LOF		
FT194	hTERT, SV40 T	YAP	LOF	Soft agar colony formation, *in vivo* tumorigenicity	170
		YAP^{S127A}			
FT246	hTERT, *TP53*-shRNA, $CDK4^{R24C}$	YAP	LOF	Soft agar colony formation	
		YAP^{S127A}			
Not named	hTERT, Cyclin D1, $CDK4^{R24C}$	$KRAS^{G12V}$, DN-TP53, Myr-AKT1	LOF	Soft agar colony formation, *in vivo* tumorigenicity	171
		$KRAS^{G12V}$, DN-TP53, C-MYC	LOF		

[A]Molecular alterations (*e.g.* shRNA or overexpressed protein) required for cell immortalization, but not sufficient for cellular transformation. SV40 T, SV40 large T antigen; SV40 t, SV40 small T antigen.

[B]Molecular alterations (*e.g.* shRNA or overexpressed protein) required for cellular transformation. DN-TP53, dominant-negative TP53; Myr-AKT1, myristoylated AKT1.

[C]Predicted impact of immortalization or transformation factors on TP53 function. GOF, gain of function; LOF, loss-of-function.

work presented in this thesis is the expected frequency of the "transforming event" within the overall population. In the four studies listed above, an exogenous oncogene was delivered to a population of cells via lentiviral transduction and was typically coupled with antibiotic selection to isolate the successfully transduced cells, resulting in a homogeneous population of cells harboring the transforming oncogene. In contrast, this thesis describes the derivation of a cell line harboring a defect in a CIN gene (*SKP1*), which is expected to result in a karyotypically heterogeneous population of cells in which the chromosome complement conferring increased tumorigenic potential may only be present in a minor fraction of the cellular population if present at all. Thus, when evaluating cellular transformation using assays such as the soft agar colony formation assay, the number of colonies formed (which is expected to reflect the number of cells in the population with anchorage-independent growth potential) may differ substantially between an "oncogene-induced" model of cellular transformation relative to a "CIN-induced" model. However, the karyotypic heterogeneity induced by CIN also confers great evolutionary and adaptive potential, and a single "transforming event" could become more prevalent within the population under certain selective pressures. Thus, in a CIN-positive sample, it may be particularly important to evaluate cellular transformation under the same selective pressures that would be present *in vivo*.

5.3.3. The Role of the Microenvironment in FT Cell Transformation.

The strongest non-genetic risk factor for EOC is the number of lifetime ovulatory events[210]. The concept of repetitive ovulatory cycles contributing to the pathogenesis of EOC, referred to as the "incessant ovulation hypothesis", was initially proposed by Fathalla in 1971 who noted that factors including the use of oral contraceptives or increased gravidity (number of pregnancies) were associated with reduced frequencies of EOC[211]. In addition, EOCs are rarely observed in

other mammals with a smaller number of lifetime ovulatory events such as those with seasonal ovulatory patterns[211]. In support of this hypothesis, many subsequent studies have established strong links between the use of oral contraceptives and a reduction in EOC risk[212–214]. These findings are thought to be linked to the role of inflammation in cancer pathogenesis. Ovulation is an acute local inflammatory event that results in the production and/or release of genotoxic substances such as reactive oxygen species (ROS)[215,216], inflammatory cytokines[217], and hormones[216,218] into the microenvironment surrounding the ovary and fallopian tube fimbriae. Many of these factors are found within the follicular fluid of the pre-ovulatory follicle, and several studies have shown that exposure of FT cells to follicular fluid or ROS induces DNA damage, changes in gene expression, and increased cell proliferation[219–223]. Interestingly, the use of nonsteroidal anti-inflammatory drugs such as aspirin have been associated with a reduced risk or improved prognosis in ovarian cancer[224–226]. Collectively, these data suggest that genotoxic stresses including proinflammatory factors and ROS may be an important part of the microenvironment contributing to the development of EOCs including HGSOC.

While it is unclear exactly how these environmental factors interact with established genetic factors to drive HGSOC development, some studies have been performed in the context of *BRCA1* mutations showing that gene expression profiles within luteal phase normal fallopian tube epithelium of *BRCA1* mutation carriers resemble the gene expression profiles found within HGSOC samples[227] and exhibit increased proinflammatory signaling[228]. Similarly, primary FT cells derived from *BRCA1* mutation carriers have increased and prolonged proinflammatory signaling following follicular fluid exposure[229]. In an analogous fashion, it would be interesting to evaluate the impact *SKP1* deficiency or CIN has on the cellular response to the ovulation-associated microenvironment (detailed further in Section 5.4.1.).

5.4. FUTURE EXPERIMENTAL DIRECTIONS

While CIN is traditionally thought to drive cancer initiation, this study suggests that an alteration in a CIN gene alone may not be sufficient to induce FT cell transformation. However, the time at which cellular transformation is assessed and the environmental forces acting on the cell population may be critical factors that determine whether or not CIN will lead to cellular transformation, and may be worth investigating in future experiments. In addition, while the work presented in this thesis focuses on the role of CIN at the early stages of HGSOC development, the cellular models generated in this thesis could also be employed to assess the role of CIN at later stages of disease including its role in drug resistance. Ultimately, a major goal of this research is to enable the design of improved therapeutics capable of exploiting CIN within HGSOC in order to improve patient outcomes.

5.4.1. Further Exploring the Role of CIN in Tumorigenesis

Conceptually, ongoing gains and losses of chromosomes may eventually enable the acquisition of a chromosome complement that is capable of driving tumorigenesis. However, to detect cellular transformation in practice may require: 1) sufficient time to accrue the series of genetic changes needed for transformation, and 2) an environment that enables survival and proliferation of a fully or partially transformed subclone. Thus, to further explore the role of CIN in tumorigenesis, future studies could focus on combining CIN with additional factors that further accelerate the rate at which chromosomes are gained or lost, or evaluating how CIN-positive samples adapt under alternative environmental conditions. For example, Section 5.3.3. describes how ovulation-associated genotoxic stresses within the fallopian tube microenvironment may be an important factor contributing to HGSOC initiation. These microenvironmental conditions could be modelled *in vitro* by treating cells with ionizing radiation or ROS-inducing drugs. To assess

whether or not these factors synergize with the pre-existing level of CIN within *SKP1*$^{+/-}$ cells to induce cellular transformation, standard CIN and cellular transformation assays could be performed as described in this thesis using both treated and untreated cells.

Importantly, many *in vitro* models of cellular transformation fail to translate to *in vivo* tumor formation, and conversely, many human tumors fail to grow under standard *in vitro* conditions (*e.g.* when attempting to establish cell lines from primary tumor samples). This suggests that there are very different selective pressures at play in each environment that are a barrier to fully understanding and modelling disease. Accordingly, ongoing research is focused on developing alternative *in vitro* models or systems that better recapitulate the *in vivo* environment. For example, Ince *et al.* developed an alternative cell culture medium that is able to support the growth of a greater diversity of primary ovarian tumors[230]. Other models focus on growing cells as part of a more complex 3D structure, such as "organoid" models of the fallopian tube epithelium that capture the normal tissue architecture[231]. In the future, these systems may provide an improved platform for assessing the role of CIN in FT cell transformation.

If evidence of cellular transformation is observed under the above conditions, these studies could then be adapted for *in vivo* tumorigenicity assays. These assays could be performed by injecting the experimental cell lines into an immunocompromised mouse (*e.g.* intraperitoneal injection) and monitoring the extent of tumor formation and dissemination, which would directly confirm whether or not diminished *SKP1* expression and/or CIN is capable of inducing tumorigenesis.

5.4.2. Drug Target Discovery

While the work presented in this thesis focuses on the role of CIN at the early stages of HGSOC development, another major goal of studying CIN within HGSOC is to understand the

role it may play in drug resistance and ultimately to enable the design of improved therapeutics for treating heterogeneous CIN-positive tumors. To move forward in this regard, experiments could be designed to assess how CIN-positive *SKP1*$^{+/-}$ cells behave under the selective pressure of chemotherapy. For example, *SKP1*$^{+/-}$ and control cells could be treated with standard chemotherapeutic agents (such as paclitaxel, carboplatin, and other agents used clinically to treat HGSOC) and the number of cells that survive treatment could be enumerated to determine whether *SKP1*$^{+/-}$ cells exhibit an increased EC_{50} (*i.e.* the concentration of drug required to cause a 50% reduction in cell numbers) relative to wild-type cells. To complement these findings, it will be important to evaluate the prevalence of CIN within larger HGSOC patient cohorts and to correlate CIN status to patient outcomes and/or response to treatment. Further, to determine whether diminished SKP1 or CUL1 expression is linked to poor overall prognosis, SKP1 or CUL1 protein expression levels could be evaluated via IHC within a tumor microarray and these data could be included in correlative studies.

If the studies above confirm that *SKP1* or *CUL1* are implicated in early disease development and/or cancer evolution (*e.g.* the acquisition of drug resistance), this knowledge could be used to identify novel drug targets that exploit the presence of CIN in HGSOC. For example, a synthetic lethal paradigm could be employed to exploit diminished expression of a specific CIN gene like *SKP1* or *CUL1*. Synthetic lethality refers to a rare and lethal combination of two independently viable gene mutations or deletions[54]. From a therapeutic perspective, downregulating a synthetic lethal interactor of an established CIN gene (*e.g.* via a small-molecule inhibitor that targets its protein product) would lead to selective killing of cancer cells with alterations in that specific CIN gene[54]. This approach is analogous to the use of poly(ADP-ribose) polymerase (PARP) inhibitors to treat ovarian cancers harboring *BRCA1/2* mutations[232–234].

Alternatively, understanding of the relevance of CIN in HGSOC may enable the use of other therapeutic approaches designed to exploit the presence of CIN in general[235]. For example, because extensive levels of CIN may not be compatible with cell viability, employing drugs that further exacerbate the pre-existing CIN has been proposed as a strategy to kill tumor cells[235–237]. Overall, this thesis represents a very early step towards uncovering the role of CIN in HGSOC pathogenesis, and there are many promising avenues for further research.

5.5. SIGNIFICANCE

CIN is just beginning to be characterized in HGSOC, and the potential mechanisms underlying CIN have never been studied in this context. The work presented in this thesis confirms that impaired protein turnover via disruption of the SCF complex is one mechanism capable of inducing CIN in HGSOC precursor cells. In general, understanding the causative mechanisms underlying CIN may have implications for the understanding of both early disease development as well as for disease evolution. These are two key areas that remain poorly understood in HGSOC, and intervention at these stages (*e.g.* early-stage disease detection or late-stage therapeutic intervention) is critical for improving patient outcomes. In addition, because *SKP1* and *CUL1* are somatically altered in numerous cancer types and CIN is pervasive across a variety of cancers, the findings of this study are expected to have widespread relevance beyond HGSOC.

CHAPTER 6. REFERENCES

1. Canadian Cancer Statistics Advisory Committee. Canadian Cancer Statistics 2019. (2019). Available at: cancer.ca/Canadian-Cancer-Statistics-2019-EN.
2. Torre, L. A. *et al.* Ovarian cancer statistics, 2018. *CA. Cancer J. Clin.* **68**, 284–296 (2018).
3. Reid, B. M., Permuth, J. B. & Sellers, T. A. Epidemiology of ovarian cancer: a review. *Cancer Biol. Med.* **14**, 9–32 (2017).
4. Bowtell, D. D. *et al.* Rethinking ovarian cancer II: reducing mortality from high-grade serous ovarian cancer. *Nat. Rev. Cancer* **15**, 668–679 (2015).
5. Cortez, A. J., Tudrej, P., Kujawa, K. A. & Lisowska, K. M. Advances in ovarian cancer therapy. *Cancer Chemother. Pharmacol.* **81**, 17–38 (2018).
6. Sherman-Baust, C. A., Becker, K. G., Wood Iii, W. H., Zhang, Y. & Morin, P. J. Gene expression and pathway analysis of ovarian cancer cells selected for resistance to cisplatin, paclitaxel, or doxorubicin. *J. Ovarian Res.* **4**, 21 (2011).
7. Prat, J. Ovarian carcinomas: five distinct diseases with different origins, genetic alterations, and clinicopathological features. *Virchows Arch.* **460**, 237–249 (2012).
8. Levanon, K., Crum, C. & Drapkin, R. New insights into the pathogenesis of serous ovarian cancer and its clinical impact. *J. Clin. Oncol.* **26**, 5284–5293 (2008).
9. Perets, R. *et al.* Transformation of the fallopian tube secretory epithelium leads to high-grade serous ovarian cancer in Brca;Tp53;Pten models. *Cancer Cell* **24**, 751–765 (2013).
10. Labidi-Galy, S. I. *et al.* High grade serous ovarian carcinomas originate in the fallopian tube. *Nat. Commun.* **8**, 1093 (2017).
11. Piek, J. M. *et al.* Dysplastic changes in prophylactically removed Fallopian tubes of women predisposed to developing ovarian cancer. *J. Pathol.* **195**, 451–456 (2001).
12. Crum, C. P. *et al.* The distal fallopian tube: a new model for pelvic serous carcinogenesis. *Curr. Opin. Obstet. Gynecol.* **19**, 3–9 (2007).
13. Kindelberger, D. W. *et al.* Intraepithelial carcinoma of the fimbria and pelvic serous carcinoma: Evidence for a causal relationship. *Am. J. Surg. Pathol.* **31**, 161–169 (2007).
14. Lee, Y. *et al.* A candidate precursor to serous carcinoma that originates in the distal fallopian tube. *J. Pathol.* **211**, 26–35 (2007).
15. Anglesio, M. S., Carey, M. S., Kobel, M., Mackay, H. & Huntsman, D. G. Clear cell carcinoma of the ovary: a report from the first Ovarian Clear Cell Symposium, June 24th, 2010. *Gynecol. Oncol.* **121**, 407–415 (2011).
16. Wiegand, K. C. *et al.* ARID1A mutations in endometriosis-associated ovarian carcinomas. *N. Engl. J. Med.* **363**, 1532–1543 (2010).
17. Prowse, A. H. *et al.* Molecular genetic evidence that endometriosis is a precursor of ovarian cancer. *Int. J. cancer* **119**, 556–562 (2006).
18. Seidman, J. D. & Khedmati, F. Exploring the histogenesis of ovarian mucinous and transitional cell (Brenner) neoplasms and their relationship with Walthard cell nests: a study of 120 tumors. *Arch. Pathol. Lab. Med.* **132**, 1753–1760 (2008).
19. Shih, I.-M. & Kurman, R. J. Ovarian tumorigenesis: a proposed model based on morphological and molecular genetic analysis. *Am. J. Pathol.* **164**, 1511–1518 (2004).
20. Kurman, R. J. & Shih, I.-M. The Dualistic Model of Ovarian Carcinogenesis: Revisited, Revised, and Expanded. *Am. J. Pathol.* **186**, 733–747 (2016).
21. Singer, G. *et al.* Mutations in BRAF and KRAS characterize the development of low-grade ovarian serous carcinoma. *J. Natl. Cancer Inst.* **95**, 484–486 (2003).

22. Obata, K. *et al.* Frequent PTEN/MMAC mutations in endometrioid but not serous or mucinous epithelial ovarian tumors. *Cancer Res.* **58**, 2095–2097 (1998).
23. Singer, G. *et al.* Patterns of p53 mutations separate ovarian serous borderline tumors and low- and high-grade carcinomas and provide support for a new model of ovarian carcinogenesis: a mutational analysis with immunohistochemical correlation. *Am. J. Surg. Pathol.* **29**, 218–224 (2005).
24. Cancer Genome Atlas Research Network. Integrated genomic analyses of ovarian carcinoma. *Nature* **474**, 609–615 (2011).
25. Gorringe, K. L. *et al.* Copy number analysis identifies novel interactions between genomic loci in ovarian cancer. *PLoS One* **5**, (2010).
26. Wang, Y. K. *et al.* Genomic consequences of aberrant DNA repair mechanisms stratify ovarian cancer histotypes. *Nat. Genet.* **49**, 856–865 (2017).
27. American Joint Committee on Cancer. Ovary, Fallopian Tube, and Primary Peritoneal Carcinoma. in *AJCC Cancer Staging Manual, 8th Ed.* 681–690 (Springer, 2017).
28. Prat, J. Staging classification for cancer of the ovary, fallopian tube, and peritoneum. *Int. J. Gynaecol. Obstet.* **124**, 1–5 (2014).
29. Ahmed, N. & Stenvers, K. L. Getting to know ovarian cancer ascites: opportunities for targeted therapy-based translational research. *Front. Oncol.* **3**, 256 (2013).
30. Tan, D. S. P., Agarwal, R. & Kaye, S. B. Mechanisms of transcoelomic metastasis in ovarian cancer. *Lancet. Oncol.* **7**, 925–934 (2006).
31. Carmignani, C. P., Sugarbaker, T. A., Bromley, C. M. & Sugarbaker, P. H. Intraperitoneal cancer dissemination: mechanisms of the patterns of spread. *Cancer Metastasis Rev.* **22**, 465–472 (2003).
32. Howlader, N. *et al. SEER Cancer Statistics Review, 1975-2006, National Cancer Institute*.
33. Coleman, R. L., Monk, B. J., Sood, A. K. & Herzog, T. J. Latest research and treatment of advanced-stage epithelial ovarian cancer. *Nat. Rev. Clin. Oncol.* **10**, 211–224 (2013).
34. Fowler, W. C. J. & Van Le, L. Gemcitabine as a single-agent treatment for ovarian cancer. *Gynecol. Oncol.* **90**, S21-3 (2003).
35. Lawrie, T. A., Bryant, A., Cameron, A., Gray, E. & Morrison, J. Pegylated liposomal doxorubicin for relapsed epithelial ovarian cancer. *Cochrane database Syst. Rev.* CD006910 (2013). doi:10.1002/14651858.CD006910.pub2
36. Herzog, T. J. Clinical experience with topotecan in relapsed ovarian cancer. *Gynecol. Oncol.* **90**, S3-7 (2003).
37. Lisio, M.-A., Fu, L., Goyeneche, A., Gao, Z.-H. & Telleria, C. High-Grade Serous Ovarian Cancer: Basic Sciences, Clinical and Therapeutic Standpoints. *Int. J. Mol. Sci.* **20**, (2019).
38. Goff, B. A., Mandel, L., Muntz, H. G. & Melancon, C. H. Ovarian carcinoma diagnosis. *Cancer* **89**, 2068–2075 (2000).
39. Friedman, G. D., Skilling, J. S., Udaltsova, N. V & Smith, L. H. Early symptoms of ovarian cancer: a case-control study without recall bias. *Fam. Pract.* **22**, 548–553 (2005).
40. Ahmed, A. A. *et al.* Driver mutations in TP53 are ubiquitous in high grade serous carcinoma of the ovary. *J. Pathol.* **221**, 49–56 (2010).
41. Kobel, M. *et al.* Optimized p53 immunohistochemistry is an accurate predictor of TP53 mutation in ovarian carcinoma. *J. Pathol. Clin. Res.* **2**, 247–258 (2016).
42. Kuhn, E. *et al.* TP53 mutations in serous tubal intraepithelial carcinoma and concurrent pelvic high-grade serous carcinoma--evidence supporting the clonal relationship of the two lesions. *J. Pathol.* **226**, 421–426 (2012).

43. Karst, A. M., Levanon, K. & Drapkin, R. Modeling high-grade serous ovarian carcinogenesis from the fallopian tube. *Proc. Natl. Acad. Sci. U. S. A.* **108**, 7547–7552 (2011).
44. Soong, T. R., Kolin, D. L., Teschan, N. J. & Crum, C. P. Back to the Future? The Fallopian Tube, Precursor Escape and a Dualistic Model of High-Grade Serous Carcinogenesis. *Cancers (Basel).* **10**, (2018).
45. Mukhopadhyay, A. *et al.* Development of a functional assay for homologous recombination status in primary cultures of epithelial ovarian tumor and correlation with sensitivity to poly(ADP-ribose) polymerase inhibitors. *Clin. Cancer Res.* **16**, 2344–2351 (2010).
46. Mukhopadhyay, A. *et al.* Clinicopathological features of homologous recombination-deficient epithelial ovarian cancers: sensitivity to PARP inhibitors, platinum, and survival. *Cancer Res.* **72**, 5675–5682 (2012).
47. Risch, H. A. *et al.* Population BRCA1 and BRCA2 mutation frequencies and cancer penetrances: a kin-cohort study in Ontario, Canada. *J. Natl. Cancer Inst.* **98**, 1694–1706 (2006).
48. King, M.-C., Marks, J. H. & Mandell, J. B. Breast and ovarian cancer risks due to inherited mutations in BRCA1 and BRCA2. *Science* **302**, 643–646 (2003).
49. Kauff, N. D. & Barakat, R. R. Risk-reducing salpingo-oophorectomy in patients with germline mutations in BRCA1 or BRCA2. *J. Clin. Oncol.* **25**, 2921–2927 (2007).
50. Karst, A. M. *et al.* Cyclin E1 deregulation occurs early in secretory cell transformation to promote formation of fallopian tube-derived high-grade serous ovarian cancers. *Cancer Res.* **74**, 1141–1152 (2014).
51. Patch, A.-M. *et al.* Whole-genome characterization of chemoresistant ovarian cancer. *Nature* **521**, 489–494 (2015).
52. Ciriello, G., Cerami, E., Sander, C. & Schultz, N. Mutual exclusivity analysis identifies oncogenic network modules. *Genome Res.* **22**, 398–406 (2012).
53. Etemadmoghadam, D. *et al.* Synthetic lethality between CCNE1 amplification and loss of BRCA1. *Proc. Natl. Acad. Sci. U. S. A.* **110**, 19489–19494 (2013).
54. Sajesh, B., Guppy, B. & McManus, K. Synthetic Genetic Targeting of Genome Instability in Cancer. *Cancers (Basel).* **5**, 739–761 (2013).
55. Etemadmoghadam, D. *et al.* Integrated genome-wide DNA copy number and expression analysis identifies distinct mechanisms of primary chemoresistance in ovarian carcinomas. *Clin. Cancer Res.* **15**, 1417–1427 (2009).
56. Mayr, D. *et al.* Analysis of gene amplification and prognostic markers in ovarian cancer using comparative genomic hybridization for microarrays and immunohistochemical analysis for tissue microarrays. *Am. J. Clin. Pathol.* **126**, 101–109 (2006).
57. Hanahan, D. & Weinberg, R. A. Hallmarks of cancer: the next generation. *Cell* **144**, 646–74 (2011).
58. Geigl, J. B., Obenauf, A. C., Schwarzbraun, T. & Speicher, M. R. Defining 'chromosomal instability'. *Trends Genet.* **24**, 64–69 (2008).
59. Negrini, S., Gorgoulis, V. G. & Halazonetis, T. D. Genomic instability — an evolving hallmark of cancer. **11**, 220–228 (2010).
60. Nojadeh, J. N., Behrouz Sharif, S. & Sakhinia, E. Microsatellite instability in colorectal cancer. *EXCLI J.* **17**, 159–168 (2018).
61. Nazemalhosseini Mojarad, E., Kuppen, P. J., Aghdaei, H. A. & Zali, M. R. The CpG island methylator phenotype (CIMP) in colorectal cancer. *Gastroenterol. Hepatol. from bed to*

bench **6**, 120–128 (2013).
62. Cahill, D. P., Kinzler, K. W., Vogelstein, B. & Lengauer, C. Genetic instability and darwinian selection in tumours. *Trends Cell Biol.* **9**, M57-60 (1999).
63. Levine, M. S. & Holland, A. J. The impact of mitotic errors on cell proliferation and tumorigenesis. *Genes Dev.* **32**, 620–638 (2018).
64. Pavelka, N., Rancati, G. & Li, R. Dr Jekyll and Mr Hyde: role of aneuploidy in cellular adaptation and cancer. *Curr. Opin. Cell Biol.* **22**, 809–815 (2010).
65. Michor, F., Iwasa, Y., Vogelstein, B., Lengauer, C. & Nowak, M. A. Can chromosomal instability initiate tumorigenesis? *Semin. Cancer Biol.* **15**, 43–49 (2005).
66. Duesberg, P., Stindl, R. & Hehlmann, R. Origin of multidrug resistance in cells with and without multidrug resistance genes: chromosome reassortments catalyzed by aneuploidy. *Proc. Natl. Acad. Sci. U. S. A.* **98**, 11283–11288 (2001).
67. Gao, C. *et al.* Chromosome instability, chromosome transcriptome, and clonal evolution of tumor cell populations. *Proc. Natl. Acad. Sci. U. S. A.* **104**, 8995–9000 (2007).
68. Sansregret, L., Vanhaesebroeck, B. & Swanton, C. Determinants and clinical implications of chromosomal instability in cancer. *Nat. Rev. Clin. Oncol.* **15**, 139–150 (2018).
69. Burrell, R. A. *et al.* Replication stress links structural and numerical cancer chromosomal instability. *Nature* **494**, 492–496 (2013).
70. Bayani, J. *et al.* Genomic mechanisms and measurement of structural and numerical instability in cancer cells. *Semin. Cancer Biol.* **17**, 5–18 (2007).
71. Lee, A. J. X. *et al.* Chromosomal instability confers intrinsic multidrug resistance. *Cancer Res.* **71**, 1858–1870 (2011).
72. Gerlinger, M. & Swanton, C. How Darwinian models inform therapeutic failure initiated by clonal heterogeneity in cancer medicine. *Br. J. Cancer* **103**, 1139–1143 (2010).
73. Carter, S. L., Eklund, A. C., Kohane, I. S., Harris, L. N. & Szallasi, Z. A signature of chromosomal instability inferred from gene expression profiles predicts clinical outcome in multiple human cancers. *Nat. Genet.* **38**, 1043–1048 (2006).
74. Heng, H. H. *et al.* Chromosomal instability (CIN): What it is and why it is crucial to cancer evolution. *Cancer Metastasis Rev.* **32**, 325–340 (2013).
75. Jamal-Hanjani, M. *et al.* Extreme chromosomal instability forecasts improved outcome in ER-negative breast cancer: a prospective validation cohort study from the TACT trial. *Ann. Oncol.* 1–7 (2015). doi:10.1093/annonc/mdv178
76. Birkbak, N. J. *et al.* Paradoxical relationship between chromosomal instability and survival outcome in cancer. *Cancer Res.* **71**, 3447–3452 (2011).
77. Giam, M. & Rancati, G. Aneuploidy and chromosomal instability in cancer: a jackpot to chaos. *Cell Div.* **10**, 3 (2015).
78. McGranahan, N., Burrell, R. A., Endesfelder, D., Novelli, M. R. & Swanton, C. Cancer chromosomal instability: therapeutic and diagnostic challenges. *EMBO Rep.* **13**, 528–538 (2012).
79. Dong, A., Lu, Y. & Lu, B. Genomic/Epigenomic Alterations in Ovarian Carcinoma: Translational Insight into Clinical Practice. *J. Cancer* **7**, 1441–1451 (2016).
80. Kuo, K.-T. *et al.* Analysis of DNA copy number alterations in ovarian serous tumors identifies new molecular genetic changes in low-grade and high-grade carcinomas. *Cancer Res.* **69**, 4036–4042 (2009).
81. Wiedemeyer, W. R., Beach, J. A. & Karlan, B. Y. Reversing Platinum Resistance in High-Grade Serous Ovarian Carcinoma: Targeting BRCA and the Homologous Recombination

System. *Front. Oncol.* **4**, 34 (2014).
82. Eckert, M. A. *et al.* Genomics of Ovarian Cancer Progression Reveals Diverse Metastatic Trajectories Including Intraepithelial Metastasis to the Fallopian Tube. *Cancer Discov.* **6**, 1342–1351 (2016).
83. Penner-Goeke, S. *et al.* The temporal dynamics of chromosome instability in ovarian cancer cell lines and primary patient samples. *PLoS Genet.* **13**, 1–24 (2017).
84. Kuhn, E. *et al.* CCNE1 amplification and centrosome number abnormality in serous tubal intraepithelial carcinoma: further evidence supporting its role as a precursor of ovarian high-grade serous carcinoma. *Mod. Pathol. an Off. J. United States Can. Acad. Pathol. Inc* **29**, 1254–1261 (2016).
85. Dulic, V., Lees, E. & Reed, S. I. Association of human cyclin E with a periodic G1-S phase protein kinase. *Science* **257**, 1958–1961 (1992).
86. Siu, K. T., Rosner, M. R. & Minella, A. C. An integrated view of cyclin E function and regulation. *Cell Cycle* **11**, 57–64 (2012).
87. Caldon, C. E. & Musgrove, E. A. Distinct and redundant functions of cyclin E1 and cyclin E2 in development and cancer. *Cell Div.* **5**, 2 (2010).
88. Chen, Z., Indjeian, V. B., McManus, M., Wang, L. & Dynlacht, B. D. CP110, a cell cycle-dependent CDK substrate, regulates centrosome duplication in human cells. *Dev. Cell* **3**, 339–350 (2002).
89. Singer, J. D., Gurian-West, M., Clurman, B. & Roberts, J. M. Cullin-3 targets cyclin E for ubiquitination and controls S phase in mammalian cells. *Genes Dev.* **13**, 2375–2387 (1999).
90. Spruck, C. H., Won, K. A. & Reed, S. I. Deregulated cyclin E induces chromosome instability. *Nature* **401**, 297–300 (1999).
91. Rajagopalan, H. *et al.* Inactivation of hCDC4 can cause chromosomal instability. *Nature* **428**, 77 (2004).
92. Fukasawa, K. Centrosome amplification, chromosome instability and cancer development. *Cancer Lett.* **230**, 6–19 (2005).
93. Bester, A. C. *et al.* Nucleotide deficiency promotes genomic instability in early stages of cancer development. *Cell* **145**, 435–446 (2011).
94. Jones, R. M. *et al.* Increased replication initiation and conflicts with transcription underlie Cyclin E-induced replication stress. *Oncogene* **32**, 3744–3753 (2013).
95. Takada, M. *et al.* FBW7 Loss Promotes Chromosomal Instability and Tumorigenesis via Cyclin E1/CDK2-Mediated Phosphorylation of CENP-A. *Cancer Res.* **77**, 4881–4893 (2017).
96. Kroeger, P. T. J. & Drapkin, R. Pathogenesis and heterogeneity of ovarian cancer. *Curr. Opin. Obstet. Gynecol.* **29**, 26–34 (2017).
97. Nakayama, N. *et al.* Gene amplification CCNE1 is related to poor survival and potential therapeutic target in ovarian cancer. *Cancer* **116**, 2621–2634 (2010).
98. Farley, J. *et al.* Cyclin E expression is a significant predictor of survival in advanced, suboptimally debulked ovarian epithelial cancers: a Gynecologic Oncology Group study. *Cancer Res.* **63**, 1235–1241 (2003).
99. Kleiger, G. & Mayor, T. Perilous journey: a tour of the ubiquitin-proteasome system. *Trends Cell Biol.* **24**, 352–359 (2014).
100. Thrower, J. S., Hoffman, L., Rechsteiner, M. & Pickart, C. M. Recognition of the polyubiquitin proteolytic signal. *EMBO J.* **19**, 94–102 (2000).
101. Deshaies, R. J. & Joazeiro, C. A. P. RING domain E3 ubiquitin ligases. *Annu. Rev. Biochem.*

78, 399–434 (2009).
102. Willems, A. R., Schwab, M. & Tyers, M. A hitchhiker's guide to the cullin ubiquitin ligases: SCF and its kin. *Biochim. Biophys. Acta* **1695**, 133–170 (2004).
103. Jin, J. *et al.* Systematic analysis and nomenclature of mammalian F-box proteins. *Genes & development* **18**, 2573–2580 (2004).
104. Stelzer, G. *et al.* The GeneCards Suite: From Gene Data Mining to Disease Genome Sequence Analyses. *Curr. Protoc. Bioinforma.* **54**, 1.30.1-1.30.33 (2016).
105. Schulman, B. A. *et al.* Insights into SCF ubiquitin ligases from the structure of the Skp1-Skp2 complex. *Nature* **408**, 381–386 (2000).
106. Cancer Genome Atlas Research Network. Comprehensive molecular portraits of human breast tumours. *Nature* **490**, 61–70 (2012).
107. Cancer Genome Atlas Research Network. Comprehensive molecular characterization of human colon and rectal cancer. *Nature* **487**, 330–337 (2012).
108. Cancer Genome Atlas Research Network. Comprehensive molecular profiling of lung adenocarcinoma. *Nature* **511**, 543–550 (2014).
109. Cancer Genome Atlas Research Network. Comprehensive molecular characterization of gastric adenocarcinoma. *Nature* **513**, 202–209 (2014).
110. Murphy, T. D. Drosophila skpA, a component of SCF ubiquitin ligases, regulates centrosome duplication independently of cyclin E accumulation. *J. Cell Sci.* **116**, 2321–2332 (2003).
111. Connelly, C. & Hieter, P. Budding yeast SKP1 encodes an evolutionarily conserved kinetochore protein required for cell cycle progression. *Cell* **86**, 275–285 (1996).
112. Nayak, S. *et al.* The Caenorhabditis elegans Skp1-related gene family: diverse functions in cell proliferation, morphogenesis, and meiosis. *Curr. Biol.* **12**, 277–287 (2002).
113. American Cancer Society. *Cancer Facts & Figures 2019*. (2019).
114. Yamanaka, A. *et al.* Multiple Skp1-related proteins in Caenorhabditis elegans: diverse patterns of interaction with Cullins and F-box proteins. *Curr. Biol.* **12**, 267–275 (2002).
115. Piva, R. *et al.* In vivo interference with Skp1 function leads to genetic instability and neoplastic transformation. *Mol. Cell. Biol.* **22**, 8375–8387 (2002).
116. Sarikas, A., Hartmann, T. & Pan, Z.-Q. The cullin protein family. *Genome Biol.* **12**, 220 (2011).
117. Gong, L. & Yeh, E. T. Identification of the activating and conjugating enzymes of the NEDD8 conjugation pathway. *J. Biol. Chem.* **274**, 12036–12042 (1999).
118. Kawakami, T. *et al.* NEDD8 recruits E2-ubiquitin to SCF E3 ligase. *EMBO J.* **20**, 4003–4012 (2001).
119. Duda, D. M. *et al.* Structural insights into NEDD8 activation of cullin-RING ligases: conformational control of conjugation. *Cell* **134**, 995–1006 (2008).
120. Dealy, M. J. *et al.* Loss of Cul1 results in early embryonic lethality and dysregulation of cyclin E. *Nat. Genet.* **23**, 245–248 (1999).
121. Wang, Y. *et al.* Deletion of the Cul1 gene in mice causes arrest in early embryogenesis and accumulation of cyclin E. *Curr. Biol.* **9**, 1191–1194 (1999).
122. Kipreos, E. T., Lander, L. E., Wing, J. P., He, W. W. & Hedgecock, E. M. cul-1 is required for cell cycle exit in C. elegans and identifies a novel gene family. *Cell* **85**, 829–839 (1996).
123. Shen, W.-H. *et al.* Null mutation of AtCUL1 causes arrest in early embryogenesis in Arabidopsis. *Mol. Biol. Cell* **13**, 1916–1928 (2002).
124. McManus, K. J., Barrett, I. J., Nouhi, Y. & Hieter, P. Specific synthetic lethal killing of

RAD54B-deficient human colorectal cancer cells by FEN1 silencing. *Proc. Natl. Acad. Sci. U. S. A.* **106**, 3276–3281 (2009).
125. Lentini, L., Amato, A., Schillaci, T. & Di Leonardo, A. Simultaneous Aurora-A/STK15 overexpression and centrosome amplification induce chromosomal instability in tumour cells with a MIN phenotype. *BMC Cancer* **7**, 212 (2007).
126. Cheng, X., Shen, Z., Yang, J., Lu, S.-H. & Cui, Y. ECRG2 disruption leads to centrosome amplification and spindle checkpoint defects contributing chromosome instability. *J. Biol. Chem.* **283**, 5888–5898 (2008).
127. Bakhoum, S. F., Genovese, G. & Compton, D. A. Deviant kinetochore-microtubule dynamics underlie chromosomal instability. *Curr. Biol.* **19**, 1937–1942 (2009).
128. Green, R. A. & Kaplan, K. B. Chromosome instability in colorectal tumor cells is associated with defects in microtubule plus-end attachments caused by a dominant mutation in APC. *J. Cell Biol.* **163**, 949–961 (2003).
129. Sajesh, B. V., Lichtensztejn, Z. & McManus, K. J. Sister chromatid cohesion defects are associated with chromosome instability in Hodgkin lymphoma cells. *BMC Cancer* **13**, 1 (2013).
130. Barber, T. D. *et al.* Chromatid cohesion defects may underlie chromosome instability in human colorectal cancers. *Proc Natl Acad Sci U S A* **105**, 3443–3448 (2008).
131. Wirth, K. G. *et al.* Separase: a universal trigger for sister chromatid disjunction but not chromosome cycle progression. *J. Cell Biol.* **172**, 847–860 (2006).
132. Jallepalli, P. V & Lengauer, C. Chromosome segregation and cancer: cutting through the mystery. *Nat. Rev. Cancer* **1**, 109–117 (2001).
133. Hutchins, J. R. a *et al.* Systematic Characterization of Human Protein Complexes Identifies Chromosome Segregation Proteins. *Science (80-.).* **328**, 593–599 (2010).
134. Lee, S., Ahn, Y., Kim, J., Cho, Y. & Park, J. Downregulation of NOP53 Ribosome Biogenesis Factor Leads to Abnormal Nuclear Division and Chromosomal Instability in Human Cervical Cancer Cells. (2018).
135. Cahill, D. P. *et al.* Mutations of mitotic checkpoint genes in human cancers. *Nature* **392**, 300–303 (1998).
136. Tutaj, H., Pogoda, E., Tomala, K. & Korona, R. Gene overexpression screen for chromosome instability in yeast primarily identifies cell cycle progression genes. *Curr. Genet.* **0**, 0 (2018).
137. Stirling, P. C. *et al.* The Complete Spectrum of Yeast Chromosome Instability Genes Identifies Candidate CIN Cancer Genes and Functional Roles for ASTRA Complex Components. **7**, 9–13 (2011).
138. Nakayama, K. *et al.* Targeted disruption of Skp2 results in accumulation of cyclin E and p27(Kip1), polyploidy and centrosome overduplication. *EMBO J.* **19**, 2069–2081 (2000).
139. Koepp, D. M. *et al.* Phosphorylation-dependent ubiquitination of cyclin E by the SCFFbw7 ubiquitin ligase. *Science* **294**, 173–177 (2001).
140. Lu, Y. *et al.* The F-box protein FBXO44 mediates BRCA1 ubiquitination and degradation. *J. Biol. Chem.* **287**, 41014–41022 (2012).
141. Moro, L., Arbini, A. A., Marra, E. & Greco, M. Up-regulation of Skp2 after prostate cancer cell adhesion to basement membranes results in BRCA2 degradation and cell proliferation. *J. Biol. Chem.* **281**, 22100–22107 (2006).
142. Kee, Y., Kim, J. M. & D'Andrea, A. D. Regulated degradation of FANCM in the Fanconi anemia pathway during mitosis. *Genes Dev.* **23**, 555–560 (2009).

143. Vaites, L. P. *et al.* The Fbx4 tumor suppressor regulates cyclin D1 accumulation and prevents neoplastic transformation. *Mol. Cell. Biol.* **31**, 4513–4523 (2011).
144. Kanie, T. *et al.* Genetic reevaluation of the role of F-box proteins in cyclin D1 degradation. *Mol. Cell. Biol.* **32**, 590–605 (2012).
145. Yu, Z. K., Gervais, J. L. & Zhang, H. Human CUL-1 associates with the SKP1/SKP2 complex and regulates p21(CIP1/WAF1) and cyclin D proteins. *Proc. Natl. Acad. Sci. U. S. A.* **95**, 11324–11329 (1998).
146. Coon, T. A., Glasser, J. R., Mallampalli, R. K. & Chen, B. B. Novel E3 ligase component FBXL7 ubiquitinates and degrades Aurora A, causing mitotic arrest. *Cell Cycle* **11**, 721–729 (2012).
147. Chen, B. B., Glasser, J. R., Coon, T. A. & Mallampalli, R. K. Skp-cullin-F box E3 ligase component FBXL2 ubiquitinates Aurora B to inhibit tumorigenesis. *Cell Death Dis.* **4**, e759 (2013).
148. Gonzalez-Loyola, A. *et al.* Aurora B Overexpression Causes Aneuploidy and p21Cip1 Repression during Tumor Development. *Mol. Cell. Biol.* **35**, 3566–3578 (2015).
149. Song, M. S. *et al.* Skp2 regulates the antiproliferative function of the tumor suppressor RASSF1A via ubiquitin-mediated degradation at the G1-S transition. *Oncogene* **27**, 3176–3185 (2008).
150. Wang, Z., Liu, P., Inuzuka, H. & Wei, W. Roles of F-box proteins in cancer. *Nat. Rev. Cancer* **14**, 233–247 (2014).
151. Randle, S. J. & Laman, H. F-box protein interactions with the hallmark pathways in cancer. *Semin. Cancer Biol.* **36**, 3–17 (2016).
152. Silverman, J. S., Skaar, J. R. & Pagano, M. SCF ubiquitin ligases in the maintenance of genome stability. *Trends Biochem. Sci.* **37**, 66–73 (2012).
153. Markossian, S., Arnaoutov, A., Saba, N. S., Larionov, V. & Dasso, M. Quantitative assessment of chromosome instability induced through chemical disruption of mitotic progression. *Cell Cycle* **15**, 1706–1714 (2016).
154. Nielsen, K., Petersen, S. & Orntoft, T. A comparison between stereological estimates of mean nuclear volume and DNA flow cytometry in bladder tumours. *APMIS* **97**, 949–56 (1989).
155. Capo-chichi, C. D. *et al.* Nuclear envelope structural defects cause chromosomal numerical instability and aneuploidy in ovarian cancer. *BMC Med.* **9**, 28 (2011).
156. Capo-chichi, C. D., Cai, K. Q., Testa, J. R., Godwin, A. K. & Xu, X.-X. Loss of GATA6 Leads to Nuclear Deformation and Aneuploidy in Ovarian Cancer. *Mol. Cell. Biol.* **29**, 4766–4777 (2009).
157. McManus, K. J. & Thompson, L. L. A novel multiplexed, image-based approach to detect phenotypes that underlie chromosome instability in human cells. *PLoS One* **10**, 1–17 (2015).
158. Bhatia, A. & Kumar, Y. Relevance of Microscopic Indicators of Chromosomal Instability in Routine Reporting of Malignancies. *Diagn. Cytopathol.* **42**, 181–188 (2013).
159. Fenech, M. Cytokinesis-block micronucleus assay evolves into a 'cytome' assay of chromosomal instability, mitotic dysfunction and cell death. *Mutat. Res. - Fundam. Mol. Mech. Mutagen.* **600**, 58–66 (2006).
160. Petersen, I. *et al.* Core classification of lung cancer: correlating nuclear size and mitoses with ploidy and clinicopathological parameters. *Lung Cancer* **65**, 312–318 (2009).
161. Zeimet, A. *et al.* DNA ploidy, nuclear size, proliferation index and DNA-hypomethylation in ovarian cancer. *Gynecol. Oncol.* **121**, 24–31 (2011).

162. Podgornova, M., Dubova, E. & Shchyogolev, A. Comparative characteristics of nuclear ploidy of cells in endocrine and solid pseudopapillary tumors of the pancreas. *Bull. Exp. Biol. Med.* **148**, 643–645 (2009).
163. Fenech, M. Chromosomal biomarkers of genomic instability relevant to cancer. **7**, 1128–1137 (2002).
164. Bhatia, A. & Kumar, Y. Cancer Cell Micronucleus: An Update On Clinical And Diagnostic Applications. *Apmis* **121**, 569–581 (2013).
165. Hanahan, D. & Weinberg, R. A. The hallmarks of cancer. *Cell* **100**, 57–70 (2000).
166. Steinberg, P. In Vitro-In Vivo Carcinogenicity. *Adv. Biochem. Eng. Biotechnol.* **157**, 81–96 (2017).
167. Borowicz, S. *et al.* The soft agar colony formation assay. *J. Vis. Exp.* e51998 (2014). doi:10.3791/51998
168. Frisch, S. M. & Francis, H. Disruption of epithelial cell-matrix interactions induces apoptosis. *J. Cell Biol.* **124**, 619–626 (1994).
169. Karst, A. M. & Drapkin, R. Primary culture and immortalization of human fallopian tube secretory epithelial cells. *Nat. Protoc.* **7**, 1755–1764 (2012).
170. Hua, G. *et al.* YAP induces high-grade serous carcinoma in fallopian tube secretory epithelial cells. *Oncogene* **35**, 2247–2265 (2016).
171. Nakamura, K. *et al.* Reconstitution of high-grade serous ovarian carcinoma from primary fallopian tube secretory epithelial cells. *Oncotarget* **9**, 12609–12619 (2018).
172. Jazaeri, A. A. *et al.* Molecular requirements for transformation of fallopian tube epithelial cells into serous carcinoma. *Neoplasia* **13**, 899–911 (2011).
173. Kobel, M. *et al.* Differences in tumor type in low-stage versus high-stage ovarian carcinomas. *Int. J. Gynecol. Pathol.* **29**, 203–211 (2010).
174. Nowak, M. A. *et al.* The role of chromosomal instability in tumor initiation. *Proc. Natl. Acad. Sci. U. S. A.* **99**, 16226–16231 (2002).
175. Nakayama, K. *et al.* Amplicon profiles in ovarian serous carcinomas. *Int. J. cancer* **120**, 2613–2617 (2007).
176. Nagy, E. & Maquat, L. E. A rule for termination-codon position within intron-containing genes: when nonsense affects RNA abundance. *Trends Biochem. Sci.* **23**, 198–199 (1998).
177. Popp, M. W. & Maquat, L. E. Leveraging Rules of Nonsense-Mediated mRNA Decay for Genome Engineering and Personalized Medicine. *Cell* **165**, 1319–1322 (2016).
178. Cao, F. *et al.* Comparison of gene-transfer efficiency in human embryonic stem cells. *Mol. imaging Biol.* **12**, 15–24 (2010).
179. Bowen, N. J. *et al.* Emerging roles for PAX8 in ovarian cancer and endosalpingeal development. *Gynecol. Oncol.* **104**, 331–337 (2007).
180. Laury, A. R. *et al.* A comprehensive analysis of PAX8 expression in human epithelial tumors. *Am. J. Surg. Pathol.* **35**, 816–826 (2011).
181. Mullany, L. K. *et al.* Specific TP53 Mutants Overrepresented in Ovarian Cancer Impact CNV, TP53 Activity, Responses to Nutlin-3a, and Cell Survival. *Neoplasia* **17**, 789–803 (2015).
182. Warne, D. J., Baker, R. E. & Simpson, M. J. Optimal Quantification of Contact Inhibition in Cell Populations. *Biophys. J.* **113**, 1920–1924 (2017).
183. Nicholson, J. M. & Cimini, D. Cancer karyotypes: survival of the fittest. *Front. Oncol.* **3**, 148 (2013).
184. Davoli, T. *et al.* Cumulative haploinsufficiency and triplosensitivity drive aneuploidy

patterns and shape the cancer genome. *Cell* **155**, 948–962 (2013).
185. Worrall, J. T. *et al.* Non-random Mis-segregation of Human Chromosomes. *Cell Rep.* **23**, 3366–3380 (2018).
186. Wang, X. *et al.* Genomic instability and endoreduplication triggered by RAD17 deletion. *Genes Dev.* **17**, 965–970 (2003).
187. Bakhoum, S. F. *et al.* Chromosomal instability drives metastasis through a cytosolic DNA response. *Nature* **553**, 467 (2018).
188. Hatch, E. M. Catastrophic nuclear envelope collapse in cancer cell micronuclei. **154**, 47–60 (2013).
189. Ravichandran, M. C., Fink, S., Clarke, M. N., Hofer, F. C. & Campbell, C. S. Genetic interactions between specific chromosome copy number alterations dictate complex aneuploidy patterns. *Genes Dev.* **32**, 1485–1498 (2018).
190. Duijf, P. H. G., Schultz, N. & Benezra, R. Cancer cells preferentially lose small chromosomes. *Int. J. cancer* **132**, 2316–2326 (2013).
191. Matsuzawa, S. I. & Reed, J. C. Siah-1, SIP, and Ebi collaborate in a novel pathway for beta-catenin degradation linked to p53 responses. *Mol. Cell* **7**, 915–926 (2001).
192. Galan, J. M. *et al.* Skp1p and the F-box protein Rcy1p form a non-SCF complex involved in recycling of the SNARE Snc1p in yeast. *Mol. Cell. Biol.* **21**, 3105–3117 (2001).
193. Seol, J. H., Shevchenko, A., Shevchenko, A. & Deshaies, R. J. Skp1 forms multiple protein complexes, including RAVE, a regulator of V-ATPase assembly. *Nat. Cell Biol.* **3**, 384–391 (2001).
194. Xu, M. *et al.* Atypical ubiquitin E3 ligase complex Skp1-Pam-Fbxo45 controls the core epithelial-to-mesenchymal transition-inducing transcription factors. *Oncotarget* **6**, 979–994 (2015).
195. Petroski, M. D. & Deshaies, R. J. Function and regulation of cullin-RING ubiquitin ligases. *Nat. Rev. Mol. Cell Biol.* **6**, 9–20 (2005).
196. Dias, D. C., Dolios, G., Wang, R. & Pan, Z.-Q. CUL7: A DOC domain-containing cullin selectively binds Skp1.Fbx29 to form an SCF-like complex. *Proc. Natl. Acad. Sci.* **99**, 16601–16606 (2002).
197. Reitsma, J. M. *et al.* Composition and Regulation of the Cellular Repertoire of SCF Ubiquitin Ligases. *Cell* **171**, 1326-1339.e14 (2017).
198. Bennett, E. J., Rush, J., Gygi, S. P. & Harper, J. W. Dynamics of cullin-RING ubiquitin ligase network revealed by systematic quantitative proteomics. *Cell* **143**, 951–965 (2010).
199. Donehower, L. A. *et al.* Integrated Analysis of TP53 Gene and Pathway Alterations in The Cancer Genome Atlas. *Cell Rep.* **28**, 1370-1384.e5 (2019).
200. Altman, A. D. *et al.* The diagnostic utility of TP53 and CDKN2A to distinguish ovarian high-grade serous carcinoma from low-grade serous ovarian tumors. *Mod. Pathol. an Off. J. United States Can. Acad. Pathol. Inc* **26**, 1255–1263 (2013).
201. Ali, S. H. & DeCaprio, J. A. Cellular transformation by SV40 large T antigen: interaction with host proteins. *Semin. Cancer Biol.* **11**, 15–23 (2001).
202. Candeias, M. M., Hagiwara, M. & Matsuda, M. Cancer-specific mutations in p53 induce the translation of Delta160p53 promoting tumorigenesis. *EMBO Rep.* **17**, 1542–1551 (2016).
203. Olive, K. P. *et al.* Mutant p53 gain of function in two mouse models of Li-Fraumeni syndrome. *Cell* **119**, 847–860 (2004).
204. Lang, G. A. *et al.* Gain of Function of a p53 Hot Spot Mutation in a Mouse Model of Li-

Fraumeni Syndrome. *Cell* **119**, 861–872 (2004).
205. Kobel, M. *et al.* The biological and clinical value of p53 expression in pelvic high-grade serous carcinomas. *J. Pathol.* **222**, 191–198 (2010).
206. Wojnarowicz, P. M. *et al.* The genomic landscape of TP53 and p53 annotated high grade ovarian serous carcinomas from a defined founder population associated with patient outcome. *PLoS One* **7**, e45484 (2012).
207. Leroy, B., Anderson, M. & Soussi, T. TP53 mutations in human cancer: database reassessment and prospects for the next decade. *Hum. Mutat.* **35**, 672–688 (2014).
208. Liu, D. P., Song, H. & Xu, Y. A common gain of function of p53 cancer mutants in inducing genetic instability. *Oncogene* **29**, 949–956 (2010).
209. Dong, P., Xu, Z., Jia, N., Li, D. & Feng, Y. Elevated expression of p53 gain-of-function mutation R175H in endometrial cancer cells can increase the invasive phenotypes by activation of the EGFR/PI3K/AKT pathway. *Mol. Cancer* **8**, 103 (2009).
210. Tung, K.-H. *et al.* Effect of anovulation factors on pre- and postmenopausal ovarian cancer risk: revisiting the incessant ovulation hypothesis. *Am. J. Epidemiol.* **161**, 321–329 (2005).
211. Fathalla, M. F. Incessant ovulation; a factor in ovarian neoplasia? *Lancet* **298**, 163 (1971).
212. McGuire, V. *et al.* Relation of contraceptive and reproductive history to ovarian cancer risk in carriers and noncarriers of BRCA1 gene mutations. *Am. J. Epidemiol.* **160**, 613–618 (2004).
213. McLaughlin, J. R. *et al.* Reproductive risk factors for ovarian cancer in carriers of BRCA1 or BRCA2 mutations: a case-control study. *Lancet. Oncol.* **8**, 26–34 (2007).
214. Narod, S. A. *et al.* Oral contraceptives and the risk of hereditary ovarian cancer. Hereditary Ovarian Cancer Clinical Study Group. *N. Engl. J. Med.* **339**, 424–428 (1998).
215. Agarwal, A., Gupta, S. & Sharma, R. K. Role of oxidative stress in female reproduction. *Reprod. Biol. Endocrinol.* **3**, 28 (2005).
216. Revelli, A. *et al.* Follicular fluid content and oocyte quality: from single biochemical markers to metabolomics. *Reprod. Biol. Endocrinol.* **7**, 40 (2009).
217. Johnson, M. L., Murdoch, J., Van Kirk, E. A., Kaltenbach, J. E. & Murdoch, W. J. Tumor necrosis factor alpha regulates collagenolytic activity in preovulatory ovine follicles: relationship to cytokine secretion by the oocyte-cumulus cell complex. *Biol. Reprod.* **61**, 1581–1585 (1999).
218. Emori, M. M. & Drapkin, R. The hormonal composition of follicular fluid and its implications for ovarian cancer pathogenesis. *Reprod. Biol. Endocrinol.* **12**, 60 (2014).
219. Bahar-Shany, K. *et al.* Exposure of fallopian tube epithelium to follicular fluid mimics carcinogenic changes in precursor lesions of serous papillary carcinoma. *Gynecol. Oncol.* **132**, 322–327 (2014).
220. Huang, H.-S. *et al.* Mutagenic, surviving and tumorigenic effects of follicular fluid in the context of p53 loss: initiation of fimbria carcinogenesis. *Carcinogenesis* **36**, 1419–1428 (2015).
221. King, S. M. *et al.* The impact of ovulation on fallopian tube epithelial cells: evaluating three hypotheses connecting ovulation and serous ovarian cancer. *Endocr. Relat. Cancer* **18**, 627–642 (2011).
222. Brachova, P., Alvarez, N. S., Van Voorhis, B. J. & Christenson, L. K. Cytidine deaminase Apobec3a induction in fallopian epithelium after exposure to follicular fluid. *Gynecol. Oncol.* **145**, 577–583 (2017).
223. Liu, Y. *et al.* Role of miR-182 in response to oxidative stress in the cell fate of human

fallopian tube epithelial cells. *Oncotarget* **6**, 38983–38998 (2015).
224. Baandrup, L., Kjaer, S. K., Olsen, J. H., Dehlendorff, C. & Friis, S. Low-dose aspirin use and the risk of ovarian cancer in Denmark. *Ann. Oncol. Off. J. Eur. Soc. Med. Oncol.* **26**, 787–792 (2015).
225. Trabert, B. *et al.* Aspirin, nonaspirin nonsteroidal anti-inflammatory drug, and acetaminophen use and risk of invasive epithelial ovarian cancer: a pooled analysis in the Ovarian Cancer Association Consortium. *J. Natl. Cancer Inst.* **106**, djt431 (2014).
226. Verdoodt, F., Dehlendorff, C., Friis, S. & Kjaer, S. K. Non-aspirin NSAID use and ovarian cancer mortality. *Gynecol. Oncol.* **150**, 331–337 (2018).
227. Tone, A. A. *et al.* Gene expression profiles of luteal phase fallopian tube epithelium from BRCA mutation carriers resemble high-grade serous carcinoma. *Clin. Cancer Res.* **14**, 4067–4078 (2008).
228. Tone, A. A., Virtanen, C., Shaw, P. & Brown, T. J. Prolonged postovulatory proinflammatory signaling in the fallopian tube epithelium may be mediated through a BRCA1/DAB2 axis. *Clin. Cancer Res.* **18**, 4334–4344 (2012).
229. Hollingsworth, J. *et al.* BRCA1 Mutation Status and Follicular Fluid Exposure Alters NFkappaB Signaling and ISGylation in Human Fallopian Tube Epithelial Cells. *Neoplasia* **20**, 697–709 (2018).
230. Ince, T. A. *et al.* Characterization of twenty-five ovarian tumour cell lines that phenocopy primary tumours. *Nat. Commun.* **6**, 7419 (2015).
231. Kessler, M. *et al.* The Notch and Wnt pathways regulate stemness and differentiation in human fallopian tube organoids. *Nat. Commun.* **6**, 8989 (2015).
232. Bryant, H. E. *et al.* Specific killing of BRCA2-deficient tumours with inhibitors of poly(ADP-ribose) polymerase. *Nature* **434**, 913–917 (2005).
233. Farmer, H. *et al.* Targeting the DNA repair defect in BRCA mutant cells as a therapeutic strategy. *Nature* **434**, 917–21 (2005).
234. Kim, G. *et al.* FDA Approval Summary: Olaparib Monotherapy in Patients with Deleterious Germline BRCA-Mutated Advanced Ovarian Cancer Treated with Three or More Lines of Chemotherapy. *Clin. Cancer Res.* **21**, 4257–4261 (2015).
235. Thompson, L. L., Jeusset, L. M.-P., Lepage, C. C. & McManus, K. J. Evolving Therapeutic Strategies to Exploit Chromosome Instability in Cancer. *Cancers (Basel).* **9**, (2017).
236. Janssen, A., Kops, G. J. P. L. & Medema, R. H. Elevating the frequency of chromosome mis-segregation as a strategy to kill tumor cells. *Proc. Natl. Acad. Sci. U. S. A.* **106**, 19108–19113 (2009).
237. Kops, G. J. P. L., Foltz, D. R. & Cleveland, D. W. Lethality to human cancer cells through massive chromosome loss by inhibition of the mitotic checkpoint. *Proc. Natl. Acad. Sci. U. S. A.* **101**, 8699–8704 (2004).

APPENDIX A: SOLUTIONS

CELL CULTURE

1× McCoy's 5A Complete Cell Culture Medium + 10% FBS

Name	Amount
McCoy's 5A Medium (Hyclone)	450.0 mL
FBS (Sigma-Aldrich)	50.0 mL
Total Volume	500.0 mL

1× RPMI-1640 Complete Cell Culture Medium + 10% FBS + 0.01 mg/mL Insulin

Name	Amount
RPMI-1640 Medium (HyClone)	449.5 mL
FBS (Sigma-Aldrich)	50.0 mL
Insulin (Sigma; 10 mg/mL)	500 μL
Total Volume	500.0 mL

1× DMEM/F12 Cell Culture Medium

Name	Amount
DMEM/F12 Powder (Gibco)	12.0 g
$NaHCO_3$	2.4 g
Milli-Q Water	up to 1.0 L
Total Volume	1.0 L

- Titrate to pH 7.0
- Pass through 0.22 um filter to sterilize
- Store in 2 × 500 mL bottles at 4°C

USG Serum Substitute

Name	Amount
USG Powder (Pall Corp.)	1 vial
UltraPure Distilled Water (Gibco)	20.0 mL
Total Volume	20.0 mL

- Let stand 20 min at RT to dissolve powder; mix by pipetting
- Store at -20°C in 10 mL aliquots

1× DMEM/F12 Complete Cell Culture Medium + 2% USG

Name	Amount
1× DMEM/F12 Cell Culture Medium	490.0 mL
USG	10.0 mL
Total Volume	500.0 mL

Cupric Sulfate Pentahydrate

Name	Amount
Cupric Sulfate Pentahydrate	26.0 g
Milli-Q Water	up to 1.0 L
Total Volume	1.0 L

10× Phosphate-Buffered Saline (PBS; Stock Solution)

Name	Amount
NaCl	80.0 g
KCl	2.0 g
Na_2HPO_4	14.4 g
KH_2PO_4	2.4 g
Milli-Q Water	up to 1.0 L
Total Volume	1.0 L

- Titrate to pH 7.4

1× PBS

Name	Amount
10× PBS (Stock Solution)	100.0 mL
Milli-Q Water	900.0 mL
Total Volume	1.0 L

GENE SILENCING

1× siRNA Buffer

Name	Amount
5× siRNA Buffer (Dharmacon)	100.0 µL
DEPC-treated Water	400.0 µL
Total Volume	500.0 µL

WESTERN BLOT

Modified Radioimmunoprecipitation Assay (RIPA) Buffer

Name	Amount
50 mM Tris – pH 8.0	5.0 mL
150 mM NaCl	7.5 mL
SDS (0.1% [w/v])	500.0 µL
Sodium Deoxycholate (0.5% [w/v])	0.5 g
NP40 (1% [w/v])	1.0 mL
Milli-Q Water	up to 100 mL
Total Volume	100.0 mL

- Protect from light and store at 4°C

25× Protease Inhibitor

Name	Amount
Protease Inhibitor cOmplete EDTA-free (Roche)	1 tablet
Milli-Q Water	2.0 mL
Total Volume	2.0 mL

- Vortex until dissolved
- Store at -20°C in 50 µL aliquots

Protein Extraction Buffer

Name	Amount
Modified RIPA Buffer	960.0 µL
25× Protease Inhibitor	40.0 µL
Total Volume	1.0 mL

4× Tris-HCl/SDS, pH 6.8 (0.5M Tris-HCl Containing 0.4% SDS)

Name	Amount
Tris	6.05 g
SDS	2.0 g
Milli-Q Water	up to 100 mL
Total Volume	100.0 mL

- Titrate to pH 6.8 with 1N HCl
- Store at 4°C

6× SDS Sample Loading Buffer

Name	Amount
4× Tris-HCl/SDS	6.5 mL
Glycerol	3.0 mL
SDS	1.0 g
β-mercaptoethanol	600.0 µL
Bromophenol Blue	1.2 mg
Total Volume	~10.0 mL

- Store 0.5 mL aliquots at -20°C; warm to RT before use

10× Running Buffer

Name	Amount
Tris Base	30.0 g
Glycine	144.0 g
SDS	10.0 g
Milli-Q Water	up to 1.0 L
Total Volume	1.0 L

1× Running Buffer

Name	Amount
10× Running Buffer	100.0 mL
Milli-Q Water	900.0 mL
Total Volume	1.0 L

1× Transfer Buffer

Name	Amount
10× Running Buffer	50.0 mL
Methanol	100.0 mL
Milli-Q Water	350.0 mL
Total Volume	500.0 mL

Copper Phthalocyanine 3,4',4'',4'''-tetrasulfonic acid Tetrasodium Salt (CPTS)

Name	Amount
CPTS	50.0 mg
HCl	1.0 mL
Milli-Q Water	up to 1.0 L
Total Volume	1.0 L

10× Tris Buffered Saline (TBS)

Name	Amount
NaCl	80.0 g
KCl	2.0 g
1 M Tris – pH 7.5	250.0 mL
Milli-Q Water	up to 1.0 L
Total Volume	1.0 L

1× TBS-Tween20 (TBST)

Name	Amount
10× TBS	100.0 mL
Tween-20	1.0 mL
Milli-Q Water	up to 1.0 L
Total Volume	1.0 L

Non-fat Milk Blocking Solution (5% [w/v])

Name	Amount
Non-fat Milk Powder (Carnation)	5.0 g
TBST	up to 100.0 mL
Total Volume	100.0 mL

CHROMOSOME INSTABILITY ASSAYS

Paraformaldehyde Fixative (4% [w/v])

Name	Amount
Paraformaldehyde (VWR Canlab)	0.4 g
1× PBS	10.0 mL
Total Volume	10.0 mL

- Bring to a slight boil to dissolve paraformaldehyde; cool to RT prior to use

Hoechst 33342 (1 mg/mL Stock Solution)

Name	Amount
Hoechst 33342 (Thermo Scientific)	10.0 mg
1× PBS	up to 10.0 mL
Total Volume	10.0 mL

- Protect from light and store at -20°C

Hoechst 33342 (300 ng/mL Working Dilution)

Name	Amount
Hoechst 33342 Stock Solution	7.0 µL
1× PBS	up to 25.0 mL
Total Volume	25.0 mL

Colcemid (100 ng/mL Working Dilution)

Name	Amount
KaryoMAX Colcemid (Gibco; 10 µg/mL)	10.0 µL
Complete Cell Culture Medium	990.0 µL
Total Volume	1.0 mL

KCl (1 M Stock Solution)

Name	Amount
KCl	7.5 g
Milli-Q Water	up to 100.0 mL
Total Volume	100.0 mL

KCl (75 mM Working Dilution)

Name	Amount
KCl (1 M Stock Solution)	7.5 mL
Milli-Q Water	92.5 mL
Total Volume	100.0 mL

3:1 Methanol:Acetic Acid (Fixative)

Name	Amount
Methanol	12.0 mL
Acetic Acid	4.0 mL
Total Volume	16.0 mL

4',6-Diamidino-2-phenylindole (DAPI; 50 μg/mL Stock Solution)

Name	Amount
DAPI (Sigma-Aldrich; 5 mg/mL)	10.0 μL
1× PBS	990.0 μL
Total Volume	1.0 mL

- Protect from light and store at 4°C

DAPI Mounting Medium

Name	Amount
DAPI (50 μg/mL Stock Solution)	10.0 μL
Vectashield Mounting Medium (Vector Laboratories)	990.0 μL
Total Volume	1.0 mL

- Protect from light and store at 4°C

CRISPR/CAS9

Carbenicillin (50 mg/mL)

Name	Amount
Carbenicillin (VWR Canlab)	0.5 g
Milli-Q Water	10.0 mL
Total Volume	10.0 mL

- Store at -20°C

Luria-Bertani (LB) Agar Plates + 60 μg/mL Carbenicillin

Name	Amount
Tryptone	5.0 g
Yeast Extract	2.5 g
NaCl	5.0 g
LB Agar	7.5 g
Milli-Q Water	up to 500 mL
Carbenicillin (50 mg/mL)	600 μL
Total Amount	~500 mL or 25 plates

- Combine top 5 ingredients and pour into bottle(s) for autoclaving
- Autoclave to dissolve agar and sterilize
- While still warm (~40°C), add carbenicillin and mix
- Pour into 10 cm plates (~20 mL/plate); allow agar to cool and solidify
- Store at 4°C

Kanamycin (50 mg/mL)

Name	Amount
Kanamycin Sulfate (Fisher Scientific)	0.5 g
Milli-Q Water	10.0 mL
Total Volume	10.0 mL

- Store at -20°C

LB Agar Plates + 50 μg/mL Kanamycin

Name	Amount
Tryptone	5.0 g
Yeast Extract	2.5 g
NaCl	5.0 g
LB Agar	7.5 g
Milli-Q Water	up to 500 mL
Kanamycin (50 mg/mL)	500 μL
Total Amount	~500 mL or 25 plates

- Combine top 5 ingredients and pour into bottle(s) for autoclaving
- Autoclave to dissolve agar and sterilize
- While still warm (~40°C), add kanamycin and mix
- Pour into 10 cm plates (~20 mL/plate); allow agar to cool and solidify
- Store at 4°C

LB Broth + 60 μg/mL Carbenicillin

Name	Amount
Tryptone	5.0 g
Yeast Extract	2.5 g
NaCl	5.0 g
LB	7.5 g
Milli-Q Water	up to 500 mL
Carbenicillin (50 mg/mL)	600 μL
Total Amount	~500 mL

- Combine top 5 ingredients
- Autoclave to sterilize
- Allow to cool and add carbenicillin

LB Broth + 50 μg/mL Kanamycin

Name	Amount
Tryptone	5.0 g
Yeast Extract	2.5 g
NaCl	5.0 g
LB	7.5 g
Milli-Q Water	up to 500 mL
Kanamycin (50 mg/mL)	500 μL
Total Amount	~500 mL

- Combine top 5 ingredients
- Autoclave to sterilize
- Allow to cool and add kanamycin

DMEM High Glucose Cell Culture Medium + 10% Tetracycline-Free FBS

Name	Amount
DMEM High Glucose Medium (HyClone)	450.0 mL
Tetracycline-Free FBS (Clontech)	50.0 mL
Total Volume	500.0 mL

Sort Buffer

Name	Amount
USG	200 μL
EDTA (50 mM)	400 μL
1× PBS	up to 10.0 mL
Total Volume	10.0 mL

Propidium Iodide (1 mg/mL Stock Solution)

Name	Amount
Propidium Iodide (Sigma)	1.0 mg
Milli-Q Water	1.0 mL
Total Volume	1.0 mL

- Protect from light and store at -20°C

Sort Buffer + 1 μg/mL Propidium Iodide

Name	Amount
Propidium Iodide (1 mg/mL Stock Solution)	10 μL
USG	200 μL
EDTA (50 mM)	400 μL
1× PBS	up to 10.0 mL
Total Volume	10.0 mL

RNase A (1 mg/mL)

Name	Amount
RNase A (Sigma)	1.0 mg
Milli-Q Water	1.0 mL
Total Volume	1.0 mL

- Store at -20°C

50× Tris-Acetate-EDTA (TAE) Buffer

Name	Amount
Tris	242.0 g
Acetic Acid	57.1 mL
Disodium EDTA	18.61 g
Milli-Q Water	up to 1.0 L
Total Volume	1.0 L

1× TAE Buffer

Name	Amount
50× TAE Buffer	20.0 mL
Milli-Q Water	980.0 mL
Total Volume	1.0 L

INDIRECT IMMUNOFLUORESCENCE

1× PBS + 0.5% Triton X-100

Name	Amount
Triton X-100	5.0 mL
1× PBS	995.0 mL
Total Volume	1.0 L

1× PBS + 0.1% Triton X-100

Name	Amount
Triton X-100	1.0 mL
1× PBS	999.0 mL
Total Volume	1.0 L

WHEAT GERM AGGLUTININ LABELING

Wheat Germ Agglutinin (WGA) Alexa Fluor 488 Conjugate (1 mg/mL Stock Solution)

Name	Amount
WGA Alexa Fluor 488 Conjugate (Life Technologies – Invitrogen)	5.0 mg
1× PBS	5.0 mL
Total Volume	5.0 mL

- Protect from light and store at -20°C

WGA Alexa Fluor 488 Conjugate (5 μg/mL Working Dilution)

Name	Amount
1 mg/mL WGA Alexa Fluor 488 Conjugate (1 mg/mL Stock Solution)	5.0 μL
1× Hank's Balanced Salt Solution (Thermo Scientific)	955.0 μL
Total Volume	1.0 mL

SOFT AGAR COLONY FORMATION ASSAYS

2× DMEM/F12 Cell Culture Medium

Name	Amount
DMEM/F12 Powder (Gibco)	12.0 g
Sodium bicarbonate	2.4 g
Milli-Q Water	up to 500.0 mL
Total Volume	500.0 mL

- Titrate to pH 7.4
- Pass through 0.22 um filter to sterilize
- Store at 4°C

2× DMEM/F12 Complete Cell Culture Medium + 4% USG

Name	Amount
2× DMEM/F12 Cell Culture Medium	480.0 mL
USG	20.0 mL
Total Volume	500.0 mL

2× McCoy's 5A Cell Culture Medium

Name	Amount
McCoy's 5A Powder (Sigma-Aldrich)	11.9 g
Sodium Bicarbonate	2.2 g
Milli-Q Water	up to 500.0 mL
Total Volume	500.0 mL

- Adjust pH to 7.4
- Pass through 0.22 μM filter to sterilize

2× McCoy's 5A Complete Cell Culture Medium + 20% FBS

Name	Amount
2× McCoy's 5A Cell Culture Medium	40.0 mL
FBS	10.0 mL
Total Volume	50.0 mL

2× RPMI-1640 Cell Culture Medium

Name	Amount
RPMI-1640 Powder (Gibco)	10.4 g
Sodium Bicarbonate	2.0 g
Milli-Q Water	up to 500.0 mL
Total Volume	500.0 mL

- Adjust pH to 7.4
- Pass through 0.22 μM filter to sterilize

2× RPMI-1640 Complete Cell Culture Medium + 20% FBS + 0.02 mg/mL Insulin

Name	Amount
2× RPMI-1640 Cell Culture Medium	39.9 mL
FBS	10.0 mL
Insulin (Sigma; 10 mg/mL)	100 μL
Total Volume	50.0 mL

Agarose (1.2% [w/v])

Name	Amount
Agarose (Invitrogen)	1.2 g
Milli-Q Water	100.0 mL
Total Volume	100.0 mL

- Autoclave to dissolve agarose and sterilize
- Warm in microwave prior to use

Agarose (0.8% [w/v])

Name	Amount
Agarose (Invitrogen)	0.8 g
Milli-Q Water	100.0 mL
Total Volume	100.0 mL

- Autoclave to dissolve agarose and sterilize
- Warm in microwave prior to use

Crystal Violet (0.1% [w/v/] Stock Solution)

Name	Amount
Crystal Violet (Sigma-Aldrich)	0.1 g
Methanol	10.0 mL
Milli-Q Water	90.0 mL
Total Volume	100.0 mL

- Pass through filter to sterilize

Crystal Violet (0.005% [w/v] Working Dilution)

Name	Amount
Crystal Violet (0.1% Stock Solution)	2.5 mL
Milli-Q Water	47.5 mL
Total Volume	50.0 mL

APPENDIX B: SUPPLEMENTARY TABLES

Table S1. K-S Tests Identify Significant Changes in NA Distributions Following *SKP1* Silencing in HCT116 Cells.

Condition	n[A]	*p*-value[B]	Significance[C]	D-statistic[D]
Untransfected	300	0.0032	**	0.1467
Non-targeting	300	-	-	-
si*SKP1*-1	300	< 0.0001	****	0.9367
si*SKP1*-2	300	< 0.0001	****	0.8067
si*SKP1*-Pool	300	< 0.0001	****	0.8933

[A]Number of nuclei analyzed.
[B]*p*-values calculated from two-sample K-S tests for the listed condition relative to non-targeting control.
[C]Significance level (**, *p*-value < 0.01; ****, *p*-value < 0.0001).
[D]D-statistic (maximum deviation between the two distribution curves).

Table S2. K-S Tests Identify Significant Changes in NA Distributions Following *CUL1* Silencing in HCT116 Cells.

Condition	n[A]	*p*-value[B]	Significance[C]	D-statistic[D]
Untransfected	300	0.0032	**	0.1467
Non-targeting	300	-	-	-
si*CUL1*-3	300	< 0.0001	****	0.5100
si*CUL1*-4	300	< 0.0001	****	0.3533
si*CUL1*-Pool	300	< 0.0001	****	0.6133

[A]Number of nuclei analyzed.
[B]*p*-values calculated from two-sample K-S tests for the listed condition relative to non-targeting control.
[C]Significance level (**, *p*-value < 0.01; ****, *p*-value < 0.0001).
[D]D-statistic (maximum deviation between the two distribution curves).

Table S3. M-W Tests Identify Significant Increases in MNF Following *SKP1* or *CUL1* Silencing in HCT116 Cells.

Condition	n[A]	Mean Nucleus Count[B]	Mean MN Count[C]	Mean % MNF[D]	Median Fold Change in MNF[E]	*p*-value[F]	Sig.[G]
Untransfected	6	2072	21.0	1.03	0.81	0.5887	ns
Non-targeting	6	1775	20.2	1.31	0.98	-	-
si*SKP1*-1	6	259	22.0	9.06	7.58	0.0022	**
si*SKP1*-2	6	450	119.5	26.71	19.33	0.0022	**
si*SKP1*-Pool	6	397	65.2	16.43	12.39	0.0022	**
si*CUL1*-3	6	464	40.7	8.64	6.33	0.0022	**
si*CUL1*-4	6	827	57.7	7.32	6.16	0.0022	**
si*CUL1*-Pool	6	491	48.5	10.03	7.35	0.0022	**

[A]Number of wells analyzed.
[B]Mean number of nuclei analyzed per well.
[C]Mean number of micronuclei counted per well.
[D]Mean percent MNF (calculated for each well as the MN count / nucleus count × 100).
[E]Median fold change in MNF relative to non-targeting control at the corresponding timepoint.
[F]*p*-values calculated from two-sample M-W tests for the listed condition relative to non-targeting control at the corresponding timepoint.
[G]Significance level (**, *p*-value < 0.01).

Table S4. K-S Tests Identify Significant Changes in NA Distributions Following *SKP1* Silencing in FT194 Cells.

Condition	n[A]	*p*-value[B]	Significance[C]	D-statistic[D]
Untransfected	300	0.0812	ns	0.1033
Non-targeting	300	-	-	-
si*SKP1*-1	300	< 0.0001	****	0.2600
si*SKP1*-2	300	< 0.0001	****	0.2600
si*SKP1*-Pool	300	< 0.0001	****	0.2067

[A]Number of nuclei analyzed.
[B]*p*-values calculated from two-sample K-S tests for the listed condition relative to non-targeting control.
[C]Significance level (ns, not significant; ****, *p*-value < 0.0001).
[D]D-statistic (maximum deviation between the two distribution curves).

Table S5. K-S Tests Identify Significant Changes in NA Distributions Following *SKP1* Silencing in FT246 Cells.

Condition	n[A]	*p*-value[B]	Significance[C]	D-statistic[D]
Untransfected	300	0.2485	ns	0.0833
Non-targeting	300	-	-	-
si*SKP1*-1	300	< 0.0001	****	0.3767
si*SKP1*-2	300	< 0.0001	****	0.2414
si*SKP1*-Pool	300	< 0.0001	****	0.3833

[A]Number of nuclei analyzed.
[B]*p*-values calculated from two-sample K-S tests for the listed condition relative to non-targeting control.
[C]Significance level (ns, not significant; ****, *p*-value < 0.0001).
[D]D-statistic (maximum deviation between the two distribution curves).

Table S6. K-S Tests Identify Significant Changes in NA Distributions Following *CUL1* Silencing in FT194 Cells.

Condition	n[A]	*p*-value[B]	Significance[C]	D-statistic[D]
Untransfected	300	0.0812	ns	0.1033
Non-targeting	300	-	-	-
si*CUL1*-3	300	< 0.0001	****	0.1967
si*CUL1*-4	300	0.0209	*	0.1233
si*CUL1*-Pool	300	0.2099	ns	0.0867

[A]Number of nuclei analyzed.
[B]*p*-values calculated from two-sample K-S tests for the listed condition relative to non-targeting control.
[C]Significance level (ns, not significant; *, *p*-value < 0.05; ****, *p*-value < 0.0001).
[D]D-statistic (maximum deviation between the two distribution curves).

Table S7. K-S Tests Identify Significant Changes in NA Distributions Following *CUL1* Silencing in FT246 Cells.

Condition	n[A]	*p*-value[B]	Significance[C]	D-statistic[D]
Untransfected	300	0.2485	ns	0.0833
Non-targeting	300	-	-	-
si*CUL1*-3	300	0.0005	***	0.1667
si*CUL1*-4	300	0.0659	ns	0.1067
si*CUL1*-Pool	300	0.0002	***	0.1733

[A]Number of nuclei analyzed.
[B]*p*-values calculated from two-sample K-S tests for the listed condition relative to non-targeting control.
[C]Significance level (ns, not significant; ***, *p*-value < 0.001).
[D]D-statistic (maximum deviation between the two distribution curves).

Table S8. M-W Tests Identify Significant Increases in MNF Following *SKP1* or *CUL1* Silencing in FT194 Cells.

Condition	n[A]	Mean Nucleus Count[B]	Mean MN Count[C]	Mean % MNF[D]	Median Fold Change in MNF[E]	*p*-value[F]	Sig.[G]
Untransfected	6	1605	169	10.57	1.07	0.3095	ns
Non-targeting	6	1583	153	9.61	0.97	-	-
si*SKP1*-1	6	1004	182	18.80	1.89	0.0022	**
si*SKP1*-2	6	1147	218	20.70	1.80	0.0022	**
si*SKP1*-Pool	6	885	154	18.65	1.86	0.0022	**
si*CUL1*-3	6	1280	197	15.60	1.58	0.0022	**
si*CUL1*-4	6	1518	151	10.00	1.03	0.2403	ns
si*CUL1*-Pool	6	1507	203	13.48	1.30	0.0087	**

[A]Number of wells analyzed.
[B]Mean number of nuclei analyzed per well.
[C]Mean number of micronuclei counted per well.
[D]Mean percent MNF (calculated for each well as the MN count / nucleus count × 100).
[E]Median fold change in MNF relative to non-targeting control at the corresponding timepoint.
[F]*p*-values calculated from two-sample M-W tests for the listed condition relative to non-targeting control at the corresponding timepoint.
[G]Significance level (ns, not significant; **, *p*-value < 0.01).

Table S9. M-W Tests Identify Significant Increases in MNF Following *SKP1* or *CUL1* Silencing in FT246 Cells.

Condition	n[A]	Mean Nucleus Count[B]	Mean MN Count[C]	Mean % MNF[D]	Median Fold Change in MNF[E]	*p*-value[F]	Sig.[G]
Untransfected	6	516	11	2.11	0.93	0.8182	ns
Non-targeting	6	604	14	2.28	0.99	-	-
si*SKP1*-1	6	165	18	10.64	4.08	0.0022	**
si*SKP1*-2	6	268	21	7.96	3.94	0.0260	*
si*SKP1*-Pool	6	180	16	8.45	3.98	0.0022	**
si*CUL1*-3	6	436	31	7.10	3.05	0.0022	**
si*CUL1*-4	6	557	18	3.26	1.30	0.1797	ns
si*CUL1*-Pool	6	538	33	6.09	2.77	0.0043	**

[A]Number of wells analyzed.
[B]Mean number of nuclei analyzed per well.
[C]Mean number of micronuclei counted per well.
[D]Mean percent MNF (calculated for each well as the MN count / nucleus count × 100).
[E]Median fold change in MNF relative to non-targeting control at the corresponding timepoint.
[F]*p*-values calculated from two-sample M-W tests for the listed condition relative to non-targeting control at the corresponding timepoint.
[G]Significance level (ns, not significant; *, *p*-value < 0.05; **, *p*-value < 0.01).

Table S10. K-S Tests Identify Significant Changes in Chromosome Number Distributions Following *SKP1* or *CUL1* Silencing in FT194 Cells.

Condition	n[A]	*p*-value[B]	Significance[C]	D-statistic[D]
Untransfected	100	0.7736	ns	0.0900
Non-targeting	100	-	-	-
si*SKP1*-1	100	0.0327	*	0.2076
si*SKP1*-2	100	0.0023	**	0.2620
si*SKP1*-Pool	100	< 0.0001	****	0.4284
si*CUL1*-3	100	< 0.0001	****	0.1417
si*CUL1*-4	100	0.0002	***	0.3090
si*CUL1*-Pool	100	< 0.0001	****	0.3552

[A]Number of mitotic spreads analyzed.
[B]*p*-values calculated from two-sample K-S tests for the listed condition vs. non-targeting control.
[C]Significance level (ns, not significant; *, *p*-value < 0.05; **, *p*-value < 0.01; ***, *p*-value < 0.001; ****, *p*-value < 0.0001).
[D]D-statistic (maximum deviation between the two distribution curves).

Table S11. Statistical Assessment of Chromosome Number Distributions Following *SKP1* or *CUL1* Silencing in FT246 Cells.

Condition	n[A]	*p*-value[B]	Significance[C]	D-statistic[D]
Untransfected	100	0.8127	ns	0.0900
Non-targeting	100	-	-	-
si*SKP1*-1	100	0.1644	ns	0.1593
si*SKP1*-2	100	0.1069	ns	0.1729
si*SKP1*-Pool	100	0.3001	ns	0.1387
si*CUL1*-3	100	0.2793	ns	0.1417
si*CUL1*-4	100	0.1790	ns	0.1561
si*CUL1*-Pool	100	0.0171	*	0.2176

[A]Number of mitotic spreads analyzed.
[B]*p*-values calculated from two-sample K-S tests for the listed condition vs. non-targeting control.
[C]Significance level (ns, not significant; *, *p*-value < 0.05).
[D]D-statistic (maximum deviation between the two distribution curves).

Table S12. Statistical Assessment of NA Distributions Within *SKP1*$^{+/-}$ FT246 Cells Over Time.

Condition	n[A]	*p*-value[B]	Significance[C]	D-statistic[D]
p0				
Control	1200	-	-	-
SKP1$^{+/-}$ 1	1200	< 0.0001	****	0.4467
SKP1$^{+/-}$ 2	1200	< 0.0001	****	0.3850
p4				
Control	1200	-	-	-
SKP1$^{+/-}$ 1	1200	< 0.0001	****	0.4025
SKP1$^{+/-}$ 2	1200	< 0.0001	****	0.2650
p8				
Control	1200	-	-	-
SKP1$^{+/-}$ 1	1200	< 0.0001	****	0.3667
SKP1$^{+/-}$ 2	1200	< 0.0001	****	0.2725
p12				
Control	1200	-	-	-
SKP1$^{+/-}$ 1	1200	< 0.0001	****	0.3933
SKP1$^{+/-}$ 2	1200	< 0.0001	****	0.2050
p16				
Control	1200	-	-	-
SKP1$^{+/-}$ 1	1200	< 0.0001	****	0.3525
SKP1$^{+/-}$ 2	1200	< 0.0001	****	0.1050

[A]Number of nuclei analyzed.
[B]*p*-values calculated from two-sample K-S tests for the listed condition relative to non-targeting control at the corresponding timepoint.
[C]Significance level (****, *p*-value < 0.0001).
[D]D-statistic (maximum deviation between the two distribution curves).

Table S13. Statistical Assessment of MNF Within *SKP1*$^{+/-}$ FT246 Cells Over Time.

Condition	n[A]	Mean Nucleus Count[B]	Mean MN Count[C]	Mean % MNF[D]	Median Fold Change in MNF[E]	*p*-value[F]	Sig.[G]
p0							
Control	12	737	22	2.95	1.00	-	-
SKP1$^{+/-}$ 1	12	1124	21	1.85	0.60	0.0007	***
SKP1$^{+/-}$ 2	12	503	42	8.34	2.86	< 0.0001	****
p4							
Control	12	405	14	3.51	1.01	-	-
SKP1$^{+/-}$ 1	12	731	12	1.58	0.50	< 0.0001	****
SKP1$^{+/-}$ 2	12	498	26	5.26	1.61	0.0014	**
p8							
Control	12	617	26	4.30	0.93	-	-
SKP1$^{+/-}$ 1	12	515	8	1.49	0.34	0.0002	***
SKP1$^{+/-}$ 2	12	597	44	7.44	1.65	0.0023	**
p12							
Control	12	618	29	4.72	0.89	-	-
SKP1$^{+/-}$ 1	12	438	9	1.99	0.47	< 0.0001	****
SKP1$^{+/-}$ 2	12	506	40	7.89	1.65	< 0.0001	****
p16							
Control	12	428	17	3.97	0.94	-	-
SKP1$^{+/-}$ 1	12	517	7	1.42	0.31	< 0.0001	****
SKP1$^{+/-}$ 2	12	478	28	5.89	1.50	0.0068	**

[A]Number of wells analyzed.
[B]Mean number of nuclei analyzed per well.
[C]Mean number of micronuclei counted per well.
[D]Mean percent MNF (calculated for each well as the MN count / nucleus count × 100).
[E]Median fold change in MNF relative to non-targeting control at the corresponding timepoint.
[F]*p*-values calculated from two-sample M-W tests for the listed condition relative to non-targeting control at the corresponding timepoint.
[G]Significance level (**, *p*-value < 0.01; ***, *p*-value < 0.001; ****, *p*-value < 0.0001).

Table S14. Statistical Assessment of Chromosome Number Distributions Within *SKP1*$^{+/-}$ FT246 Cells Over Time.

Condition	n[A]	*p*-value[B]	Significance[C]	D-statistic[D]
p0				
Control	100	-	-	-
SKP1$^{+/-}$ 1	100	< 0.0001	****	0.8292
SKP1$^{+/-}$ 2	100	0.0008	***	0.2841
p4				
Control	100	-	-	-
SKP1$^{+/-}$ 1	100	< 0.0001	****	0.8869
SKP1$^{+/-}$ 2	100	0.0048	**	0.2486
p8				
Control	100	-	-	-
SKP1$^{+/-}$ 1	100	< 0.0001	****	0.8900
SKP1$^{+/-}$ 2	100	< 0.0001	****	0.4054
p12				
Control	100	-	-	-
SKP1$^{+/-}$ 1	100	< 0.0001	****	0.7800
SKP1$^{+/-}$ 2	100	0.0001	***	0.3100
p16				
Control	100	-	-	-
SKP1$^{+/-}$ 1	100	< 0.0001	****	0.6785
SKP1$^{+/-}$ 2	100	0.0415	*	0.1984

[A]Number of mitotic spreads analyzed.
[B]*p*-values calculated from two-sample K-S tests for the listed condition relative to non-targeting control at the corresponding timepoint.
[C]Significance level (*, *p*-value < 0.05; **, *p*-value < 0.01; ***, *p*-value < 0.001; ****, *p*-value < 0.0001).
[D]D-statistic (maximum deviation between the two distribution curves).